On the arc wire-directed energy deposition of low thermal expansion Fe–Ni alloys

Sood, A.

DOI
10.4233/uuid:ab67f07d-887f-40c7-8fd4-62ee3ff7302a

Publication date
2025

Document Version
Final published version

Citation (APA)
Sood, A. (2025). *On the arc wire-directed energy deposition of low thermal expansion Fe–Ni alloys*. [Dissertation (TU Delft), Delft University of Technology]. https://doi.org/10.4233/uuid:ab67f07d-887f-40c7-8fd4-62ee3ff7302a

On the arc wire-directed energy deposition of low thermal expansion Fe–Ni alloys

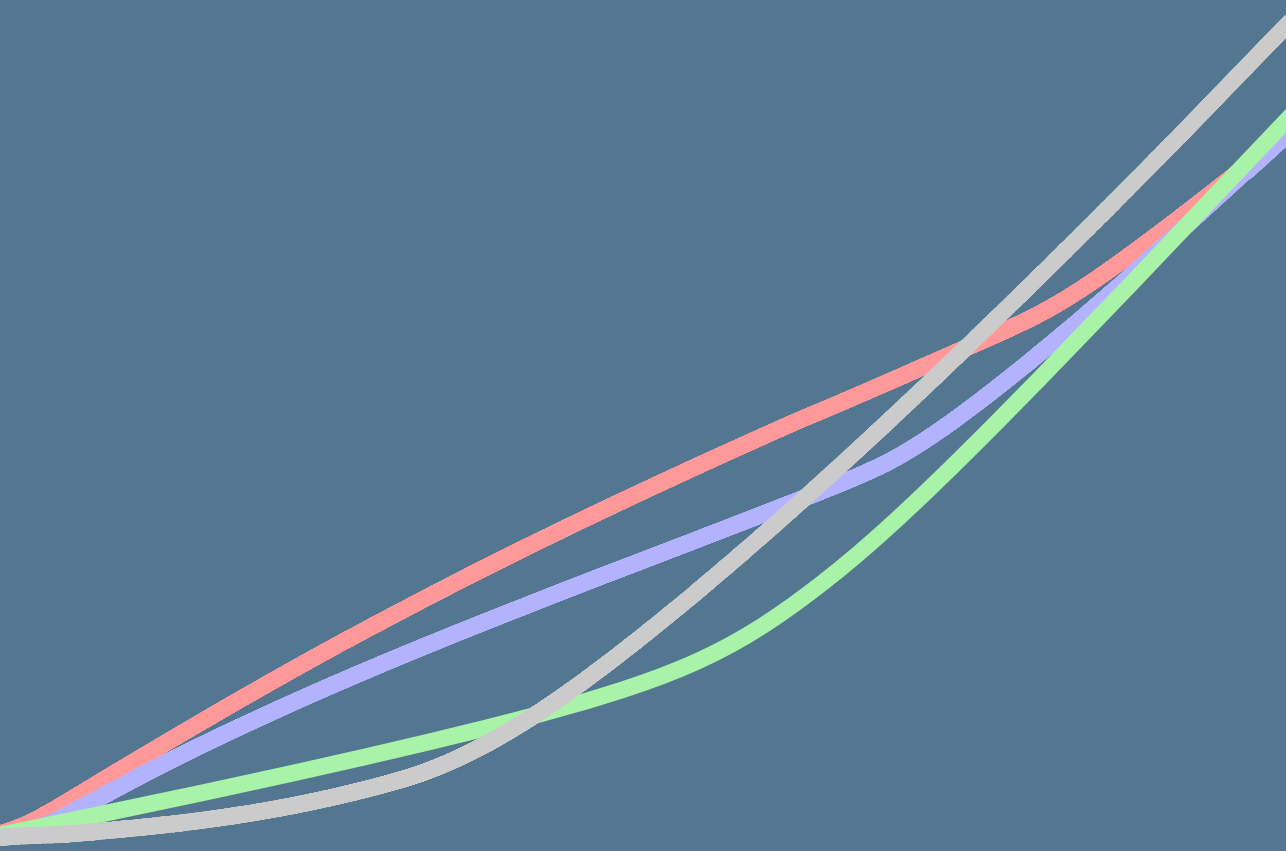

Arjun Sood

On the arc wire-directed energy deposition of low thermal expansion Fe–Ni alloys

On the arc wire-directed energy deposition of low thermal expansion Fe–Ni alloys

Dissertation

for the purpose of obtaining the degree of doctor
at Delft University of Technology
by the authority of the Rector Magnificus, Prof. dr. ir. T.H.J.J. van der Hagen,
chair of the Board for Doctorates,
to be defended publicly on Monday 10 November 2025 at 10:00 a.m.

by

Arjun SOOD

Master of Science in Materials Science and Engineering,
Delft University of Technology, the Netherlands,
born in Hoshiarpur, India.

This dissertation has been approved by the promotors.

Composition of the doctoral committee:

Rector Magnificus,	Chairperson
Dr. ir. M.J.M. Hermans,	Delft University of Technology, promotor
Dr. V.A. Popovich,	Delft University of Technology, promotor
Dr. ir. C. Goulas,	University of Twente, copromotor

Independent members:

Prof. dr. M.J. Santofimia Navarro	Delft University of Technology
Prof. dr. A.A. Zadpoor	Delft University of Technology
Prof. dr. ir. L. A.I. Kestens	Ghent University, Belgium
Prof. dr. S. Ganguly	Cranfield University, United Kingdom

Reserve member:

Prof. dr. ir. R. H. Petrov	Ghent University, Belgium

This research was carried out under the European Union's Horizon 2020 research and innovation programme under grant agreement number 862017, in the framework of the Materials innovation institute, M2i (www.m2i.nl).

Keywords: Thermal expansion; Welding; Cracking; Additive manufacturing; Fe–Ni alloys; Directed energy deposition

Printed by: ProefschriftMaken

Email: arjunsood18@gmail.com

ISBN 978-94-6518-179-0

An electronic copy of this dissertation is available at
https://repository.tudelft.nl/.

You cannot hope to build a better world without improving the individuals. To that end, each of us must work for our own improvement.

Marie Curie

CONTENTS

SUMMARY

The increasing demand for lightweight, high-performance materials in aerospace engineering has led to the widespread adoption of composite material structures. These materials significantly improve fuel efficiency and reduce emissions by lowering the overall weight of the aircraft. However, the manufacturing of composite components requires thermally stable mould tooling to ensure dimensional accuracy during high-temperature curing processes. Consequently, mould tooling materials must exhibit excellent thermal stability to minimise thermal expansion mismatches between the composite component and the moulding tool. Among candidate materials, low thermal expansion (LTE) alloys belonging to the Fe–Ni system, such as alloys 36 and 42, are of considerable interest due to their ability to maintain dimensional stability over a wide temperature range. For instance, alloy 36 exhibits an exceptionally low mean linear coefficient of thermal expansion (CTE) near room temperature, a behaviour primarily attributed to magnetovolume effects arising below its Curie temperature. The high nickel content in alloy 36, nominally 36 wt.%, stabilises a single-phase face-centred cubic (FCC) structure from solidification to room temperature. As a result, alloy 36 and other LTE alloys present specific challenges during conventional processing, including built-up edge formation, significant work hardening, and distortion due to low elastic stiffness. These limitations complicate the fabrication of large or geometrically complex components using subtractive methods, thus necessitating alternative manufacturing strategies. In this context, additive manufacturing offers a promising route, with arc wire directed energy deposition (AW-DED) emerging as a particularly suitable technique owing to its ability to fabricate large-scale structures with high deposition rates and efficient material utilisation.

This thesis elucidates the response of alloy 36 to AW-DED and investigates the fabrication of LTE alloys based on a twin-wire feeding approach. In particular, this study highlights the influence of process parameters on microstructural evolution, thermal properties, and mechanical performance of the as-deposited components. Alloy 36 was deposited at heat inputs ranging from 200–550 $J\,mm^{-1}$ using cold wire gas tungsten arc welding (GTAW) process in the pulsed current mode. Depending on the heat input, the alloy exhibited low resistance to abnormal grain growth leading to significant grain coarsening due to its inherent single-phase austenitic structure. The extent of coarsening increased with increasing heat input, which, in turn, led to increased localisation of the AW-DED induced thermo-mechanical strain at straight grain boundaries and triple junctions of the grains. Consequently, the localisation of strain was found to introduce intergranular voids and cracks in the as-deposited microstructures. These intergranular defects were related to the phenomenon of ductility-dip cracking (DDC) owing to the morphology of the crack, features of the crack flank, and absence of elemental segregation (S and P).

The preservation of high-angle grain boundary area upon reducing the heat input reduced the degree of intergranular strain localisation, thus eliminating DDC in alloy 36 deposited at a heat input of 200 J mm^{-1} during GTAW-based AW-DED. The mechanical performance of the alloy deposited in this heat input condition was also improved compared to that of the alloy deposited at a heat input of 550 J mm^{-1}. In particular, the average yield strength, the ultimate tensile strength, and the elongation increased by 16%, 23%, and 38%, respectively, indicating the successful elimination of DDC. The measured mean linear coefficient of thermal expansion of alloy 36 deposited at the upper and lower extremes of the heat input range, i.e. 200 and 550 J mm^{-1}, remained nearly identical and in agreement with that offered by the conventionally processed material regardless of the specimen orientation.

To extend the functional capability of AW-DED, a twin-wire feeding approach was employed to enable in situ alloying for depositing multiple LTE alloys. A twin-wire feeding approach during GTAW-based AW-DED allows for on-demand deposition of a desired LTE alloy composition and subsequently the thermal expansion properties by exploiting the primarily binary nature of LTE alloys. Therefore, alloy 36 and a high-nickel content wire were simultaneously fed into a melt pool to fabricate mono-material and compositionally graded structures. The low heat input condition from earlier results was adopted to ensure crack-free deposition while melt pool imaging revealed liquid metal transfer characteristics leading to chemically homogeneous and geometrically stable deposition, i.e. the continuous metal transfer mode. This mode allowed the deposition of an alloy 46 mono-material structure that exhibited mean linear CTE values in the vicinity of the standard material specification of alloy 46 in various temperature ranges. In addition, the compositionally graded wall also deposited in the continuous metal transfer mode comprised stable regions of three distinct alloy segments, namely alloys 42, 46, and 52 along the building direction of the wall. These alloy segments were characterised by distinct Curie temperature values that were observed to be on par with the material specifications of their conventionally processed counterparts. This study also examined the occurrence of anisotropy in the thermal expansion behaviour by comparing the temperature-displacement curves of vertically and horizontally oriented specimens. Measurements indicated slight directional differences in CTE, attributed to residual stress-induced alterations in magnetic domain configurations. The maximum absolute difference in CTE between vertical and horizontal specimens reached up to 0.21 µm m^{-1} °C^{-1} for alloy 36 and 0.52 µm m^{-1} °C^{-1} for alloy 46.

A further strategy to suppress DDC while maintaining the high heat input condition, i.e. 550 J mm^{-1}, involved the combined application of accelerated cooling via a CO_2 jet and the addition of titanium carbide (TiC) particles. Incorporation of accelerated cooling reduced the interpass deposition times and the melt pool length during AW-DED of alloy 36. Consequently, heat dissipation increased, leading to a reduction in the extent of grain coarsening and alleviating DDC. However, combining the application of a cooling jet during AW-DED of alloy 36 along with the introduction of TiC particles was necessary to eliminate DDC in alloy 36 deposited at the high heat input condition. The TiC particles acted as grain boundary pinning agents, increasing grain boundary tortuosity and subsequently the grain boundary area. The combined approach of accelerated cooling and TiC addition led to an approximate 70% reduction in the average grain

width and a complete suppression of DDC compared to the unmodified high heat input condition.

The mechanical performance of alloy 36 deposited with the combined approach improved markedly, with respective increases of 18%, 24%, and 60% in the yield strength, tensile strength, and elongation compared to the alloy deposited in the unmodified high heat input condition. In addition to mechanical enhancements, TiC incorporation was found to increase Curie temperature and reduce CTE by up to 34% in the low-temperature range of 30–100 °C. The lattice parameter of the TiC-modified alloy 36, was observed to be higher than that of the TiC-free alloy 36, which corresponds to a weakening of the antiferromagnetic Fe–Fe exchange interaction. This adjustment enhances ferromagnetic ordering, leading to the observed low-temperature CTE reduction in the TiC-modified alloy 36. Although reducing the heat input effectively mitigated DDC in alloy 36, it led to a reduction in the deposition rate. Therefore, the combined approach of accelerated cooling and TiC reinforcement under high heat input conditions presents a more viable path forward for industrial applications, offering both high productivity and defect-free fabrication. The twin-wire feeding methodology demonstrated here also provides a flexible platform for generating on-demand alloy compositions with spatially tunable thermal and magnetic properties.

In summary, this thesis presents a detailed investigation into GTAW-based AW-DED of alloy 36 and related LTE alloys. The present study demonstrates that susceptibility to DDC can be addressed through a combination of heat input control, grain boundary engineering, and thermal management strategies. Furthermore, it establishes the feasibility of in situ alloying using twin-wire feeding to fabricate LTE alloys with graded properties. These results provide a foundation for the reliable fabrication of dimensionally stable, mechanically robust mould tooling and structural components for high-precision aerospace applications.

SAMENVATTING

De toenemende vraag naar lichtgewicht en hoogpresterende materialen in de lucht- en ruimtevaarttechniek heeft geleid tot een brede toepassing van composietconstructies. Deze materialen verbeteren de brandstofefficiëntie aanzienlijk en verminderen de emissies doordat zij het totale gewicht van het vliegtuig verlagen. Voor de vervaardiging van composietonderdelen zijn echter thermisch stabiele matrijzen noodzakelijk om maatnauwkeurigheid te garanderen tijdens uithardingsprocessen bij hoge temperaturen. Matrijsmaterialen moeten daarom een uitstekende thermische stabiliteit vertonen om uitzettingsverschillen tussen het composietonderdeel en het gereedschap tot een minimum te beperken. Onder de kandidaatmaterialen voor matrijzen zijn legeringen met een lage thermische uitzetting (LTE) uit het Fe–Ni-systeem, zoals alloy 36 en 42, bijzonder interessant vanwege hun vermogen om dimensionele stabiliteit te behouden over een breed temperatuurbereik. Zo vertoont alloy 36 een uitzonderlijk lage gemiddelde lineaire uitzettingscoëfficiënt (CTE) nabij kamertemperatuur, een gedrag dat voornamelijk wordt toegeschreven aan magnetovolume-effecten beneden de Curie-temperatuur. Het hoge nikkelgehalte van alloy 36 (nominaal 36 gew.%) stabiliseert een enkelvoudige fase met een kubisch vlakken gecentreerd (KVG) kristalrooster vanaf de stolling tot aan kamertemperatuur. Hierdoor brengen alloy 36 en andere LTE-legeringen specifieke uitdagingen met zich mee bij conventionele bewerking, zoals het ontstaan van opbouwsnedes, aanzienlijke versteviging en vervorming door een lage elasticiteitsmodulus. Deze beperkingen bemoeilijken de vervaardiging van grote of geometrisch complexe onderdelen via subtractieve methoden, waardoor alternatieve productiestrategieën noodzakelijk zijn. In dit kader bieden additieve productiemethoden een veelbelovende route, waarbij arc wire directed energy deposition (AW-DED) zich als een bijzonder geschikte techniek aandient vanwege het vermogen om grootschalige structuren te vervaardigen met hoge depositiesnelheden en efficiënt materiaalgebruik.

Dit proefschrift beschrijft de respons van alloy 36 op AW-DED en de vervaardiging van LTE-legeringen door het gelijktijdig neersmelten van twee toevoegdraden. In het bijzonder wordt de invloed van procesparameters op de microstructurele evolutie, thermische eigenschappen en mechanische prestaties van de vervaardigde componenten bestudeerd. Alloy 36 werd neergesmolten bij warmte-inbrengen variërend van 200 tot 550 J mm^{-1} met behulp van gas tungsten arc lassen (GTAW) in gepulste stroommodus en een koude draadtoevoer. Afhankelijk van de warmte-inbreng vertoont de legering een lage weerstand tegen abnormale korrelgroei, wat leidt tot aanzienlijke grofkorreligheid door de inherent enkelvoudige austenitische structuur. De korrelgrootte neemt toe met stijgende warmte-inbreng en resulteert in een toegenomen lokalisatie van geïnduceerde thermo-mechanische spanningen aan rechte korrelgrenzen en tripelpunten. Dit veroorzaakt interkristallijne holtes en scheuren in de microstructuren van de depositielagen. Deze interkristallijne defecten kunnen in verband gebracht worden met ductility-dip cracking

(DDC), op basis van de scheurmorfologie, de kenmerken van de scheuroppervlakken en de afwezigheid van elementaire segregatie (S en P).

Het behoud van een groter aandeel grote hoek korrelgrenzen door het verlagen van de warmte-inbreng vermindert de mate van interkristallijne spanningslokalisatie, waardoor DDC is geëlimineerd bij alloy 36, geproduceerd met een warmte-inbreng van 200 J mm^{-1}. De mechanische prestaties onder deze condities zijn bovendien beter dan bij 550 J mm^{-1}. Zo nemen de gemiddelde vloeigrens, treksterkte en rek respectievelijk met 16%, 23% en 38% toe, wat de succesvolle eliminatie van DDC bevestigt. De gemeten gemiddelde lineaire uitzettingscoëfficiënt van alloy 36, vervaardigd bij zowel 200 als 550 J mm^{-1}, blijft vrijwel identiek aan die van conventioneel geproduceerd materiaal, onafhankelijk van de specimenoriëntatie.

Om de functionele mogelijkheden van AW-DED uit te breiden werd een dubbeldraadsaanvoersysteem toegepast, waarmee in situ legeren mogelijk werd gemaakt. Deze aanpak maakt het mogelijk om de gewenste legeringssamenstelling en daarmee de thermische uitzettingseigenschappen te realiseren, gebruikmakend van het grotendeels binaire karakter van LTE-legeringen. Daartoe is alloy 36 en een hoog-nikkel draad gelijktijdig toegevoerd in het smeltbad, om zowel mono-materiaal als compositioneel gegradeerde proefstukken te vervaardigen. De lage warmte-inbrengconditie uit eerdere resultaten is toegepast om scheurvrije deposities te garanderen. Videoopnamen van het smeltbad tonen aan dat de vloeibare metaaloverdracht homogeen en stabiel verloopt (continuous metal transfer mode), wat leidt tot chemisch homogene en geometrisch stabiele deposities. Met deze methode is een mono-materiaalstructuur van alloy 46 vervaardigd, waarvan de gemiddelde lineaire CTE-waarden overeenkomt met de standaardspecificaties van alloy 46 in diverse temperatuurbereiken. Daarnaast is een gegradeerde muur vervaardigd, bestaande uit opeenvolgende segmenten van alloy 42, 46 en 52 in de opbouwrichting. Deze segmenten worden gekarakteriseerd door verschillende Curie-temperaturen, die in lijn liggen met conventioneel geproduceerde referentiematerialen. Ook is anisotropie in het thermische uitzettingsgedrag onderzocht door temperatuur-verplaatsingscurves van verticaal en horizontaal georiënteerde proefstukken te vergelijken. De metingen lieten kleine richtingsafhankelijke verschillen in CTE zien, toegeschreven aan door restspanningen geïnduceerde veranderingen in de magnetische domeinconfiguratie. Het maximale verschil in CTE tussen verticale en horizontale proefstukken bedroeg 0.21 µm m^{-1} °C^{-1} voor alloy 36 en 0.52 µm m^{-1} °C^{-1} voor alloy 46.

Een strategie om DDC te onderdrukken bij hoge warmte-inbreng (550 J mm^{-1}) betreft het gecombineerd toepassen van versnelde koeling met behulp van een CO_2 en de toevoeging van titaniumcarbide (TiC)-deeltjes. Versnelde koeling alleen verkort de tijd tussen het aanbrengen van de depositielagen en de beperkt de lengte van het smeltbad, waardoor de warmteafvoer toeneemt en de mate van grofkorreligheid afneemt, wat DDC gedeeltelijk vermindert. Pas door deze koeling te combineren met toevoeging van TiC-deeltjes is DDC volledig geëlimineerd bij hoge warmte-inbreng. De TiC-deeltjes fungeerden als korrelgrenspinners, waardoor de korrelgrenzen grilliger worden en het totale korrelgrensoppervlak toeneemt. Deze gecombineerde aanpak leidt tot een reductie van circa 70% in de gemiddelde korrelbreedte en een volledige onderdrukking van DDC ten opzichte van de ongemodificeerde hoge warmte-inbrengconditie.

De mechanische eigenschappen van alloy 36 verbeteren hierdoor aanzienlijk, met respectievelijke toenames van 18%, 24% en 60% in vloeigrens, treksterkte en rek. Naast deze verbeteringen verhoogt de toevoeging van TiC ook de Curie-temperatuur en verlaagt de CTE met maximaal 34% in het lage temperatuurbereik (30–100 °C). De roosterparameter van de TiC-gemodificeerde alloy 36 blijkt groter te zijn dan die van de TiC-vrije variant, wat duidt op een verzwakking van de antiferromagnetische Fe–Fe-uitwisselingsinteractie. Deze aanpassing versterkt de ferromagnetische ordening, wat resulteert in de waargenomen reductie van de CTE bij lage temperaturen. Hoewel het verlagen van de warmte-inbreng effectief DDC tegengaat, leidt dit tot een lagere neersmeltsnelheid. Daarom biedt de gecombineerde toepassing van versnelde koeling en TiC-toevoeging bij hoge warmte-inbreng een veelbelovende route voor industriële toepassingen, die zowel hoge productiviteit als defectvrije fabricage mogelijk maakt. De hier gedemonstreerde dubbeldraadsaanvoer biedt bovendien een flexibel platform voor het genereren van legeringen met lokaal afstembare thermische en magnetische eigenschappen.

Samenvattend presenteert dit proefschrift een diepgaand onderzoek naar GTAW-gebaseerde AW-DED van alloy 36 en gerelateerde LTE-legeringen. Het onderzoek toont aan dat de gevoeligheid voor DDC kan worden verminderd door een combinatie van warmte-inbreng controle, korrelgrensengineering en thermisch management. Daarnaast is de haalbaarheid van in-situ legeren door middel van dubbeldraadsaanvoer aangetoond voor de vervaardiging van LTE-legeringen met gegradeerde eigenschappen. Deze resultaten vormen een basis voor de betrouwbare productie van dimensioneel stabiele, mechanisch robuuste matrijzen en structurele componenten voor toepassingen in de luchtvaart.

ABBREVIATIONS

AM	Additive Manufacturing
AW-DED	Arc Wire-Directed Energy Deposition
BD	Building Direction
BTF	Buy-to-fly
CT	Continuous Transfer
CTE	Coefficient of Thermal Expansion
DDC	Ductility-dip cracking
FCC	Face-centred cubic
GB	Grain Boundary
GMAW	Gas Metal Arc Welding
GTAW	Gas Tungsten Arc Welding
TIG	Tungsten Inert Gas
HI	Heat Input
IT	Intermittent Transfer
LTE	Low Thermal Expansion
LW-DED	Laser Wire-Directed Energy Deposition
MIG	Metal Inert Gas
PAW	Plasma Arc Welding
RT	Room Temperature
TD	Transverse Direction
WD	Welding Direction

1

INTRODUCTION

1.1. INTRODUCTION

THE utilisation of composite materials in aircraft structures can allow substantial weight reduction while maintaining structural integrity. For example, a primary structural component in an aircraft, the vertical stabiliser, fabricated with carbon composite materials, is 400 kg lighter than an equivalent Al alloy-based component [1]. Weight savings contribute to reduced fuel consumption, as an estimated 2900 L of fuel per year can be saved with a 1 kg reduction in weight [1]. Reduced fuel consumption, in turn, facilitates the realisation of global agreements on greenhouse gas emissions. Consequently, composite materials are becoming the standard material choice for aircraft structures, as shown in Figure 1.1 (a). A typical manufacturing process of a composite[†] material component involves the lay-up of composite material on a moulding tool with subsequent curing at elevated temperature or pressure, or both [2]. Hence, the interaction between the moulding tool and the composite material becomes a key factor in determining the resulting dimensional accuracy of the fabricated composite component [3].

Tool-part interactions can be mainly attributed to the relative mismatch in the coefficient of thermal expansion (CTE) between the composite components and the tooling materials. In Figure 1.1 (b), the linear thermal expansion of various tooling materials is compared for a 4.9 m moulding tool heated to 177 °C. Among these materials, alloy 36 stands out for its highest thermal dimensional stability, evident from the lowest expansion of the alloy 36-based tool in Figure 1.1 (b). This alloy belongs to the Fe–Ni system and offers an unusually low mean linear CTE, approximately 2.0 $\mu m\,m^{-1}\,°C^{-1}$ in the temperature range of 25–149 °C [5]. Similarly to alloy 36, multiple other alloys in the Fe–Ni system, such as alloys 42, 46, and 52, where the number signifies the nominal Ni content, exhibit low CTE values in certain temperature ranges and are known as low thermal expansion (LTE) alloys [6]. Consequently, these alloys, particularly alloys 36 and 42, have become indispensable

[†]Thermosetting polymers constitute the majority of matrix materials used in composite aircraft structural components, the share of thermoplastic polymers is estimated to be less than 5% [4]. Approximately 90% of the thermosetting matrix material is accounted for by epoxy resins, which require a curing cycle as part of the manufacturing process [4].

in the aerospace industry for the fabrication of moulding tools [7].

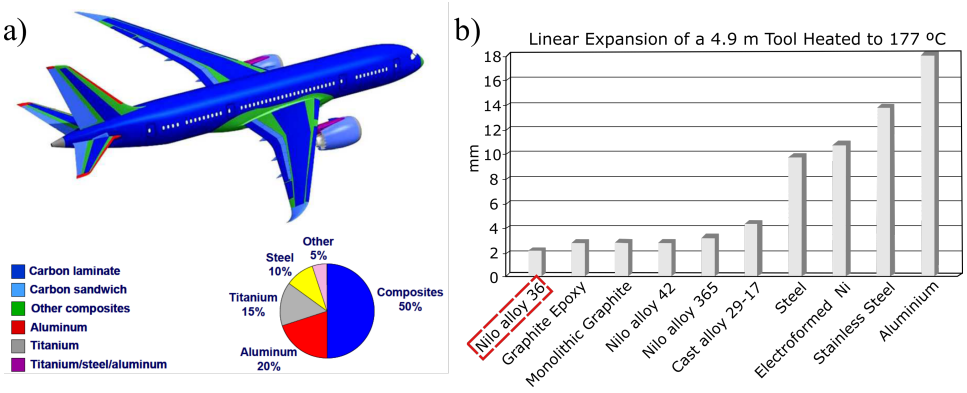

Figure 1.1: An overview of commonly employed materials in a commercial aircraft in (a), and a comparison of the linear thermal expansion of various materials used in a moulding tool heated to 177 °C in (b). Adapted from references [8, 9].

Traditionally, LTE alloy moulding tools are fabricated using as-cast or wrought LTE alloys via subtractive manufacturing [10]. However, the inherent ductile character of LTE alloys leads to material flow rather than cutting, which degrades the efficacy of machining operations [11]. In addition, material utilisation is low during subtractive processing, as the majority of raw material is scrapped [7]. In the case of LTE alloys, material utilisation is paramount due to their substantial costs [12]. Therefore, subtractive manufacturing of LTE alloy components is associated with several challenges, including low material utilisation, extended processing times, and limitations in part complexity [13]. To overcome these challenges, metal additive manufacturing (AM) processes can be employed, which are based on the principle of layer-by-layer deposition of materials at desired locations to create 3-dimensional (3D) structures [14]. Multiple fusion-based metal AM processes exist that can be broadly classified into two categories depending on the form of the feedstock material, i.e. metallic powders or wires. In the former case, metal powders are melted by a heat source (electric arc, or laser and electron beams) to deposit functional components, whereas the latter case relies on metallic wires instead of powders. On the one hand, due to the difference in the type of the feedstock material, metal powder-based AM processes are characterised by lower material utilisation and deposition rates compared to wire-based AM processes. On the other hand, metallic components with high design complexity are limited to fabrication using powder-based processes. Due to the availability of these metal AM processes and their respective advantages, metal AM techniques have rapidly evolved and are adopted in the marine, automotive, and aerospace industries.

Among fusion-based metal AM processes, arc wire-directed energy deposition (AW-DED) offers high deposition rates ($\approx$ 1–10 kg hr^{-1}) and material utilisation [15, 16]. Hence, AW-DED is particularly suitable for fabricating LTE alloy moulding tools. This metal AM technique exploits welding processes—gas metal arc welding (GMAW), gas

tungsten arc welding (GTAW), and plasma arc welding (PAW)—and thus incorporates an electric arc to melt metals and their alloys supplied in the form of wires and generate 3D structures, as shown schematically by the GTAW-based AW-DED setup in Figure 1.2 (a). The aforementioned welding processes are distinct in terms of the features incorporated in the welding torch and the electrode type (consumable or not), as shown schematically in Figures 1.2 (b) and (c). In GMAW, the welding torch supplies the wire concentrically (Figure 1.2 (b)), which, as a consumable electrode, is essential to ignite an arc. In comparison, during GTAW and PAW, the welding torch encloses a non-consumable tungsten alloy electrode, separately from the consumable wire, to ignite an arc. Furthermore, the torch and nozzle in PAW (Figure 1.2) are water cooled, as the nozzle is designed to constrict the arc. This enables a higher energy density of the arc in PAW compared to GMAW and GTAW. Apart from these primary differences among the three welding processes, an AW-DED setup, regardless of the specific welding process used, generally comprises equipment similar to that shown in Figure 1.2 (a).

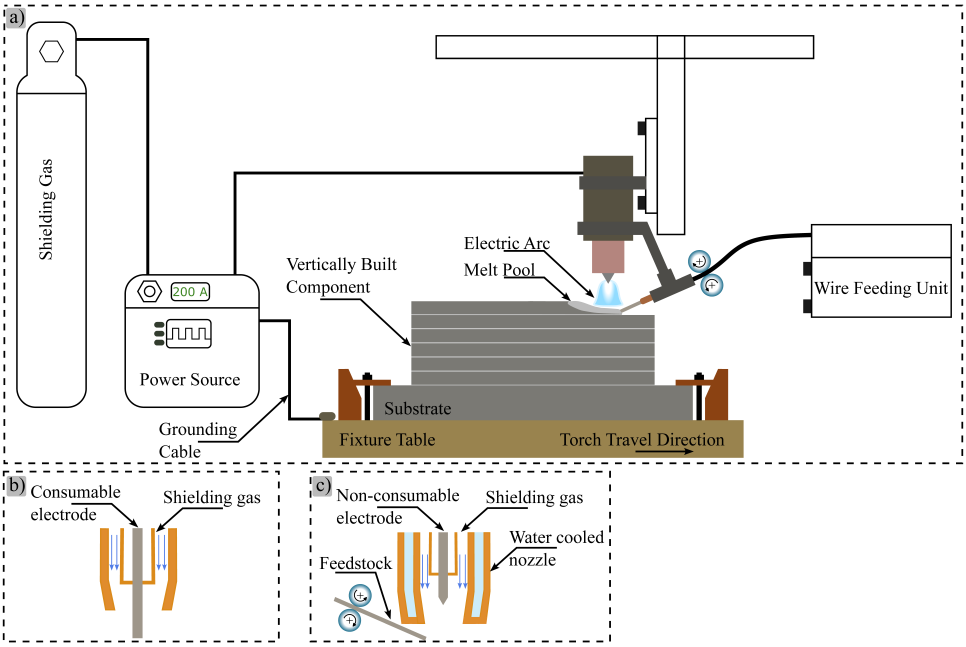

Figure 1.2: A schematic depiction of an AW-DED process employing GTAW in (a), and the torches of GMAW and PAW in (b) and (c), respectively.

In AW-DED, a localised heat source melts the incoming metallic wire and a part of the substrate, which solidifies as the heat source travels, thereby adding new material to the substrate. Repetition of this process leads to the layer-by-layer vertical build-up of components, as shown schematically in Figure 1.2 (a), which are near-net shaped. However, this layer-by-layer material addition leads to cyclic melting-solidification phenomena during AW-DED, which can result in undesirable microstructural aspects

that can deteriorate the functional performance of a component. Consider, for example, the deposition of alloy 36 by AW-DED. This alloy exhibits a single-phase austenitic crystal structure between room temperature and the melting range of the alloy, resulting in a relatively low resistance to grain growth. The localised travelling heat source in AW-DED induces temperature gradients, leading to non-uniform heating and cooling of the material. This results in inhomogeneous thermal expansion and contraction of the material under restraint by the surrounding colder material, thereby introducing residual stresses and strains into the build. Repeated thermal cycling during subsequent layer depositions further redistributes and modifies the residual stress field. Consequently, complex residual stresses and strains develop in the material during AW-DED, which, when coupled with the high susceptibility of alloy 36 to grain growth, can increase the risk of cracking. The anomalous thermal expansion behaviour of alloy 36 can be attributed to a compensation mechanism in which thermally driven volume expansion from lattice vibrations is counteracted by magnetovolume effects, particularly the intrinsically high spontaneous volume magnetostriction of the alloy. Hence, the low CTE of alloy 36 is maintained until about 200 °C, due to the coupling between spontaneous volume magnetostriction and ferromagnetic ordering. At higher temperatures, i.e. in a range of 0.5–0.8 of the solidus, the alloy exhibits a high CTE value similar to that of a typical metal, implying that the introduction of thermal stresses or strains in alloy 36 is justified. The presence of cracks can negatively affect the functional performance of an alloy 36 structure, and grain coarsening can lead to anisotropic material properties. This could likely render the deposited component as unacceptable due to a poor response of the material to AW-DED.

Existing studies on AM and multi-pass welding of alloy 36, to a large extent, report the persistence of intergranular cracks and abnormal grain growth effects [17–20]. Therefore, AW-DED of alloy 36 can be expected to be prone to similar issues. In essence, the functional performance of the alloy in terms of its load-bearing capacity or dimensional stability, or both, can deteriorate [21]. Understanding the response of LTE alloys to AW-DED processing in a manner that highlights the process-property relationships becomes crucial. For instance, this can allow for reducing the sensitivity of an LTE alloy to cracking through parameter optimisation or modification of the grain boundary morphology, while retaining the unique low thermal expansion properties. Moreover, the binary nature of LTE alloys can be exploited to generate on-demand Fe–Ni LTE alloy compositions with desired thermal expansion properties. Employing a twin-wire feeding approach during AW-DED offers the flexibility of synthesising a required chemical composition by in situ alloying. This can be expanded to spatially alter the thermal expansion properties in a structure, also commonly referred to as functional grading. Consequently, enhancing the applicability of AW-DED in processing LTE alloys and paving the way for the transition from machining to AM of LTE alloys.

1.2. AIM OF THE STUDY

The binary Fe–Ni system offers valuable alloys with low thermal expansion that are exploited for their thermal dimensional stability. These alloys exhibit a single-phase austenitic crystal structure in a wide temperature range, which can be easily affected by AW-DED, eventually compromising the functional performance of a deposited structure. The objective of this work is to study and elucidate the response of alloy 36 to AW-DED and to establish the feasibility of generating various LTE alloy compositions by in situ alloying based on a twin-wire feeding approach. For this purpose, GTAW was used to deposit a commercially available alloy 36 wire in a range of heat inputs. Depending on the heat input, the as-deposited alloy exhibited a high propensity to abnormal grain growth. This, in turn, led to the occurrence of intergranular cracking in the as-deposited microstructures. The susceptibility to cracking was found to increase with increasing heat input. Various aspects of the as-deposited microstructures, namely, cracking morphology, phase composition, chemical content, and strain localisation, were studied by scanning electron microscopy (SEM), X-ray diffraction (XRD), X-ray fluorescence (XRF), and electron backscatter diffraction (EBSD), respectively. Lastly, the functional behaviour of the alloy deposited in the upper and lower extremes of the heat input range was established through mechanical and dilatometric analyses.

The parameters resulting in defect-free deposition were further adopted in a twin-wire feed deposition approach to study the feasibility of in situ alloying. Considering the primarily binary Fe–Ni composition of LTE alloys, the twin-wire feeding approach has the potential to enable on-demand generation of desired LTE alloy compositions and the grading of these compositions in a structure. Melt pool imaging with subsequent chemical analysis was performed to investigate the conditions during the twin-wire process that led to geometrically and chemically stable deposited compositions. The thermal expansion behaviour in conjunction with the microstructure of the as-deposited alloys was analysed by dilatometry and EBSD, respectively.

To expand the parametric window during AW-DED, TiC particles were added during the deposition of alloy 36 to induce grain refinement by suppressing abnormal grain growth. This was combined with an external cooling approach to promote heat extraction during deposition. The potential of TiC particles in mitigating cracking and expanding the processing window was demonstrated through mechanical testing. Lastly, the effect of TiC addition on the thermal expansion behaviour of alloy 36 was evaluated using XRD and dilatometry.

The results of this study elaborate on the aspects of intergranular cracking, chemical stability, functional behaviour, and microstructure of LTE alloy components fabricated by AW-DED.

1.3. OUTLINE OF THE THESIS

In chapter 2, commonly employed wire-based metal AM techniques are presented and discussed. The evolution of microstructure during AW-DED is described with reference to its fundamental similarity to welding. This is followed by an introduction to the low

thermal expansion alloys. Critical aspects of their chemical composition and thermal expansion properties are given. Finally, an in-depth review of existing studies on AW-DED and other AM techniques employed to fabricate LTE alloys is presented.

In chapter 3, the chemical compositions of the materials used in the present work are presented. The experimental setup and process conditions used in this study are described, along with the process parameters, melt pool imaging technique, and microstructural characterisation methods. Subsequently, the methodology and instruments employed for analysing the functional properties of the as-deposited LTE alloys through mechanical and dilatometric testing are given.

In chapter 4, results are presented that elaborate the effect of heat input on the microstructure and functional behaviour of alloy 36. A reduction in heat input allowed the deposition of an intergranular crack-free alloy 36 microstructure. This was shown to occur due to the preservation of an increased grain boundary area with a simultaneous reduction in heat input. The presence of grain boundary defects (cracking and voids) deteriorated the mechanical performance of the as-deposited alloy 36. In comparison, the thermal expansion behaviour of the as-deposited alloy was found to be unaffected by such defects.

In chapter 5, a twin-wire feeding approach is adapted for in situ deposition of various LTE alloys. A feasibility study was conducted to address the aspects of geometrical stability and chemical homogeneity. The liquid metal transfer modes, i.e. continuous and intermittent metal transfer, were observed to affect these aspects. Geometrically stable beads with chemical homogeneity were obtained when the deposition was restricted to the continuous metal transfer mode during the twin-wire feeding approach. The LTE alloys deposited in this mode exhibited a thermal expansion behaviour, as reflected by the measured CTE, which was on par with that of the traditionally processed commercially available LTE alloys.

In chapter 6, an attempt is made to expand the deposition window of alloy 36 during AW-DED. The high heat input condition of chapter 3, i.e. 550 $J\,mm^{-1}$, which resulted in grain boundary cracking, was employed to deposit alloy 36 with a combined approach of enhanced cooling and TiC particle addition to mitigate cracking. The combined approach eliminated cracking in alloy 36, as demonstrated by the improved tensile properties of the alloy. In addition, the CTE of the as-deposited alloy 36 with the combined approach decreased, which was shown to occur due to the improved ferromagnetic character of the alloy. Lastly, in chapter 7, the main findings from the earlier chapters are discussed and concluded, followed by recommendations for future work.

REFERENCES

[1] *Introduction: Engineering requirements for aerospace composite materials.* Polymer Composites in the Aerospace Industry. Ed. by P. E. Irving and C. Soutis. 2nd ed. Woodhead Publishing, 2015, pp. 3–22.

[2] D. B. Shah, K. M. Patel, A. I. Patel, V. Pariyal, and S. J. Joshi. *Experimental investigation on spring-back deformation during autoclave curing of parabolic*

antenna reflectors. Composites Part A 115 (2018), pp. 134–146. DOI: 10.1016/j.compositesa.2018.09.017.

[3] Y. Li, Y. Xiao, L. Yu, K. Ji, and D. Li. *A review on the tooling technologies for composites manufacturing of aerospace structures: materials, structures and processes*. Composites Part A 154, no. 106762 (2022). DOI: 10.1016/j.compositesa.2021.106762.

[4] I. Hamerton and J. Kratz. *The use of thermosets in modern aerospace applications*. Thermosets Structure, Properties, and Applications. Ed. by Q. Guo. 2nd ed. Elsevier, 2018, pp. 303–340. DOI: 10.1016/B978-0-08-101021-1.00009-5.

[5] Carpenter Technology. *Controlled-Expansion Alloys*. CRS Holdings, Inc. Accessed: Mar. 04, 2025. Available: https://www.carpentertechnology.com/hubfs/PDFs/Controlled-ExpansionAlloys.pdf.

[6] *Standard specification for iron-nickel sealing alloys*. ASTM Standard F30-96, 2017. DOI: 10.1520/F0030-96R17.

[7] J. Fowler, A. Nycz, M. Noakes, C. Masuo, and D. Vaughan. *Wire-arc additive manufacturing: Invar deposition characterization*. Proceedings of the 30th Annual International Solid Freeform Fabrication Symposium. 2019, pp. 616–624. DOI: 10.26153/tsw/17299.

[8] W. G. Roeseler, B. Sarh, and M. U. Kismarton. *Composite strucutres: The first 100 years*. 16th International Conference on Composite Materials. July 2007, pp. 1–41.

[9] R. J. Smith, G. J. Lewis, and D. H. Yates. *Development and application of nickel alloys in aerospace engineering*. Aircraft Engineering and Aerospace Technology 73, 2 (2001), pp. 138–146. DOI: 10.1108/00022660110694995.

[10] N. Khanna and A. Srivastava. *Optimization and analysis of surface roughness for INVAR-36 in end milling operations*. Materials Today: Proceedings 5, 2 (2018), pp. 5281–5288. DOI: 10.1016/j.matpr.2017.12.111.

[11] A. Sahoo and V. R. Medicherla. *Fe-Ni Invar alloys: A review*. Materials Today: Proceedings 43, 2 (2021), pp. 2242–2244. DOI: 10.1016/j.matpr.2020.12.527.

[12] H. Guo, D. Liu, M. Xu, Z. Dong, and L. Zhang. *Preparation, characterization and composition optimization design of laser powder bed fusion continuously graded Invar36/316L stainless steel alloys*. Materials Characterization 209, no. 113709 (2024). DOI: 10.1016/j.matchar.2024.113709.

[13] D. Jafari, T. H. Vaneker, and I. Gibson. *Wire and arc additive manufacturing: Opportunities and challenges to control the quality and accuracy of manufactured parts*. Materials and Design 202, no. 109471 (2021). DOI: 10.1016/j.matdes.2021.109471.

[14] M. Armstrong, H. Mehrabi, and N. Naveed. *An overview of modern metal additive manufacturing technology*. Journal of Manufacturing Processes 84 (2022), pp. 1001–1029. DOI: 10.1016/j.jmapro.2022.10.060.

[15] L. Vazquez, A. Iturrioz, P. L. de Uralde, and P. Alvarez. *Maximising the deposition rate of 5356 aluminium alloy by CMT-Twin-based WAAM while reducing segregation-related problems by local IR thermography*. Metals 13, 11, no.1890 (2023). DOI: 10.3390/met13111890.

[16] S. W. Williams, F. Martina, A. C. Addison, J. Ding, G. Pardal, and P. Colegrove. *Wire + arc additive manufacturing*. Materials Science and Technology 32, 7 (2016), pp. 641–647. DOI: 10.1179/1743284715Y.0000000073.

[17] Y.-C. Zhang, H. Nakagawa, and F. Matsuda. *Weldability of Fe-36%Ni alloy (report III) : Dynamic observation of reheat hot crack and evaluation of hot ductility of reheated weld metal (materials, metallurgy & weldability)*. Transactions of JWRI 14, 1 (1985), pp. 107–117.

[18] J. L. Corbacho, J. C. Suérez, and F. Molleda. *Welding of Invar Fe-36Ni alloy for tooling of composite materials*. Welding International 12, 12 (1998), pp. 966–971. DOI: 10.1080/09507119809448543.

[19] H. Nakagawa, F. Matsuda, A. Nagai, and N. Sakabata. *Weldability of Fe-36%Ni alloy (report I) : Hot cracking with cross-bead test (materials, metallurgy, weldability)*. Transactions of JWRI 9, 2 (1980), pp. 197–204.

[20] J. L. Corbacho, J. C. Suárez, and F. Molleda. *Grain coarsening and boundary migration during welding of Invar Fe-36Ni alloy*. Materials Characterization 41, 1 (1998), pp. 27–34. DOI: 10.1016/S1044-5803(98)00020-5.

[21] H. Tan, Y. Wang, G. Wang, F. Zhang, W. Fan, Z. Feng, and X. Lin. *Investigation on microstructure and properties of laser solid formed low expansion Invar 36 alloy*. Journal of Materials Research and Technology 9, 3 (2020), pp. 5827–5839. DOI: 10.1016/j.jmrt.2020.03.108.

2

BACKGROUND

IN this chapter, an overview of the commonly employed directed energy deposition (DED) techniques, material evolution during arc wire-DED, introduction to low thermal expansion alloys, and the current state of additive manufacturing of alloys with a low coefficient of thermal expansion is provided.

2.1. DIRECTED ENERGY DEPOSITION TECHNIQUES

The term directed energy deposition refers to processes that use a focused energy source to melt feedstock materials in the form of wires or powders and create components in a layer-by-layer manner. In general, DED processes employing a laser beam or an electric arc as the heat source have gained significant attention compared to electron beam processing for the purpose of large-scale metal AM. Applying these sources to wire feedstock materials results in two distinct process designations, namely laser wire-DED (LW-DED) and arc wire-DED (AW-DED). These processes are described in the following sections.

2.1.1. LASER WIRE-DED

Laser-wire DED uses a laser beam as a heat source to melt metal wires and is also known as wire laser metal deposition (W-LMD). A schematic of the LW-DED process is shown in Figure 2.1 (a), with the wire being fed laterally to the melt pool by an independent feeding system. Alternatively, the laser and the wire can be delivered coaxially to the substrate by employing a different laser head, as shown in Figure 2.1 (b). During LW-DED, manipulation of the laser head or the substrate, or both, through a motion control system allows for the deposition of 3D structures. A shielding gas can also be used to protect the melt pool from ambient contamination. A variety of lasers (diode, CO_2, fibre, Nd:YAG or Yb:YAG) can be utilised in LW-DED, which are characterised by different wavelengths [1–4]. The shorter wavelengths offered by YAG, fibre, and diode lasers, compared to a CO_2 laser, make these more suitable for LW-DED due to the relatively higher energy absorption by metals [5].

As LW-DED relies on lasers, an intensely concentrated heat source can be delivered to the substrate. The combination of wide ranges in spot size and power settings

enables the delivery of a high power density heat source, generally ranging from 10^7–10^{11} W m^{-2} [5]. Depending on the power density of the incident laser beam, two distinct laser processing modes can be obtained: conduction mode and keyhole mode. The conduction mode occurs when the power density of the incident laser beam on the metal surface is relatively low. The incident energy from the laser beam is locally absorbed at the surface, which is then transferred to the surrounding material, resulting in the evolution of a melt pool purely on the basis of heat conduction. When the power density exceeds a certain threshold, metal vaporisation occurs, depressing the surface of the melt pool due to the recoil pressure exerted by the escaping metal vapour. This leads to the formation of a cavity, known as a keyhole, which is filled with a mixture of ionised metal vapour and ambient gas. Power densities typically below 10^9 W m^{-2} are suitable in LW-DED, enabling melting in the conduction mode [5–7]. Limiting LW-DED to process conditions that enable the conduction mode results in a stable deposition process while also preventing excessive elemental loss through vaporisation, which is typically associated with the keyhole mode. Existing studies have employed laser beam spot sizes in the range of 0.3–4 mm, power settings that vary between 0.1–8 kW, and travel speeds in the range of 1–75 mm s^{-1} [8–12]. Although LW-DED is relatively new compared to AW-DED, it has been successfully applied to fabricate various metals such as stainless steels, Ni-based superalloys, and titanium-based alloys [13]. The growing interest in this technology has also led to the development of commercially available LW-DED systems [14].

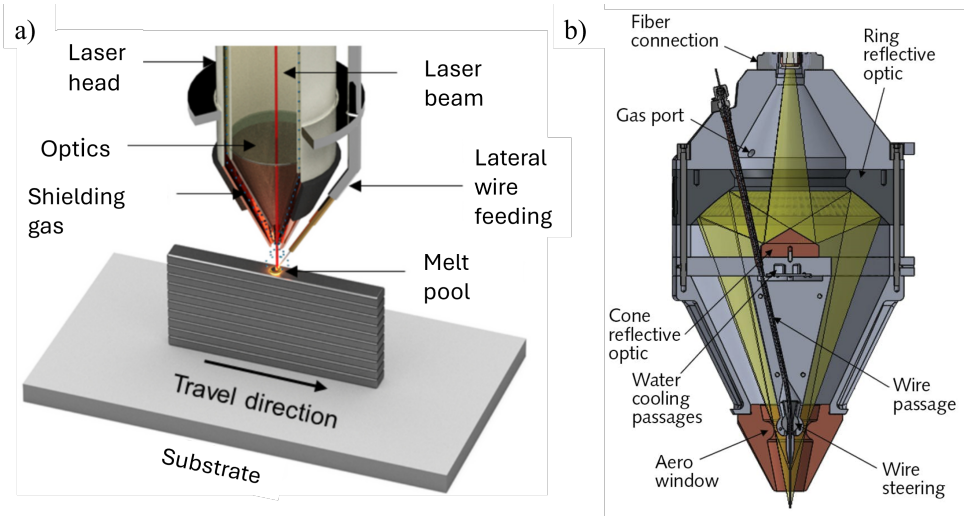

Figure 2.1: A schematic depiction of the laser wire-DED process with an independent wire feeder shown in (a), reproduced with permission from reference [15]. An overview of a laser head allowing for coaxial wire feeding in (b), reproduced with permission from reference [16].

2.1.2. ARC WIRE-DED

Arc wire-DED is based on three long-standing arc welding processes: gas metal arc welding (GMAW), gas tungsten arc welding (GTAW) and plasma arc welding (PAW) [17]. From a welding perspective, GMAW invariably utilises a filler material, whereas GTAW and PAW can be employed without a filler material, in which case the processes are termed autogenous welding. However, a filler material is essential to adapt these processes for the purpose of AW-DED. The fundamental differences among GMAW, GTAW, and PAW processes are attributed to the type of electrode and the nozzle design, as shown in Figures 2.2 (a), (b), and (c).

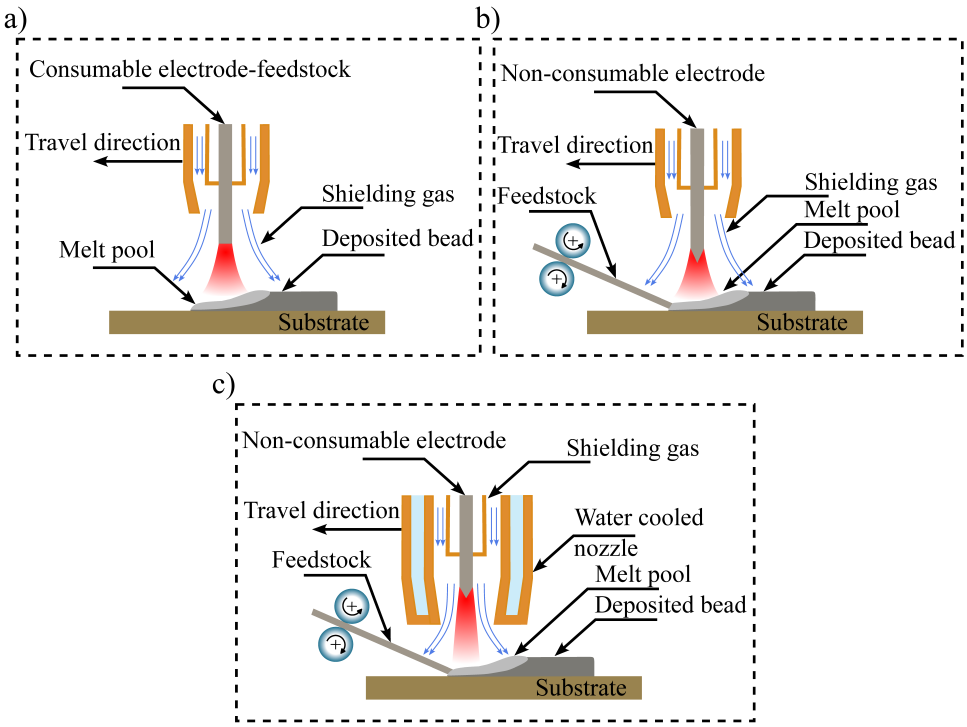

Figure 2.2: Schematic depiction of AW–DED processes based on GMAW (a), GTAW (b), and PAW (c). These processes are primarily distinguished by whether the electrode is consumable or non-consumable.

In GMAW, an electric arc is established between the workpiece and a consumable wire (feedstock) electrode. The energy from the arc leads to the formation of a melt pool to which molten metal is transferred from the feedstock wire. A shielding gas is applied to generate a stable arc and protect the melt pool from the environment. Depending on the consumable material and the substrate, the process can involve an active or an inert shielding gas, or both. This results in two variations of the GMAW process, namely, metal inert gas (MIG) and metal active gas (MAG). In comparison, during GTAW, also referred to as tungsten inert gas (TIG) welding, the arc is generated

between a non-consumable tungsten alloy electrode and the workpiece. This results in the formation of a melt pool to which a wire can be fed independently from the non-consumable electrode. The shielding gas used in this case is always inert to prevent oxidation of the tungsten alloy electrode. The process is generally performed with the electrode in the negative polarity to prevent electrode overheating and is commonly referred to as the direct-current electrode-negative (DCEN) configuration. The PAW process resembles GTAW but utilises a water-cooled constricting nozzle to increase the energy density of the arc generated by the non-consumable tungsten alloy electrode. Power densities during AW-DED processing are typically on the order of 10^4–10^6 W m^{-2} [14, 18]. In general, an AW-DED setup will use at least one of the welding processes, coupled with a motion control system, to fabricate 3D structures in a layer-by-layer manner. The process is comparable to multi-pass welding in that both involve repetitive thermal cycles from successive passes; however, the boundary conditions and process parameters in AW-DED can differ significantly from those in conventional multi-pass welding. Additional equipment can also be included for active process monitoring and control, improved cooling, and microstructural treatments [19].

In the case of GMAW-based AW-DED, metal transfer from the consumable electrode (feedstock wire) can proceed in multiple modes, including short-circuiting, globular, spray, and pulsed spray transfer [18]. The preferred transfer modes during GMAW-based AW-DED are short-circuiting and pulsed-spray transfers due to their relative advantages in managing heat input and deposition rates while achieving low spatter during deposition. Depending on the metal transfer mode, the material being fabricated and the deposition approach (single or multi-machine), deposition rates of 1–10 kg hr^{-1} can be achieved in GMAW-based AW-DED [20–22]. In contrast, GTAW and PAW-based AW-DED offer limited modes of liquid metal transfer from the arc-independent feedstock wire. The liquid metal from the wire can enter the melt pool continuously (via a persistent liquid metal bride) or intermittently (through interrupted bridging or free flight transfer). These modes of metal transfer are also applicable to LW-DED as in this process the heat source is independent of the feedstock material, similar to that of GTAW- or PAW-based AW-DED. However, studies have demonstrated stable deposition when the deposition mode is restricted to continuous metal transfer and, to some extent, in intermittent metal transfer mode via interrupted bridging [23–25]. The deposition rates in GTAW- and PAW-based AW-DED are lower than those in GMAW-based AW-DED, typically in the range of 0.5–4 kg hr^{-1} [17]. However, the independence of the feedstock wire from the arc in GTAW and PAW-based AW-DED allows for convenient feeding of multiple wires to a single melt pool for the purpose of in situ alloying. This, in turn, enables the generation of desired chemical compositions that exhibit distinct functional properties. Hence, the relevant advantages and process flexibilities associated with GTAW, PAW, and GMAW technologies have led to their successful employment in AW-DED processing to deposit multiple alloy systems: aluminium alloys (GTAW, GMAW), titanium alloys (PAW, GTAW), steels (GTAW, GMAW, PAW) and nickel alloys (GMAW, GTAW, PAW) [26–33]. The potential of AW-DED as a key metal AM technique has been demonstrated by manufacturing industrial products, such as engine connectors, ship propellers,

landing gear assemblies, and wing spars [20, 26].

2.2. MATERIAL EVOLUTION DURING ARC WIRE-DED

The microstructure development during AW-DED can be understood on the basis of microstructural changes encountered in fusion welding. This is justified as AW-DED is built on the fundamentals of arc welding. The heat source during a single-pass fusion weld imposes a local thermal cycle on the material, which, in the case of AW-DED, is repeated layer-by-layer. The travelling heat source leads to the formation of microstructural zones that can be physically and chemically distinct from the original microstructure unaffected by the heat source. The extent of the microstructural changes is determined by the amount of energy introduced to the material, i.e. the heat input, in conjunction with the constituent phase diagram of a material.

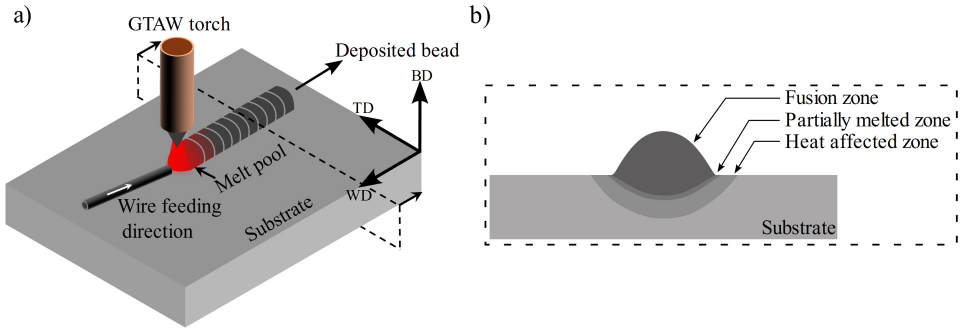

Figure 2.3: A schematic illustration of GTAW-based AW-DED in (a), and a cross-section in the BD-TD plane showing three distinct zones generated in the material influenced by the heat source in (b).

Consider an alloy subjected to a single-pass bead-on-plate GTAW operation with the addition filler material, as shown in Figure 2.3 (a). For simplicity, the chemical composition of the substrate and the filler material is assumed to be identical. A melt pool originates and evolves to stability on the substrate as an arc is created between the substrate and the non-consumable electrode. Following this, the wire is added to the melt pool, which leads to the addition of new material on the substrate. As the heat source moves in the vicinity of the substrate, the material ahead of the heat source is melted along with the incoming wire, while the previously melted material trailing the heat source begins to solidify. Hence, the movement of the heat source results in continuous local melting and solidification of the deposited material and, to some extent, the substrate. The microstructure of the material influenced by the heat source is transformed, resulting in a fusion zone or the weld metal, a partially melted zone, and a heat affected zone, as shown in Figure 2.3 (b).

The fusion zone is characterised by complete melting due to an imposed temperature in excess of the liquidus temperature of the material and a microstructure that is identical to that obtained following casting. The partially melted zone experiences fractional melting as the maximum temperature in this zone remains

between solidus and liquidus temperatures of the material. In comparison, the heat affected zone persists in the solid phase, as the peak temperature in this zone does not exceed the solidus temperature of the material. However, this zone may experience solid-state phase transformations and other microstructural changes, for instance, grain coarsening. During AW-DED, the single pass described in Figure 2.3 (a) is repeated layer by layer. Consequently, the previously deposited material undergoes partial melting and solidification coupled with the complete melting and solidification of the newly added material.

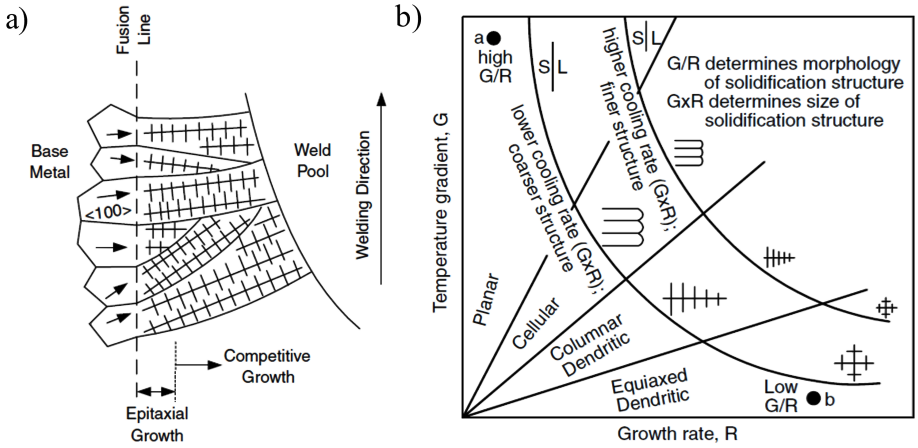

Figure 2.4: Schematic illustration of the microstructural evolution in the fusion zone as determined by the competitive growth mechanism in (a), and the effect of the temperature gradient, G, and the growth rate, R, in determining the morphology and size of the solidification structure in (b). Reproduced with permission from references [34, 35].

The microstructure formation in the fusion zone is primarily governed by a competitive growth mechanism. Solidification in the fusion zone begins with the growth of existing grains at the fusion boundary. These grains grow in a manner to preserve the crystallography of the existing grains at the fusion boundary. This condition is known as epitaxial growth and occurs due to the crystallographic and chemical similarities between the feedstock material and the substrate [36]. Following the initial epitaxial solidification, a competitive grain growth phenomenon occurs, typically until the terminal solidification stage. Competitive growth is driven by two factors: the growth of grains in the direction opposing the maximum thermal gradient, and the preference of grains to follow the easy-growth directions, i.e. <100> in cubic crystal structured alloys [37–39]. The interplay between these factors forces the growth of grains that contain the easy-growth direction antiparallel to the direction of maximum thermal gradient. In cubic alloys, this typically results in the growth of <100> orientated columnar grains from the fusion boundary, perpendicularly towards the trailing melt pool boundary, as shown in Figure 2.4 (a). Since, at any point on the trailing melt pool boundary, the temperature gradient is maximum perpendicular to

the boundary.

Moreover, the solidification microstructure in the fusion zone can display distinct features. The morphology and size of these features are mainly determined by the local solidification rate, R, and the temperature gradient, G, in the melt pool. Depending upon the location in the melt pool and the coupling between G and R, the melt pool may exhibit planar, cellular, columnar, or equiaxed dendritic features. The morphology and size of the solidification microstructure that can appear in the fusion zone of alloys as determined by the ratio G/R and the product G·R[‖], respectively, is shown in Figure 2.4 (b). For instance, close to the fusion line, the ratio of G and R is much higher than that observed close to the trailing edge of the melt pool along its centreline. Consequently, a planar solidification morphology may be observed close to the fusion boundary of a melt pool, which transitions to a cellular, followed by columnar dendritic and finally to equiaxed dendritic morphology, when moving across from the fusion boundary towards the melt pool centreline. This transition in the morphology of the solidification structure in the fusion zone is schematically depicted in Figure 2.5.

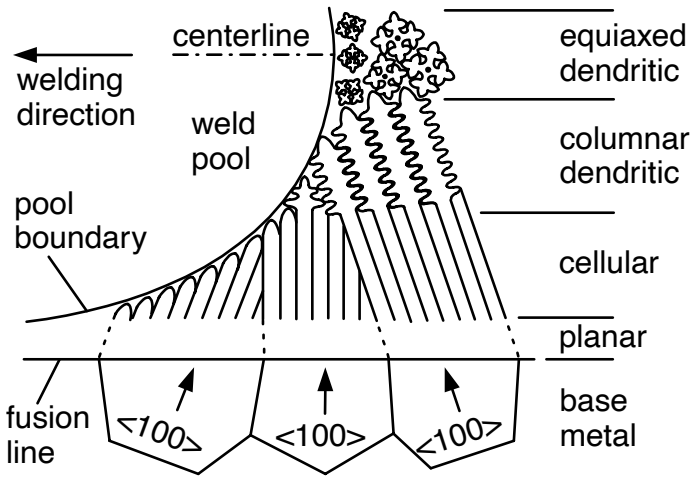

Figure 2.5: Schematic illustration of the microstructural evolution in the fusion zone determined by the competitive growth mechanism coupled with the effect of G and R in determining the morphology of the solidification structure, reproduced with permission from reference [36].

The competitive growth and solidification mechanisms described above also apply to the grain structures formed in alloys during AW-DED processing. For vertically built structures by AW-DED, specifically in the case of thin-walled structures, heat flow is generally maximum towards the substrate. This results in a maximum thermal gradient direction for the bulk, which is antiparallel to the vertical building direction. The mechanism of competitive growth may then lead to the development

[‖]The product G·R is indicative of the cooling rate, as implied by its unit ($°C s^{-1}$).

of a crystallographic texture along this direction. For instance, during AW-DED of single-phase cubic alloys, the bulk of the deposit is commonly observed to be dominated by columnar grains with their <100> directions orientated along the building direction. The existence of a crystallographic texture may lead to directionally dependent anisotropic material properties in a deposited part. However, modification of the processing conditions (heat input or printing strategy) during AW-DED can allow for the manipulation of crystallographic texture.

Figure 2.6: Geometrical distortion in an as-deposited component by AW-DED upon the release of clamps. Reproduced by permission of Informa UK Limited, trading as Taylor & Taylor & Francis Group from reference [32].

In addition to the microstructural changes induced by the heat source, stresses are also developed in a material as a result of the imposed localised thermal cycle. These stresses are retained within a material in the absence of external forces and are thus referred to as residual stresses. In fusion-based welding processes, residual stress generation is mainly attributed to an inhomogeneous temperature field induced in a material by a moving heat source, in conjunction with local plastic deformation [19, 40, 41]. The travelling heat source imposes temperature gradients in a material that cause non-uniform thermal expansion/contraction, which is constrained by the surrounding low-temperature material. This, coupled with the elastic-plastic behaviour of a material, determines the extent of residual stress induced in a material [42]. In the case of additive manufacturing, the extent of residual stress is further influenced by factors such as the build geometry (thin- versus thick-wall) and the deposition sequence.

Residual stresses can be classified into three categories, each associated with a characteristic length scale within the microstructure, as shown in Figure 2.7. Type I residual stresses are averaged over multiple grains and are thus representative of the macroscopic stress state experienced by a material. Type II residual stresses reflect intergranular stresses that vary between grains, but remain essentially constant within a given grain. Type III residual stresses represent stress states on the scale of individual grains, arising from intragranular features such as dislocations, precipitates, solute atoms, and voids within the crystal lattice. The sum of these three types of stresses constitutes the total residual stress.

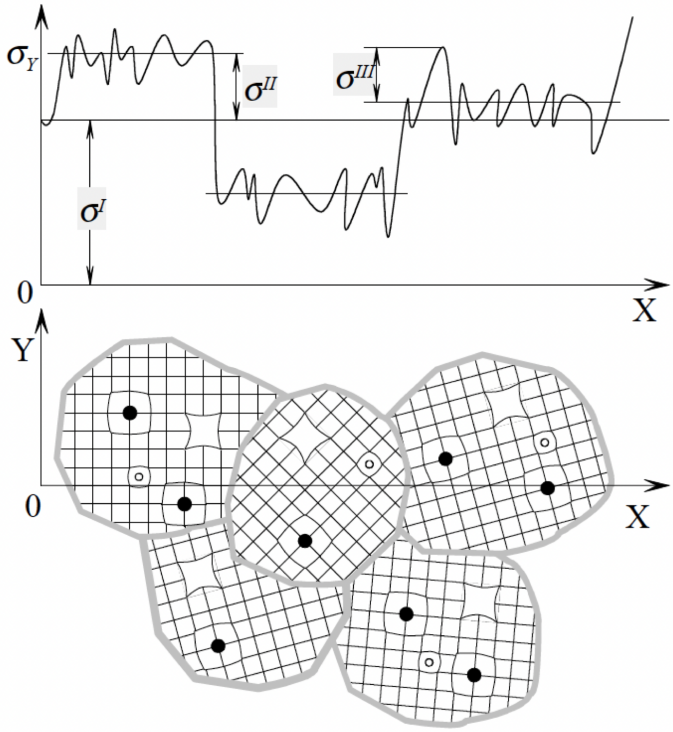

Figure 2.7: Classification of residual stresses according to their characteristic spatial length scales, reproduced with permission from reference [43].

During the production of a component by AW-DED, residual stresses are generated in the newly deposited material, coupled with the redistribution of stresses in the previously deposited layers. Upon completion of the deposition process, the component is cooled to room temperature, after which the clamps are released. At this stage, the component is free from external mechanical restraint, which permits the redistribution of residual stresses. Consequently, the released component typically exhibits distortion, resulting from prior relaxation of residual stresses that exceeded the yield strength of the material, as shown in Figure 2.6. This has a negative impact on the geometrical tolerances of a component produced by AW-DED. On the one hand, tensile residual stresses can lead to layer delamination during deposition or cause cracking, thereby deteriorating the mechanical performance of a component, for example, by reducing its fatigue life. On the other hand, compressive residual stresses near the surface may enhance the fatigue performance of a component [44]. Hence, control over the extent and nature of residual stresses in a component can enable an improvement in functional performance. Hence, controlling the magnitude and nature of residual stresses within a structure can improve its functional performance. Currently, methods such as high-pressure inter-pass rolling, optimisation of the deposition strategy, and preheating have been shown to reduce residual stresses and

distortion in structures fabricated by AW-DED[19, 20, 45, 46].

2.3. LOW THERMAL EXPANSION ALLOYS

The binary Fe–Ni system offers a unique class of alloys that exhibit exceptional thermal dimensional stability. These alloys are characterised by low mean linear coefficients of thermal expansion (CTE) in specific temperature ranges. The Ni content in these alloys dictates their CTE values and is used for their commercial naming. Alloy 36 has a nominal Ni content of 36 wt.% Ni and is popularly known by its trade name Invar 36 [47]. It offers the lowest CTE (α) among the LTE alloys belonging to the binary Fe–Ni system, as shown in Figure 2.8 (a). However, increasing the Ni content expands the low thermal expansion temperature range with a simultaneous increase in the minimum CTE. The anomalous thermal expansion phenomenon in the Fe–Ni system was discovered in 1896 and was later termed the Invar effect [48, 49]. An alloy was developed based on this discovery, which received recognition for its invariant thermal expansion in the vicinity of room temperature, thus being named Invar [50]. Since the discovery of the unusual thermal expansion behaviour in the Fe–Ni system, multiple attempts have been made to address the physical mechanisms underlying this anomaly, which is also commonly referred to as the 'Invar problem' [51–53]. The low CTE of alloy 36 persists approximately until 200 °C, i.e. negligible or low thermal expansion upon heating well below the Curie temperature, followed by a sharp rise in thermal expansion while approaching the Curie temperature. Naturally, studies addressing the Invar problem have underscored magnetically induced volume changes as the key phenomenon leading to anomalous thermal expansion behaviour in LTE alloys[51, 52]. In particular, the Invar effect arises from the compensation of thermal expansion, resulting from anharmonic lattice vibrations during heating, by magnetovolume effects, particularly the spontaneous volume magnetostriction.

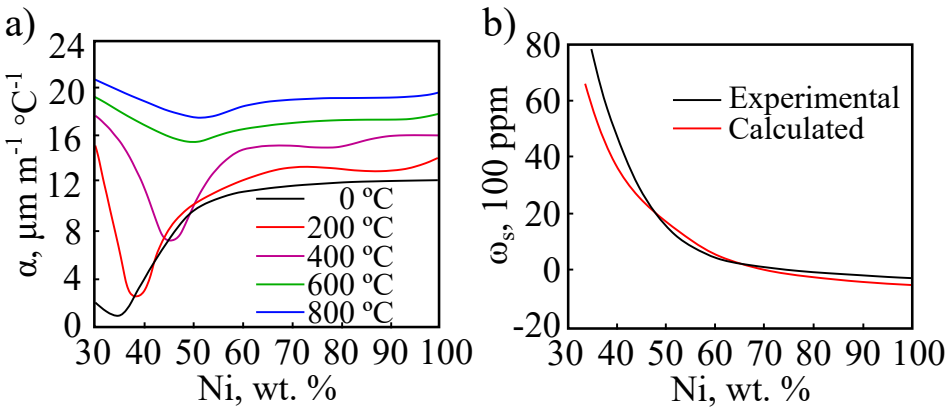

Figure 2.8: The mean linear coefficient of thermal expansion in the Fe–Ni system at various temperatures in (a), and the variation of the spontaneous volume magnetostriction versus the Ni content in (b). Adapted with permission from reference [54].

The variation in spontaneous volume magnetostriction (ω_s), for the binary Fe–Ni system as a function of the Ni content, is shown in Figure 2.8 (b). Unsurprisingly, ω_s is observed to have a maximum at approximately 36 wt.% Ni, thus leading to the lowest CTE in alloy 36 among other LTE alloys belonging to the Fe-Ni system. However, it should be noted that fundamental work aimed at developing a conclusive theory of the Invar effect is still ongoing, despite its discovery more than a century ago [55]. The selection of an LTE alloy for an application is determined by the CTE requirements. Depending on the Ni content, LTE alloys can offer a range of low CTE values that are maintained within specific temperature intervals. In 2.1, a comparison of the CTE values of common LTE alloys in various temperature ranges is presented, highlighting the typical values exhibited by commercially available alloys. Hence, these alloys are used in a variety of applications, such as lunar probes, composite material moulding tools, glass-to-metal sealings, high-precision tools, and cryogenic applications [56].

Table 2.1: A comparison among the CTE of various LTE Fe–Ni alloys in different temperature ranges [57, 58].

Temperature range, °C	Mean linear CTE, µm m^{-1} °C^{-1}			
	Alloy 36	Alloy 42	Alloy 46	Alloy 52
30–149	2.0	5.6	7.7	10.1
30–300	5.9	4.4	7.5	10.1
30–400	8.6	6.0	7.5	9.9
30–500	10.4	7.9	8.5	9.9
30–600	11.6	9.6	9.8	10.8

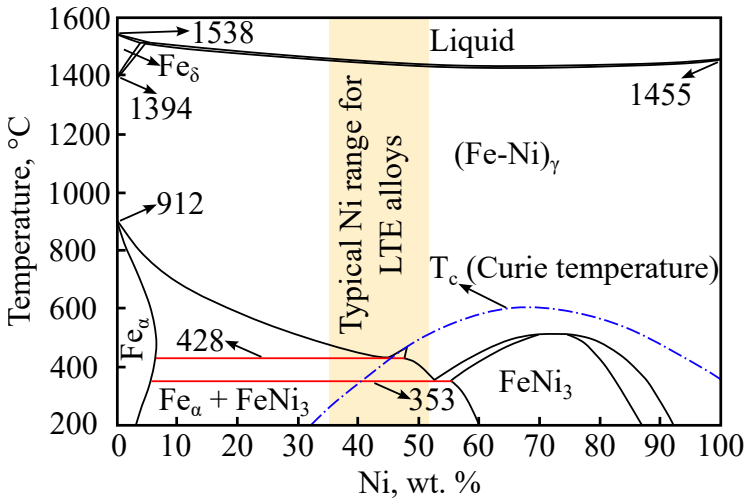

Figure 2.9: The binary phase diagram of Fe–Ni, adapted from reference [59].

The binary Fe–Ni phase diagram based on experimental measurements is shown in Figure 2.9. The typical compositional range pertaining to LTE alloys, along with the dependence of Curie temperature on the Ni content, is highlighted in the figure. Starting from the high-temperature liquid phase region in the Ni range of 36 to 52 wt.%, corresponding to typical LTE alloys, this range experiences a very narrow solidification range when cooling. Following this, a wide austenitic phase field persists approximately until 500 °C. Upon further cooling to room temperature, the equilibrium microstructure according to the phase diagram should be dual phase. However, the solid-solution nature combined with the high Ni content in Fe–Ni LTE alloys results in sluggish substitutional diffusion, thus stabilising the austenitic phase at room temperature [60]. Hence, single-phase LTE Fe–Ni alloys are not hardenable by heat treatment and are generally available commercially in as-cast and wrought conditions. Following cold working or machining operations, the LTE alloys typically require a heat treatment for the temporal stability of the thermal expansion. A commonly employed three-step industrial heat treatment practice for Invar-type LTE alloys is based on the work of Lement *et al.* [61]. The heat treatment is commonly referred to as the Lement heat treatment and comprises the following steps: holding at 750 °C–850 °C followed by water quenching, stress relief at 315 °C–425 °C then air cooling to 90 °C, and subsequent holding at this temperature for 24–48 hours followed by air cooling [47]. A recrystallised homogeneous microstructure, depending on prior material fabrication process, is achieved after the first two steps of the aforementioned heat treatment practice. The holding step allows for temporal stability in LTE alloys, as these alloys can exhibit dimensional changes over a period of time when held isothermally. The finite, time-dependent dimensional instability of LTE alloys is accelerated during the holding step, resulting in alloys that exhibit temporal stability after this heat treatment [62]. However, it should be noted that the effects of such a heat treatment practice are reserved in LTE alloys if the service temperature during their application is maintained below the temperature previously imposed in the final step of the heat treatment. Consequently, the three-step heat treatment practice permits thermal dimensional and temporal stability in LTE alloys. This heat treatment practice was specifically developed for precision tooling applications of alloy 36, or other LTE alloys, such as mounting components for precision tools on space probes, telescopic mirror mounts, and metering rods [62–64]. Moreover, in the past, there was an explicit need for a heat treatment practice to temporally stabilise the thermal expansion of LTE alloys due to the excessively high carbon content of these alloys [65]. In precision tooling equipment, both thermal dimensional stability and isothermal temporal stability are primary requirements. For instance, a dimensional change of 1 ppm in a telescopic mirror mount can change the focus of the instrument by 10 µm [66]. Hence, in the case of alloy 36 employed in precision tooling equipment, a heat treatment practice that establishes temporal stability in the alloy is indispensable. However, such heat treatment practices have limited significance for alloy 36 utilised in aerospace moulding tools, as the heat treatment is essentially disturbed when these tools are heated and cooled during the curing cycles used for fabricating composite materials.

The addition of alloying elements is often required to improve the mechanical and physical properties and workability of the binary Fe–Ni LTE alloys [67, 68]. However,

the thermal expansion of these alloys is very sensitive to alloying additions [69]. The effect of some common alloying elements on the CTE of alloy 36 is shown in Figure 2.10. In contrast to the elements that create a positive change in the CTE of alloy 36, cobalt reduces the CTE. The substitution of 5 wt.% Ni with Co in nominal alloy 36 results in an alloy referred to as Super Invar, which exhibits a near-zero CTE ($\approx 0.6\,\mu m\,m^{-1}\,°C^{-1}$) in the temperature range of approximately 25–100 °C [58].

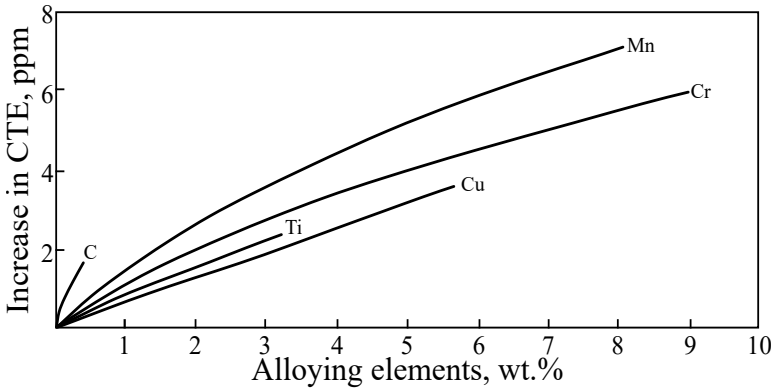

Figure 2.10: The increase in CTE of alloy 36 from nominal value upon the addition of common alloying elements, adapted from reference [70].

2.4. CURRENT STATUS OF ADDITIVELY DEPOSITED ALLOY 36

In applications with stringent requirements for the geometric stability of components, alloy 36 has emerged as the standard choice among LTE alloys. The aerospace industry relies on alloy 36 moulding tools to produce composite material structures [71]. Common aerospace structures, including frames, wing skins, and associated stringers in commercial aircraft, utilise carbon fibre reinforced polymer (CFRP) composites [72, 73]. Fabrication of these composite structures requires curing under applied pressure (0.5–0.7 MPa), elevated temperature (80–180 °C), or a combination of both [74]. A key aspect that governs the dimensional accuracy of the cured composite structures is the tool-part interactions due to the mismatch of CTE. The use of alloy 36 moulding tools can mitigate these interactions, establishing it as a key material for the production of composite structures in the aerospace industry. In cases when curing temperatures up to 300 °C are required, alloy 42 can replace alloy 36 due to its lower CTE in this temperature range, as listed in Table 2.1.

The moulding tools of alloy 36 in the aerospace industry generally have dimensions of a few metres [74]. Arc wire-DED is particularly suitable for fabricating large structures owing to the high deposition rates offered by this processing method. Consequently, multiple studies have been conducted to address the applicability of AW-DED in the fabrication of alloy 36 components. Veiga *et al.* [75] reported on the microstructure and mechanical properties of alloy 36 deposited using PAW- and GMAW-based AW-DED [75]. Defect-free microstructures were obtained with

both processes, mainly dominated by columnar grains. Similarly, the mechanical properties of alloy 36 fabricated using both techniques either exceeded or met the properties of a conventionally produced alloy 36. However, a pronounced anisotropy was observed in the elongation of the PAW-fabricated alloy 36, which was attributed to the corresponding anisotropic microstructure. The elongation of alloy 36 specimens oriented in the building and welding directions was reported to be 51% and 29%, respectively. Building on this work, Aldalur *et al.* [76], studied the thermal expansion properties of alloy 36 fabricated by AW-DED based on GMAW and PAW. They reported that the CTE of alloy 36 fabricated using PAW was significantly higher than that of the alloy deposited by GMAW. The mean CTE of alloy 36 manufactured by GMAW was found to be comparable to that of the commercially available alloy, irrespective of the orientation of the specimen in the deposited component. The discrepancy between the thermal properties of alloy 36 fabricated by the two AW-DED processes was attributed to the higher heat input used during PAW (986 J mm^{-1}) compared to GMAW (446 J mm^{-1}).

Considering the ability of GMAW-based AW-DED to fabricate alloy 36 with satisfactory thermal expansion properties, the authors proceeded to deposit a thin-wall alloy 36 tooling component through a single-bead layering approach. However, this tooling component, which was deposited using the previously established GMAW parameters, showed the generation of hot spots due to heat accumulation as the deposition height increased. Regardless of heat accumulation, the authors argued that the microstructure had remained unaffected. Apart from the defect-free fabrication of alloy 36 through two AW-DED processes, the above studies were limited to a single set of parameters, thus not exploring the parametric processing limits for alloy 36 during AW-DED. For instance, Qiu *et al.* [77] and Tan *et al.* [78], utilised selective laser melting and powder-laser metal deposition, respectively, to fabricate multi-bead alloy 36 structures. In these studies, the microstructure was found to be susceptible to cracking depending on the processing parameters. Additionally, the works of Veiga *et al.* [75] and Aldalur *et al.* [76] employed an alloy 36 wire alloyed with Nb and C for the precipitation of NbC during solidification. These precipitates can improve the strength of the deposited alloy and avoid problems related to grain growth or intergranular cracking in alloy 36. However, the response of Nb-lean alloy 36 during AW-DED would likely deviate from the results reported by Veiga *et al.* [75], especially in structures with multiple bead overlapping. The works of Qiu *et al.* [77] and Tan *et al.* [78], utilised alloy 36 powders that were lean in precipitate-forming elements, such as Ti, Nb, and V, which potentially explains the appearance of the cracking phenomenon reported in their studies. The Nb-lean alloy 36 is widely available as a feedstock for AW-DED and is used in existing moulding tools. Consequently, the utilisation of AW-DED for fabricating precipitate-lean alloy 36 moulding tools, as well as to repair existing tools, requires further investigation.

The work of Aldalur *et al.* [76] is one of the earliest studies to evaluate the effects of AW-DED processing on the thermal expansion behaviour of as-deposited alloy 36. The higher heat input during PAW-based AW-DED of alloy 36 increased its CTE ($\approx$ 3.91 µm m^{-1} °C^{-1}), compared to the CTE ($\approx$ 1.95 µm m^{-1} °C^{-1}) of the alloy fabricated by GMAW-based AW-DED. This discrepancy in CTE was reported to

occur in the temperature range of 0–100 °C, in higher ranges, the CTE of alloy 36 processed by both AW-DED methods converged to values similar to those of the reference alloy. The temperature range of 0–100 °C is well below the Curie transition of alloy 36 and is the region of approximately invariant thermal expansion. This implies that AW-DED processing can influence the underlying physical phenomenon responsible for the invariant thermal expansion of alloy 36, thus affecting its critical low-temperature CTE. Multiple other studies employing AW-DED, SLM, and LPBF techniques have also reported process-induced effects on the thermal expansion behaviour of alloy 36 [79–84]. Among these studies, factors such as defect distribution, grain size, crystallographic texture, and residual stress have been highlighted to induce directional anisotropy and/or deviation from the expected thermal expansion behaviour of alloy 36. But a comparison of the underlying cause that leads to thermal expansion discrepancies in studies of alloy 36 reveals conflicting views. For instance, Jiao *et al.* [82] attributed the anisotropic directional CTE of as-deposited alloy 36 to different grain boundary densities arising from a microstructure dominated by columnar grains. However, Huang *et al.* [84] showed that the magnetic properties controlling the thermal expansion in as-deposited alloy 36 are virtually immune to microstructural variations, i.e. preferred crystal orientations and grain size/morphology. Therefore, the specifics of the effects induced by AW-DED on the thermal expansion of alloy 36 remain largely unanswered, necessitating further consideration.

Hence, the current state-of-art related to the AW-DED of LTE alloys presents multiple opportunities to further expand the applicability of AW-DED in fabricating LTE alloys. Firstly, despite the success of the initial studies in obtaining defect-free thin-wall structures, it is worth noting that industrially applicable LTE alloy structures may require multi-bead overlapping. Consider the use of alloy 36 in the aerospace industry as the primary material for fabricating the face sheet of a moulding tool, which typically has a thickness of approximately 10,mm and spans several metres. The fabrication of such structures necessitates multi-bead overlapping, which is conducive to the formation of defects, such as lack of fusion and intergranular cracking. Moreover, the existing body of work on alloy 36 deposition via AW-DED remains largely limited to a fixed set of processing parameters. To address this gap, it is necessary to investigate the response of alloy 36 to a wider range of process conditions. For instance, the alloy can be deposited using varying levels of heat input, which would enable a detailed assessment of its influence on microstructural evolution and functional performance. Secondly, the ductile nature of LTE alloys presents significant challenges during subtractive manufacturing. To overcome this, AW-DED is a viable alternative processing method, as the LTE alloy structures obtained through this route are near-net shaped. Consequently, the need for subtractive processing is greatly reduced to have a functional LTE alloy component.

In expanding the applicability of AW-DED to LTE alloys, the relatively simple binary Fe-Ni nature of LTE alloys can be exploited. The uncoupled nature of the heat source and feedstock material in GTAW- and PAW-based AW-DED implies that these processes can be adapted for the simultaneous feeding of multiple wires into a melt pool. Combining this process flexibility with the binary Fe–Ni nature of LTE alloys can enable the in situ synthesis of desired LTE alloy compositions. A feasibility

study aimed at establishing the deposition of geometrically stable structures that bear chemical homogeneity of an LTE alloy composition via a twin-wire deposition approach during AW-DED can be undertaken. This approach enables the on-demand fabrication of LTE alloy compositions with a desired CTE, while also facilitating the repair of existing moulding tools, irrespective of their chemical composition. Lastly, the single-phase austenitic structure of LTE alloys is known to increase the susceptibility of these alloys to intergranular cracking. This grain boundary embrittlement phenomenon has been shown to occur in both multi-pass welding operations of alloy 36 and during selective laser melting of alloy 36. In general, a reduction in the heat input can improve the resistance of alloy 36 to intergranular cracking. However, this inevitably also leads to a reduction of the deposition rates which is undesirable in terms of productivity. Alternatively, a high heat input may be retained during the fabrication of alloy 36 structures, provided the grain boundary morphology is modified during the process. This can be achieved by the introduction of external carbide particles into the melt pool during AW-DED, which, in turn, can enable the fabrication of grain boundary defect-free structures without compromising the heat input. Consequently, these open-ended discussions that pertain to enhancing the fabrication of LTE alloys by AW-DED are addressed in the following chapters.

REFERENCES

[1] M. Lammers, K. Biester, N. Schwarz, J. Hermsdorf, S. Kaierle, and H. Ahlers. *Automatic changing of weld deposit for additive manufacturing of hybrid metal-glass components using direct laser deposition*. Lasers in Manufacturing Conference. Accessed: Jan. 11, 2025. Available: https://wlt.de/lim2021-proceedings/directed-energy-deposition. 2021.

[2] E. Brandl, B. Baufeld, C. Leyens, and R. Gault. *Additive manufactured Ti-6Al-4V using welding wire: comparison of laser and arc beam deposition and evaluation with respect to aerospace material specifications*. Physics Procedia 5 (2010), pp. 595–606. DOI: 10.1016/j.phpro.2010.08.087.

[3] M. Motta, A. G. Demir, and B. Previtali. *High-speed imaging and process characterization of coaxial laser metal wire deposition*. Additive Manufacturing 22 (2018), pp. 497–507. DOI: 10.1016/j.addma.2018.05.043.

[4] D. G. Ahn. *Direct metal additive manufacturing processes and their sustainable applications for green technology: A review*. International Journal of Precision Engineering and Manufacturing-Green Technology 3, 4 (2016), pp. 381–395. DOI: 10.1007/s40684-016-0048-9.

[5] J. Elmer, P. Hochanadel, K. Lachenberg, and T. Webber. *Introduction to high energy density electron and laser beam welding*. ASM Handbook, Volume 06A - Welding Fundamentals and Processes. Ed. by T. J. Lienert, S. S. Babu, T. A. Siewert, and V. L. Acoff. ASM International, 2011, pp. 507–511.

[6] L. Quintino and E. Assunção. *Conduction laser welding*. Handbook of Laser Welding Technologies. Woodhead Publishing Limited, 2013. Chap. 6, pp. 139–162. DOI: 10.1533/9780857098771.1.139.

[7] M. Froend, V. Ventzke, N. Kashaev, B. Klusemann, and J. Enz. *Thermal analysis of wire-based direct energy deposition of Al-Mg using different laser irradiances*. Additive Manufacturing 29, no. 100800 (2019). DOI: 10.1016/j.addma.2019.100800.

[8] C. Hagenlocher, P. O'Toole, W. Xu, M. Brandt, M. Easton, and A. Molotnikov. *In process monitoring of the thermal profile during solidification in laser directed energy deposition of aluminium*. Additive Manufacturing Letters 3, no. 100084 (2022). DOI: 10.1016/j.addlet.2022.100084.

[9] M. Madarieta, E. Irazu, I. Garmendia, J. Flores, and C. Soriano. *Geometrical study of 5356 aluminium alloy by means of a concentric wire laser metal deposition*. Procedia CIRP 113 (2022), pp. 361–366. DOI: 10.1016/j.procir.2022.09.143.

[10] L. Wang, L. Wang, Q. Feng, L. Ma, Y. Tang, and B. Li. *High surface quality additive manufacturing process of titanium alloy with composite heat source*. Proceedings of the Institution of Mechanical Engineers, Part B: Journal of Engineering Manufacture 238, 1–2 (2024), pp. 37–47. DOI: 10.1177/09544054231158407.

[11] A. da Silva, S. Wang, J. Volpp, and A. F. H. Kaplan. *Vertical laser metal wire deposition of Al-Si alloys*. Procedia CIRP 94 (2020), pp. 341–345. DOI: 10.1016/j.procir.2020.09.078.

[12] M. Froend, V. Ventzke, S. Riekehr, N. Kashaev, B. Klusemann, and J. Enz. *Microstructure and hardness evolution of laser metal deposited AA5087 wall-structures*. Procedia CIRP 74 (2018), pp. 131–135. DOI: 10.1016/j.procir.2018.08.062.

[13] R. Rumman, D. A. Lewis, J. Y. Hascoet, and J. S. Quinton. *Laser metal deposition and wire arc additive manufacturing of materials: An overview*. Archives of Metallurgy and Materials 64, 2 (2019), pp. 467–473. DOI: 10.24425/amm.2019.127561.

[14] D. G. Ahn. *Directed energy deposition (DED) process: State of the art*. International Journal of Precision Engineering and Manufacturing - Green Technology 8, 2 (2021), pp. 703–742. DOI: 10.1007/s40684-020-00302-7.

[15] A. P. Nagalingam, M. Shamir, E. B. Tureyen, A. R. C. Sharman, O. Poyraz, E. Yasa, and J. Hughes. *Recent progress in wire-arc and wire-laser directed energy deposition (DED) of titanium and aluminium alloys*. The International Journal of Advanced Manufacturing Technology 136 (2025), pp. 2035–2073. DOI: 10.1007/s00170-024-14967-w.

[16] E. Stiles, S. Ream, J. Hay, and C. Walters. *High-Power Coaxial Wire Laser DED*. Accessed: Oct. 06, 2025. Available at: https://www.ewi.org/high-power-coaxial-wire-laser-ded/. Edison Welding Institute (EWI). 2023.

[17] A. Shah, R. Aliyev, H. Zeidler, and S. Krinke. *A review of the recent developments and challenges in wire arc additive manufacturing (WAAM) process*. Journal of Manufacturing and Materials Processing 7, 3 (2023), pp. 97–127. DOI: 10.3390/jmmp7030097.

[18] S. Kou. *Fusion welding processes*. Welding Metallurgy. 3rd ed. Hoboken: John Wiley & Sons, 2021. Chap. 1, pp. 3–35.

[19] T. DebRoy, H. L. Wei, J. S. Zuback, T. Mukherjee, J. W. Elmer, J. O. Milewski, A. M. Beese, A. Wilson-Heid, A. De, and W. Zhang. *Additive manufacturing of metallic components – Process, structure and properties*. Progress in Materials Science 92 (2018), pp. 112–224. DOI: 10.1016/j.pmatsci.2017.10.001.

[20] S. W. Williams, F. Martina, A. C. Addison, J. Ding, G. Pardal, and P. Colegrove. *Wire + arc additive manufacturing*. Materials Science and Technology 32, 7 (2016), pp. 641–647. DOI: 10.1179/1743284715Y.0000000073.

[21] A. Queguineur, R. Asadi, M. Ostolaza, E. H. Valente, V. K. Nadimpalli, G. Mohanty, J. Y. Hascoët, and I. F. Ituarte. *Wire arc additive manufacturing of thin and thick walls made of duplex stainless steel*. International Journal of Advanced Manufacturing Technology 127, 1-2 (2023), pp. 381–400. DOI: 10.1007/s00170-023-11560-5.

[22] L. Vazquez, A. Iturrioz, P. L. de Uralde, and P. Alvarez. *Maximising the deposition rate of 5356 aluminium alloy by CMT-Twin-based WAAM while reducing segregation-related problems by local IR thermography*. Metals 13, 11, no.1890 (2023). DOI: 10.3390/met13111890.

[23] T. Ungethüm, E. Spaniol, M. Hertel, and U. Füssel. *Analysis of metal transfer and weld geometry in hot-wire GTAW with indirect resistive heating*. Welding in the World 64 (2020), pp. 2109–2117. DOI: 10.1007/s40194-020-00986-0.

[24] H.-K. Lee and K.-H. Yun. *A Study on the applicability of A-TIG welding of semi-automatic cold wire feeding process for cryogenic stainless steel pipes*. Journal of Welding and Joining 42, 3 (2024), pp. 231–238. DOI: 10.5781/jwj.2024.42.3.1.

[25] D. Ding, Z. Pan, D. Cuiuri, and H. Li. *Wire-feed additive manufacturing of metal components: Technologies, developments and future interests*. The International Journal of Advanced Manufacturing Technology 81, 1-4 (2015), pp. 465–481. DOI: 10.1007/s00170-015-7077-3.

[26] M. Srivastava, S. Rathee, A. Tiwari, and M. Dongre. *Wire arc additive manufacturing of metals: A review on processes, materials and their behaviour*. Materials Chemistry and Physics 294, no. 126988 (2023). DOI: 10.1016/j.matchemphys.2022.126988.

[27] C. Dharmendra, B. S. Amirkhiz, A. Lloyd, G. D. J. Ram, and M. Mohammadi. *Wire-arc additive manufactured nickel aluminum bronze with enhanced mechanical properties using heat treatments cycles*. Additive Manufacturing 36, no. 101510 (2020). DOI: 10.1016/j.addma.2020.101510.

[28] C. V. Haden, G. Zeng, F. M. Carter, C. Ruhl, B. A. Krick, and D. G. Harlow. *Wire and arc additive manufactured steel: Tensile and wear properties*. Additive Manufacturing 16 (2017), pp. 115–123. DOI: 10.1016/j.addma.2017.05.010.

[29] J. F. Wang, Q. J. Sun, H. Wang, J. P. Liu, and J. C. Feng. *Effect of location on microstructure and mechanical properties of additive layer manufactured Inconel 625 using gas tungsten arc welding*. Materials Science and Engineering: A 676 (2016), pp. 395–405. DOI: 10.1016/j.msea.2016.09.015.

[30] N. P. Gokhale and P. Kala. *Thermal analysis of TIG-WAAM based metal deposition process using finite element method*. Materials Today: Proceedings 44 (2021), pp. 453–459. DOI: 10.1016/j.matpr.2020.09.756.

[31] K. S. Derekar. *A review of wire arc additive manufacturing and advances in wire arc additive manufacturing of aluminium*. Materials Science and Technology 34, 8 (2018), pp. 895–916. DOI: 10.1080/02670836.2018.1455012.

[32] F. Xu, V. Dhokia, P. Colegrove, A. McAndrew, S. Williams, A. Henstridge, and S. T. Newman. *Realisation of a multi-sensor framework for process monitoring of the wire arc additive manufacturing in producing Ti-6Al-4V parts*. International Journal of Computer Integrated Manufacturing 31, 8 (2018), pp. 785–798. DOI: 10.1080/0951192X.2018.1466395.

[33] D. Ding, B. Wu, Z. Pan, Z. Qiu, and H. Li. *Wire arc additive manufacturing of Ti6AL4V using active interpass cooling*. Materials and Manufacturing Processes 35, 7 (2020), pp. 845–851. DOI: 10.1080/10426914.2020.1732414.

[34] S. Kou. *Basic solidification concepts*. Welding Metallurgy. 2nd ed. Hoboken: John Wiley & Sons, Inc., 2003. Chap. 6, pp. 145–169. DOI: 10.1002/0471434027.ch6.

[35] S. Kou. *Weld metal solidification I: Grain structure*. Welding Metallurgy. 2nd ed. Hoboken: John Wiley & Sons, Inc., 2003. Chap. 7, pp. 170–198. DOI: 10.1002/0471434027.ch7.

[36] S. Kou. *Weld metal solidification II: Microstructure within grains*. Welding Metallurgy. 2nd ed. Hoboken: John Wiley & Sons, Inc., 2003. Chap. 8, pp. 199–214. DOI: 10.1002/0471434027.ch8.

[37] J. C. Lippold. *Solid-state cracking*. Welding Metallurgy and Weldability. Hoboken: John Wiley & Sons, Inc., 2015. Chap. 4, pp. 130–213.

[38] W. A. Tiller. *Preferred growth direction of metals*. Journal of Metals 9 (1957), pp. 847–855. DOI: 10.1007/BF03397928.

[39] W. Kurz and D. J. Fisher. *Introduction*. Fundamentals Of Solidification. Trans Tech Publications Ltd., 1984. Chap. 1, pp. 1–14.

[40] Q. Wu, T. Mukherjee, A. De, and T. DebRoy. *Residual stresses in wire-arc additive manufacturing – Hierarchy of influential variables*. Additive Manufacturing 35, no. 101355 (2020). DOI: 10.1016/j.addma.2020.101355.

[41] G. Agarwal. *Study of solidification cracking during laser welding in advanced high strength steels: A combined experimental and numerical approach*. Ph.D. thesis. Delft, South Holland: Delft University of Technology, 2019.

[42] E. M. Van der Aa. *Local cooling during welding: Prediction and control of residual stresses and buckling distortion*. Ph.D. thesis. Delft, South Holland: Delft University of Technology, 2007.

[43] A. Pilipenko. *Computer Simulation of Residual Stress and Distortion of Thick Plates in Multielectrode Submerged Arc Welding: Their Mitigation Techniques*. Ph.D. thesis. Trondheim, Norway: Norwegian University of Science and Technology, 2001.

[44] G. A. Webster and A. N. Ezeilo. *Residual stress distributions and their influence on fatigue lifetimes*. International Journal of Fatigue 23 (2001), pp. 375–383. DOI: 10.1016/S0142-1123(01)00133-5.

[45] Y. Nilsiam, P. Sanders, and J. M. Pearce. *Slicer and process improvements for open-source GMAW-based metal 3-D printing*. Additive Manufacturing 18 (2017), pp. 110–120. DOI: 10.1016/j.addma.2017.10.007.

[46] H. J. Roman, W. Stewart, R. Matthew J., C. Paul, and G. Supriyo. *Residual stress characterization and control in the additive manufacture of large scale metal structures*. Residual Stresses 2016: ICRS-10. Materials Research Forum LLC, 2016, pp. 455–460. DOI: 10.21741/9781945291173-77.

[47] E. L. Frantz. *Low-expansion alloys*. Properties and Selection: Nonferrous Alloys and Special-Purpose Materials. Vol. 2. ASM International, 1990, pp. 889–896. DOI: 10.31399/asm.hb.v02.a0001099.

[48] *The Nobel Prize in Physics 1920*. Accessed: Mar. 04, 2025. Available: https://www.nobelprize.org/prizes/physics/1920/summary/.

[49] E. F. Wassermann. *New developments on the Invar-effect*. Physica Scripta T25 (1989), pp. 209–219. DOI: 10.1088/0031-8949/1989/t25/038.

[50] M. Shiga. *Invar alloys*. Current Opinion in Solid State and Materials Science 1, 3 (1996), pp. 340–348. DOI: 10.1016/S1359-0286(96)80023-4.

[51] E. F. Wassermann. *The Invar problem*. Journal of Magnetism and Magnetic Materials 100, 1–3 (1991), pp. 346–362. DOI: 10.1016/0304-8853(91)90828-X.

[52] Y. Nakamura. *The Invar problem*. IEEE Transactions on Magnetics 12, 4 (1976), pp. 278–291. DOI: 10.1109/TMAG.1976.1059049.

[53] S. Chikazumi, T. Mizoguchi, N. Yamaguchi, and P. Beckwith. *The Invar problem*. Journal of Applied Physics 39, 2 (1968), pp. 939–944. DOI: 10.1063/1.1656337.

[54] T. Yasunori and S. Yûki. *Thermal expansion coefficient of Fe-Ni (fcc) alloys*. Journal of the Japan Institute of Metals and Materials 34, 2 (1970), pp. 228–232. DOI: 10.2320/jinstmet1952.34.2_228.

[55] B. Akgul, M. Kul, and F. Erden. *The puzzling thermal expansion behavior of Invar alloys: a review on process-structure-property relationship*. Critical Reviews in Solid State and Materials Sciences 49, 2 (2023), pp. 254–307. DOI: 10.1080/10408436.2023.2170975.

[56] A. Sahoo and V. R. Medicherla. *Fe-Ni Invar alloys: A review*. Materials Today: Proceedings 43, 2 (2021), pp. 2242–2244. DOI: 10.1016/j.matpr.2020.12.527.

[57] *Standard specification for Iron-Nickel sealing alloys*. ASTM Standard F30-96, 2017. DOI: 10.1520/F0030-96R17.

[58] Carpenter Technology. *Controlled-Expansion Alloys*. CRS Holdings, Inc. Accessed: Mar. 04, 2025. Available: https://www.carpentertechnology.com/hubfs/PDFs/Controlled-ExpansionAlloys.pdf.

[59] W.-S. Chang, Y. Wei, J.-M. Guo, and F.-J. He. *Thermal stability of Ni-Fe alloy foils continuously electrodeposited in a fluorborate bath*. Open Journal of Metal 2 (2012), pp. 18–23. DOI: 10.4236/ojmetal.2012.21003.

[60] G. Cacciamani, A. Dinsdale, M. Palumbo, and A. Pasturel. *The Fe-Ni system: Thermodynamic modelling assisted by atomistic calculations*. Intermetallics 18.6 (2010), pp. 1148–1162. DOI: 10.1016/j.intermet.2010.02.026.

[61] B. S. Lement. *The dimensional behavior of Invar*. Ph.D. thesis. Cambridge, Massachusetts: Massachusetts Institute of Technology, 1949.

[62] S. F. Jacobs, S. C. Johnston, and D. E. Schwab. *Dimensional instability of Invars*. Applied Optics 23, 20 (1984), pp. 3501–3502. DOI: 10.1364/ao.23.3500_1.

[63] W. M. Sokolowski, S. F. Jacobs, M. S. Lane, T. P. O'Donnell, and C. Hsieh. *Quality and reliability for optical systems*. Proceedings of SPIE. 1993. DOI: 10.1117/12.164978.

[64] K. Ona, N. Sakaguchi, H. Ohno, and S. Utsunomiya. *The advanced super Invar alloys with zero thermal expansion for space Telescopes*. Transactions of the Japan Society for Aeronautical and Space Sciences 18, 3 (2020), pp. 32–37. DOI: 10.2322/tastj.18.32.

[65] J. M. Steele, D. A. Thompson, S. F. Jacobs, and D. L. Bass. *Temperature and age effects on the temporal stability of Invar*. Current Developments in Optical Design and Optical Engineering II. 1992. DOI: 10.1117/12.130718.

[66] R. A. Thakar and S. V. Trivedi. *An overview of dimensional stability of Invar 36 material for space based optical mounting applications*. International Conference on Ideas, Impact and Innovation in Mechanical Engineering (ICIIIME 2017). Vol. 5, 6. 2017, pp. 146–151.

[67] C. Chen, B. Ma, S. Miao, and B. Liu. *Effect of cobalt on microstructure and mechanical properties of invar alloy*. Advances in Materials Processing. Ed. by Y. Han. Springer Singapore, 2018, pp. 855–864. DOI: 10.1007/978-981-13-0107-0_84.

[68] V. M. Kalinin, F. N. Dunaev, and V. A. Kornyakov. *Effect of alloying elements on the Curie point of Fe-Ni invar alloys*. Soviet Physics Journal 5 (1970), pp. 129–131. DOI: 10.1007/BF00823460.

[69] M. Tsuda. *Effect of minor alloying elements on the mean thermal expansion coefficient of Fe36Ni invar alloy*. Tetsu-to-Hagane 80.12 (1994), pp. 944–949. DOI: 10.2355/tetsutohagane1955.80.12_944.

[70] H. Saito. *Invar and Invar type alloys*. Physics and Application of Invar Alloys: Honda Memorial Series on Materials Science No. 3. Ed. by H. Saito. Tokyo: Maruzen Company LTD, 1978. Chap. 22, pp. 513–549.

[71] R. J. Smith, G. J. Lewis, and D. H. Yates. *Development and application of nickel alloys in aerospace engineering*. Aircraft Engineering and Aerospace Technology 73, 2 (2001), pp. 138–146. DOI: 10.1108/00022660110694995.

[72] Y. Li, Y. Xiao, L. Yu, K. Ji, and D. Li. *A review on the tooling technologies for composites manufacturing of aerospace structures: materials, structures and processes*. Composites Part A 154, no. 106762 (2022). DOI: 10.1016/j.compositesa.2021.106762.

[73] J. Zhang, G. Lin, U. Vaidya, and H. Wang. *Past, present and future prospective of global carbon fibre composite developments and applications*. Composites Part B: Engineering 250, no. 110463 (2023). DOI: 10.1016/j.compositesb.2022.110463.

[74] F. Ahmad, M. A. Awadh, M. Abas, S. Noor, and A. Hameed. *Optimization of carbon fiber reinforced plastic curing parameters for aerospace application*. Applied Sciences 12, no. 4307 (2022). DOI: 10.3390/app12094307.

[75] F. Veiga, A. Suárez, T. Artaza, and E. Aldalur. *Effect of the heat input on wire-arc additive manufacturing of Invar 36 alloy: Microstructure and mechanical properties*. Welding in the World 66, 6 (2022), pp. 1081–1091. DOI: 10.1007/s40194-022-01295-4.

[76] E. Aldalur, A. Suárez, and F. Veiga. *Thermal expansion behaviour of Invar 36 alloy parts fabricated by wire-arc additive manufacturing*. Journal of Materials Research and Technology 19 (2022), pp. 3634–3645. DOI: 10.1016/j.jmrt.2022.06.114.

[77] C. Qiu, N. J. E. Adkins, and M. M. Attallah. *Selective laser melting of Invar 36: Microstructure and properties*. Acta Materialia 103 (2016), pp. 382–395. DOI: 10.1016/j.actamat.2015.10.020.

[78] H. Tan, Y. Wang, G. Wang, F. Zhang, W. Fan, Z. Feng, and X. Lin. *Investigation on microstructure and properties of laser solid formed low expansion Invar 36 alloy*. Journal of Materials Research and Technology 9, 3 (2020), pp. 5827–5839. DOI: 10.1016/j.jmrt.2020.03.108.

[79] H. Asgari, M. Salarian, H. Ma, A. Olubamiji, and M. Vlasea. *On thermal expansion behavior of invar alloy fabricated by modulated laser powder bed fusion*. Materials and Design 160 (2018), pp. 895–905. DOI: 10.1016/j.matdes.2018.10.025.

[80] N. J. Harrison, I. Todd, and K. Mumtaz. *Thermal expansion coefficients in Invar processed by selective laser melting*. Journal of Materials Science 52, 17 (2017), pp. 10517–10525. DOI: 10.1007/s10853-017-1169-4.

[81] M. Yakout, M. A. Elbestawi, and S. C. Veldhuis. *A study of thermal expansion coefficients and microstructure during selective laser melting of Invar 36 and stainless steel 316L*. Additive Manufacturing 24 (2018), pp. 405–418. DOI: 10.1016/j.addma.2018.09.035.

[82] G. Jiao, X. Fang, X. Chen, N. Xi, M. Zhang, Y. Liu, H. Wu, and K. Huang. *The origin of low thermal expansion coefficient and enhanced tensile properties of Invar alloy fabricated by directed energy deposition*. Journal of Materials Processing Technology 317, no. 117994 (2023). DOI: 10.1016/j.jmatprotec.2023.117994.

[83] G. Jiao, X. Fang, X. Li, M. Zhang, Z. Zhang, H. Li, and K. Huang. *High performance ultrasonic vibration assisted Wire-arc directed energy deposition of Invar alloy*. Journal of Materials Processing Technology 332, 118543 (2024). DOI: 10.1016/j.jmatprotec.2024.118534.

[84] G. Huang, G. He, Y. Liu, and K. Huang. *Anisotropy of microstructure, mechanical properties and thermal expansion in Invar 36 alloy fabricated via laser powder bed fusion*. Additive Manufacturing 82, no. 104025 (2024). DOI: 10.1016/j.addma.2024.104025.

3

EXPERIMENTAL METHODOLOGY

THIS chapter describes the materials used in the present study, the experimental setup, and the processing parameters. In addition, an overview of the methods and characterisation tools used to study the microstructure, melt pool behaviour, and functional properties is also given. The procedures and techniques outlined here are adapted and applied as appropriate in the following chapters.

3.1. MATERIAL OVERVIEW

A 1.2 mm diameter wire of the low thermal expansion alloy 36 was used in this study. The wire is commercially known as 3Dprint AM Mold 36 or alloy Fe-Ni36 and is manufactured by voestalpine Böhler Welding. In addition, a high Ni wire was utilised to tailor the Ni content, i.e. the thermal expansion properties, through a twin-wire deposition approach. This wire is commercially known as UTP A 80 Ni and has the same manufacturer and diameter as the alloy 36 wire. The chemical composition of these wires as stated by the manufacturer and measured using energy dispersive spectroscopy (EDS) are listed in Table 3.1. The Ni content in the alloy 36 wire is measured to be close to 36 wt.%, which agrees well with the manufacturer's specifications. The Ni content in the alloy 36 wire is critical as it governs the thermal expansion behaviour of the alloy. The S and P content in the wire is observed in low concentrations, which is beneficial in promoting the weldability of this alloy specifically in the context of solidification cracking [1, 2]. Elements such as Mn, Mo, Cr and Si are added to improve the workability, mechanical properties, and weldability of alloy 36 [3–6]. In comparison, the addition of Co to Fe–Ni LTE alloys, where the added Co partly substitutes the Ni content, results in alloys with a lower linear coefficient of thermal expansion (CTE) while possessing a higher Curie temperature compared to binary Fe–Ni alloys [7, 8]. In addition, the Ni wire contains around 3.3 wt.% of Ti, and is used in conjunction with the alloy 36 wire during twin-wire experiments in this study. As mentioned in section 2.3, the addition of Ti can increase the thermal expansivity of alloy 36. However, the Ni wire is fed at low feeding rates to the melt pool relative to the alloy 36 wire, as will be shown in chapter 5. Hence, its contribution in raising the thermal expansivity of the deposited alloy composition will be marginal.

Table 3.1: Chemical composition of the feedstock wires used in the present study, as stated by the manufacturer and measured using EDS. * indicates that the chemical contents are below the stated value.

Elements, wt.%	Si*	Mn	Cr*	Mo*	Co*	P and S	Ni	Ti	Fe
Alloy 36									
Manufacturer	0.10	0.20	0.50	0.50	1.00	0.01	34–38	-	Bal.
EDS result	0.14	0.32	0.10	0.12	0.40	0.01	36.10	-	62.81
UTP A 80 Ni									
Manufacturer	0.30	0.30	-	-	-	-	Bal.	3.30	0.10
EDS result	0.32	0.27	-	-	-	-	95.88	3.38	0.15

3.2. EXPERIMENTAL SETUP

The deposition was performed using the gas tungsten arc welding (GTAW) process in the cold wire condition. A commercially available Migatronic TIG commander 400 AC/DC power source was used for the GTAW-based AW-DED process. The pulsed current setting in the direct-current electrode-negative (DCEN) configuration was used during the experiments. A wire feeding assembly connected to an independent Migatronic KT4 wire feeder was mounted on the welding torch for the purpose of supplying the feedstock material. In the case of twin-wire feeding experiments, two wire feeding units were used in conjunction to simultaneously supply alloy 36 and Ni-rich wires.

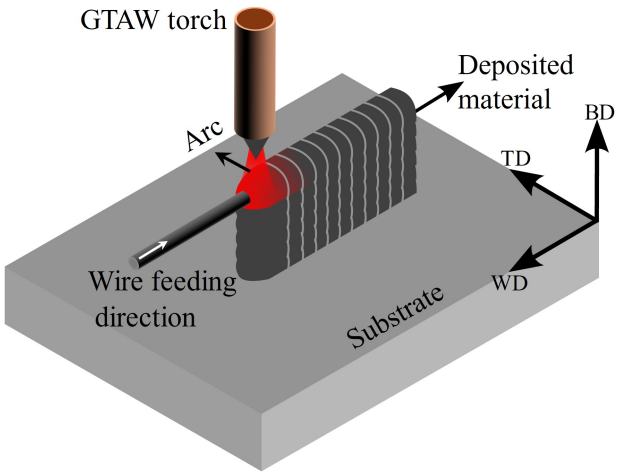

Figure 3.1: Schematic diagram of the GTAW-based AW-DED process employed in this study. The building, welding/travel, and transverse directions are denoted by BD, WD, and TD, respectively.

The schematic of the GTAW-based AW-DED set-up employed in this study is

shown in Figure 3.1. The GTAW torch was positioned perpendicular to the substrate. The torch and the substrate were controlled through separate servo-motors allowing for an independent 3-axis motion. The shielding from the ambient environment was achieved using an inert argon gas supply at a flow rate of 10 L min^{-1}. The non-consumable electrodes employed in this study were 3.2 mm in diameter and chemically composed of tungsten alloyed with rare earth oxides (E3 electrodes, purple colour). A front wire feeding approach was adapted due to the observed geometrical stability of the beads deposited in this approach as established in other works [9–11]. Moreover, these studies have also reported improved bead stability when the liquid metal transfer from the wire to the melt pool occurs in continuous metal transfer mode, compared to intermittent metal transfer mode, which may involve bridging or free flight transfer of droplets. The details of these deposition modes will be presented and discussed in chapter 5. The current and voltage profiles during the deposition process were measured using a Triton data logger at a sampling rate of 5 kHz. This data was used to calculate the instantaneous power (IP) based on equation 3.1,

$$IP = \frac{1}{n}\sum_{i=1}^{n}(I_i \cdot U_i), \tag{3.1}$$

and in conjunction with equation 3.2,

$$HI = \frac{IP \cdot \eta}{TS}, \tag{3.2}$$

for determining the heat input (HI), assuming a process efficiency (η) of 0.7 [12]. In equations 3.1 and 3.2, I_i is the instantaneous current in A, U_i is the instantaneous voltage in V, and TS is the travel speed in mm s^{-1}. The process parameters of this study were established on the basis of the dimensional stability of the weld beads obtained during initial bead-on-plate experiments. To achieve different HI values, both current and travel speeds were adjusted simultaneously, as can be seen from the process parameters corresponding to the five HI conditions listed in Table 3.2. In addition, the wire feed speed was adjusted in accordance with the HI level to maintain a stable deposition process. An arc length of 3–3.5 mm was maintained for the parameters corresponding to conditions A through C, while an arc length of 4–4.5 mm was maintained in conditions D and E. This resulted in slightly different average arc voltages for each HI condition, as listed in Table 3.2.

3.3. LIQUID METAL TRANSFER CHARACTERISATION

The liquid metal transfer characteristics during GTAW-based AW-DED were investigated using a specialised camera and illumination system. A Cavitar C300 welding camera was used for this purpose. This camera is equipped with a pulsed laser illumination system of 645 ± 10 nm wavelength. A narrow optical band pass filter is also incorporated in the camera for spectral filtering of the optical radiation from the welding arc. The gain and the exposure settings on the camera can be adjusted to optimise the image quality. The maximum achievable recording rate of the camera with the laser illumination is limited to 100 frames per second.

Table 3.2: Process parameters used in this study during GTAW-based AW-DED. TS: travel speed, WFS: wire feed speed, I_{base}: base current, I_{peak}: peak current, t_{base}: base time, t_{peak}: peak time, U_{ave}: average voltage, HI: heat input.

Parameters	TS mm s^{-1}	WFS mm s^{-1}	I_{base} A	I_{peak} A	t_{base} s	t_{peak} s	U_{ave} V	HI J mm^{-1}
A	4.6	22	81	180	0.20	0.20	10.0	200
B	4.5	28	110	220	0.20	0.15	10.3	250
C	3.8	30	120	240	0.20	0.20	10.6	350
D	3.5	39	133	265	0.20	0.20	11.4	450
E	3.3	50	135	300	0.20	0.20	12.0	550

3.4. MICROSTRUCTURE CHARACTERISATION

Optical microscopy

The microstructures of the as-deposited alloys were studied following chemical etching. Sample surfaces parallel to the BD-TD plane (Figure 3.1) were analysed. Standard metallographic procedures involving mechanical grinding and polishing were followed to prepare the surface. Polished samples were chemically etched to reveal the grain structure using Kalling's No. 1 (distilled water, $CuCl_2$, HCl, and $CH3_3CH_2OH$), and Kalling's No. 2 reagents, which is compositionally identical to No.1 but without distilled water. These etchants successfully revealed the grain boundaries and substructure of the grains as shown in Figure 3.2. Following the etching process, the surfaces were cleaned with 2-propanol and blow-dried using hot air. A Keyence VHX-5000 digital microscope was used to study the etched surfaces. Quantitate analyses comprising grain size, geometrical characteristics, and crack length in the observed microstructures were performed using the microscope built-in software and ImageJ software.

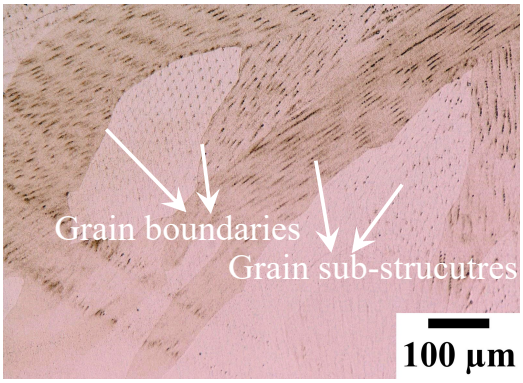

Figure 3.2: The chemically etched microstructure of as-deposited alloy 36 revealing the constituent features.

Scanning electron microscopy

The samples in polished condition were observed using a scanning electron microscope (SEM) equipped with an energy dispersive spectroscopy (EDS) detector to study the chemical composition. Elemental maps and quantitative information about the chemical composition of as-deposited alloys were obtained through SEM-EDS. A ThermoFisher Scientific Helios G4 Plasma FIB UXe SEM (Helios-SEM) was used for this purpose at acceleration voltages of 10–20 kV and beam currents of 0.80–6.40 nA. The typical detection limit of EDS is 1000 ppm for higher atomic number (> 8) elements [13]. Thus, this technique can reveal meaningful information about the chemical make-up of LTE Fe–Ni alloys.

Electron backscatter diffraction

Electron backscatter diffraction (EBSD) is a SEM-based technique that provides information on microstructural-crystallographic orientations [14]. This technique is widely utilised to obtain grain orientations and phase compositions in crystalline or quasi-crystalline materials. The samples to be studied using EBSD were polished with a colloidal silica suspension in addition to the preparation procedure mentioned above. This polishing step was necessary to remove any accumulated damage from previous sample preparation steps and create a surface suitable for EBSD analysis. The Helios-SEM is equipped with an AMETEK-EDAX EBSD detector and was used for fine step-size EBSD analysis, with a step size ranging from 0.05–1 µm, depending on the feature size under observation. The acceleration voltage and beam current during these scans were 10 kV and 6.4 nA, respectively. The EDAX OIM Analysis version 8 software package was used to post-process the collected data. A standard cleanup routine consisting of grain confidence index standardisation, neighbour orientation correlation, and single average orientation per grain was applied while processing the grain and phase maps. For the kernel average misorientation (KAM) maps, the cleanup was limited to grain confidence index standardisation. In addition, coarse step-size scans were performed using a JEOL 7200F field emission SEM equipped with a Oxford Instruments EBSD detector. A step size of 5 µm was used to scan areas of 5.2×4.6 mm^2 during these scans. The data obtained were post-processed in the Aztec HKL software version 6.1. The acceleration voltage and beam current during these EBSD scans were 15 kV and 3.2 nA, respectively.

X-ray diffraction

The constituent phases and crystal structure of the as-deposited alloys were evaluated using X-ray diffraction (XRD). This technique is based on the principle of elastic scattering of X-rays from the atomic planes of a sample under investigation [15]. The scattered waves that satisfy the Bragg criteria interfere constructively, leading to a diffraction pattern, thus revealing crystallographic information [16]. A Bruker D8 Advance diffractometer in the Bragg-Brentano geometry was used in this study for the purpose of phase analysis [15]. The instrument utilised Cu Kα radiation operated at a current and voltage of 40 mA and 45 kV, respectively. Coupled $2\theta/\theta$ scans were performed with a 2θ step size of 0.04° and counting time of 0.5 s per step. The data was post-processed using the Bruker software DiffracSuite.EVA version 5.2. In

addition, XRD was also utilised to evaluate the lattice parameters of the as-deposited samples. In this case, the employed instrument was similar to the above-mentioned diffractometer but utilised Co Kα radiation instead of Cu Kα radiation. The diffraction patterns were generated from coupled 2θ/θ scans and post-processed using the instrument software DiffracSuite.EVA version 7.2. The acquisition parameters during these scans were a 2θ step size of 0.035° and a counting time of 5 s per step. The lattice parameters were obtained by correlating the values of the trial lattice parameter of each diffraction peak with the Nelson-Riley extrapolation function [17]. The result of an XRD measurement performed on the as-received alloy 36 wire is shown in Figure 3.3. The pattern reveals only austenitic-fcc (face-centred cubic) phase peaks in the wire, thus establishing it as a single-phase material.

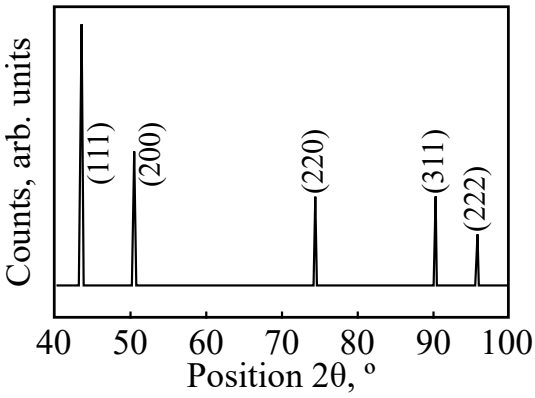

Figure 3.3: The X-ray diffraction pattern of the as-received alloy 36 wire showing a single-phase fcc crystal structure.

3.5. FUNCTIONAL PROPERTIES

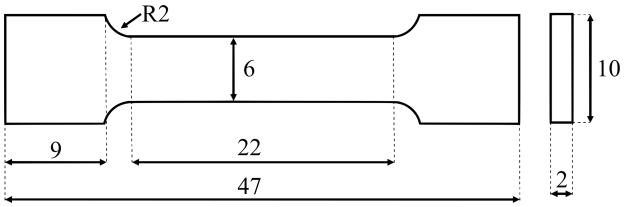

Figure 3.4: Schematic diagram of the flat dog-bone specimens used in the present study to quantify the tensile properties. All dimensions are in mm.

Mechanical testing and hardness

The as-deposited alloys were mechanically characterised through uniaxial tensile tests. Flat dog-bone shaped specimens, shown schematically in Figure 3.4, were

machined by wire-electronic discharge machining (W-EDM). The specimen geometry and testing procedures were based on the guidelines outlined in the ISO 6892-1 standard [18]. The specimens were extracted in two sets, with their lengths oriented parallel to the building and the welding/travel directions, respectively, to quantify and compare the tensile properties in these two directions. Tensile tests were performed at room temperature using an INSTRON® 5500R machine in displacement controlled mode. The displacement rate imposed by the machine during the tensile tests was 1 mm min^{-1}. The displacement of the specimens was recorded using an INSTRON® dynamic axial clip-on extensometer of 12.5 mm gauge length. Following the tests, the fracture surfaces were analysed using a JEOL JSM-IT100 SEM at an acceleration voltage in the range of 15–20 kV.

A Struers DuraScan hardness testing machine was employed to quantify the microhardness of the as-deposited alloy using the HV_1 test method. In this method, a downward force of 9.81 N is exerted on the surface of the specimen by a diamond pyramid indenter with a square base. A built-in optical microscope is then used to measure the lengths of the two diagonals of the indentation. The average of these diagonal lengths, together with the applied load, is used to calculate the Vickers hardness value. Measurements were performed on polished sample surfaces according to the testing procedure guidelines stated in the ASTM E92-17 standard [19].

Dilatometry

Dilatometry was performed to evaluate the mean linear coefficients of thermal expansion (CTE) and the Curie temperatures of the as-deposited low thermal expansion alloys. A Linseis TMA PT1000 thermomechanical analyser was used to determine the linear CTE. The TMA PT1000 uses a resistance furnace and a high-resolution linear variable differential transformer (LVDT) displacement sensor connected to a quartz piston and sample stage. Cylindrical specimens of ϕ4 mm and 10 mm length were machined using W-EDM. Two sets of specimens were prepared, with their lengths oriented parallel to the building and welding (travel) directions, respectively, to quantify and compare the CTE in these two directions. The furnace was filled with argon gas during the measurements to create an inert environment. A heating rate of 5 °C min^{-1} was used during these experiments and the testing procedure was in accordance with the guidelines stated in the ASTM E831-19 standard [20]. The average linear CTE were calculated based on the temperature-displacement curves by equation 3.3,

$$\alpha = \frac{1}{L_0}\frac{dL}{dT}, \tag{3.3}$$

where, α represents the mean CTE in the desired temperature interval; L_o is the initial length of the specimen; dL is the change in length of the specimen accompanied by the temperature variation (dT). The Curie temperatures of the as-deposited alloys were also determined using a Bähr 805 A/D dilatometer. Different to the principle of dilatometers that rely on furnace-based heating, this apparatus utilises two quartz rods connected to a LVDT displacement sensor to record the thermal expansion of a sample during heating by an induction coil. Throughout the heating process, the temperature and thermal expansion are recorded simultaneously along with the power

delivered to the induction coil. The Curie transition can be located by analysing the power signal during a measurement. Below Curie temperature, an induction coil heats a ferromagnetic material through the mechanisms of Joule heating and hysteresis heating [21]. However, the latter mechanism only contributes up to the Curie temperature. Therefore, the instrument delivers additional power to maintain the heating rate applied during the test. This manifests as a sudden increase in the supplied power at the Curie transition and is therefore referred to as the energy jump method for the determination of the Curie temperature [21]. Following the test, the recorded power signal is analysed to identify the temperatures before and after the power jump. The average of these temperatures is then calculated to ascertain the Curie temperature. For these experiments, cylindrical specimens of ϕ3.5 mm and 10 mm length, were machined using W-EDM with their lengths oriented parallel to the travel/welding direction. The tests were performed under vacuum at a heating rate of 10 °C min^{-1}.

In the present work, the furnace-heated dilatometer was preferred for CTE measurements of LTE alloys, based on preliminary experiments. Specimens were taken from a commercially available alloy 36 plate with known CTE values in different temperature ranges. The specimens were tested with both induction-heated (IH) and furnace-heated (FH) dilatometers. The corresponding CTE values measured in different temperature ranges using the two dilatometers are compared inin Table 3.3. It is evident that the CTE values of alloy 36 measured by an FH dilatometer are a better match to the material specifications compared to those obtained from the IH dilatometer. The discrepancy between the CTE measurements obtained from the two dilatometers is attributed to the suitability of the IH dilatometer being limited to high-temperature measurements(> 500 °C). Moreover, the IH dilatometer operates on the principle of electromagnetic induction, generating both heat and alternating magnetic fields. These magnetic fields may influence the magnetovolume effects in alloy 36 below its Curie temperature by perturbing the intrinsic spin structure of the material. Hence, to minimise instrumental effects and measurement errors in the CTE data, an FH dilatometer was employed in the subsequent chapters.

Table 3.3: The mean linear CTE of a commercially available alloy 36 in different temperature ranges measured using induction- and furnace-heated dilatometers.

Mean CTE, µm m^{-1} °C^{-1}	Temperature Range, °C		
	20–100	20–150	20–260
IH Dilatometer	2.04	2.50	5.12
FH Dilatometer	1.36	2.01	4.67
Material Specification [22]	1.30	2.11	4.18

REFERENCES

[1] A. J. Ramirez and J. C. Lippold. *New insight into the mechanism of ductility-dip cracking in Ni-base weld metals.* Hot Cracking Phenomena in Welds. Ed. by

T. Böllinghaus and H. Herold. Berlin: Springer-Verlag, 2005, pp. 19–41. DOI: 10.1007/3-540-27460-X_2.

[2] S. M. Abbasi, M. Morakabati, R. Mahdavi, and A. Momeni. *Effect of microalloying additions on the hot ductility of cast FeNi36*. Journal of Alloys and Compounds 639 (2015), pp. 602–610. DOI: 10.1016/j.jallcom.2015.03.167.

[3] K. A. Yushchenko, N. I. Kakhovskii, and T. M. Starushchenko. *Effect of alloying of the seam metal on properties of weldments in invar alloys*. Metal Science and Heat Treatment 16 (1974), pp. 866–869.

[4] H. Liu, Z. Sun, G. Wang, X. Sun, J. Li, F. Xue, H. Peng, and Y. Zhang. *Effect of aging on microstructures and properties of Mo-alloyed Fe-36Ni invar alloy*. Materials Science and Engineering: A 654 (2016), pp. 107–112. DOI: 10.1016/j.msea.2015.12.018.

[5] J. C. Tverberg. *The role of alloying elements on the fabricability of austenitic stainless steel*. Accessed: Mar. 12, 2025. Available: https://www.csidesigns.com/uploads/white-papers/fabtech.pdf. 2000.

[6] M. Tsuda and K. Wang. *The effect of alloying elements on the mechanical properties of the Fe-36% Ni alloys*. Tetsu-To-Hagane 82, 8 (1996), pp. 701–706.

[7] D. A. Colling. *Influence of cobalt on Invar characteristics of iron-nickel alloys*. AIP Conference Proceedings 3. 1972, pp. 188–194. DOI: 10.1063/1.2948556.

[8] C. Chen, B. Ma, S. Miao, and B. Liu. *Effect of cobalt on microstructure and mechanical properties of invar alloy*. Advances in Materials Processing. Ed. by Y. Han. Springer Singapore, 2018, pp. 855–864. DOI: 10.1007/978-981-13-0107-0_84.

[9] T. Ungethüm, E. Spaniol, M. Hertel, and U. Füssel. *Analysis of metal transfer and weld geometry in hot-wire GTAW with indirect resistive heating*. Welding in the World 64 (2020), pp. 2109–2117. DOI: 10.1007/s40194-020-00986-0.

[10] H.-K. Lee and K.-H. Yun. *A Study on the applicability of A-TIG welding of semi-automatic cold wire feeding process for cryogenic stainless steel pipes*. Journal of Welding and Joining 42, 3 (2024), pp. 231–238. DOI: 10.5781/jwj.2024.42.3.1.

[11] D. Ding, Z. Pan, D. Cuiuri, and H. Li. *Wire-feed additive manufacturing of metal components: Technologies, developments and future interests*. The International Journal of Advanced Manufacturing Technology 81, 1-4 (2015), pp. 465–481. DOI: 10.1007/s00170-015-7077-3.

[12] S. Kou. *Heat flow in welding*. Welding Metallurgy. 3rd ed. John Wiley & Sons, 2021. Chap. 2, pp. 37–60.

[13] M. Hirobumi, S. Marks, and I. Anderson. *The recent resolution and detection limit improvement of EDS and EBSD with SEM*. IEEE International Meeting for Future of Electron Devices, Kansai (IMFEDK). Kyoto: IEEE, 2019, pp. 51–54.

[14] G. Qian, Y. Li, and A. R. Gerson. *Applications of surface analytical techniques in Earth Sciences*. Surface Science Reports 70 (2015), pp. 86–133. DOI: 10.1016/j.surfrep.2015.02.001.

[15] M. E. Fitzpatrick, A. T. Fry, P. Holdway, F. A. Kandil, J. Shackleton, and L. Suominen. *Principles*. Determination of residual stresses by X-ray diffraction. NPL UK, 2002. Chap. 5, pp. 5–12.

[16] F. Adams. *X-ray absorption and diffraction | overview*. Encyclopedia of Analytical Science. Ed. by P. Worsfold, A. Townshend, and C. Poole. 2nd ed. Oxford: Elsevier, 2005, pp. 365–377. DOI: 10.1016/B0-12-369397-7/00668-3.

[17] J. B. Nelson and D. P. Riley. *An experimental investigation of extrapolation methods in the derivation of aaccurate unit-cell dimensions of crystals*. Proceedings of the Physical Society 57, 3 (1945), pp. 160–177. DOI: 10.1088/0959-5309/57/3/302.

[18] *Metallic materials-Tensile testing-Part 1: Method of test at room temperature*. ISO Standard 6892-19, 2019.

[19] *Test methods for vickers hardness and knoop hardness of metallic materials*. ASTM Standard E92-17, 2017.

[20] *Standard test method for linear thermal expansion of solid materials by thermomechanical analysis*. ASTM Standard E831-19, 2019.

[21] A. Verma, M. Sundararaman, J. B. Singh, and S. A. Nalawade. *A new method for determining the curie temperature using a dilatometer*. Measurement Science and Technology 21, no. 105106 (2010). DOI: 10.1088/0957-0233/21/10/105106.

[22] Carpenter Technology. *Controlled-Expansion Alloys*. CRS Holdings, Inc. Accessed: Mar. 04, 2025. Available: https://www.carpentertechnology.com/hubfs/PDFs/Controlled-ExpansionAlloys.pdf.

4

MICROSTRUCTURE AND FUNCTIONAL BEHAVIOUR OF ALLOY 36[‡]

THE low thermal expansion alloy 36 was deposited using cold wire gas tungsten arc welding in a range of heat inputs. Intergranular cracking prevailed in the as-deposited microstructures, the extent of which was reduced by decreasing the heat input. Abnormal grain coarsening and strain localisation at grain boundaries were promoted as heat input increased, which increased the susceptibility of the alloy to intergranular cracking. Consequently, the increase in heat input adversely affected the tensile properties of the alloy, as intergranular cracking led to premature failure. However, the characteristic low thermal expansion behaviour of alloy 36 remained unaffected by heat input.

4.1. INTRODUCTION

The binary Fe–Ni system presents a class of functional alloys characterised by a uniquely low thermal expansion behaviour. The minimum mean linear coefficient of thermal expansion (CTE) in the binary Fe–Ni system is observed at a Ni content of about 36 wt.% (alloy 36) [1]. For comparison, the mean CTE values of alloy 36 and stainless steel 316L in an approximate temperature range of 20–100 °C are $1.60\,\mu m\,m^{-1}\,°C^{-1}$ and $16\,\mu m\,m^{-1}\,°C^{-1}$, respectively [2, 3]. As such, alloy 36 is used in precision instruments, aerospace moulding tools, and cryogenic storage and transport tanks [4–6]. Alloy 36 products in the aerospace sector are traditionally fabricated using subtractive processes [7]. However, machining of alloy 36 can be challenging

[‡]The contents of this chapter are in part based on a journal article published as: A. Sood, J. Schimmel, V. M. Ferreira, M. Bosman, C. Goulas, V. Popovich, and M. J. M. Hermans. *Directed energy deposition of Invar 36 alloy using cold wire pulsed gas tungsten arc welding: Effect of heat input on the microstructure and functional behaviour*. Journal of Materials Research and Technology 25 (2023), pp. 6183–6197.

due to certain physical aspects of this alloy, such as high work hardening rates and low thermal conductivity [8]. Furthermore, subtractive techniques often result in the generation of significant material waste [9, 10]. In this regard, additive manufacturing (AM) techniques present a suitable alternative, as they are not associated with such drawbacks [11].

Recently, multiple studies have emerged that address the microstructure and properties of alloy 36 fabricated by laser-powder processing [8, 12–17]. In contrast to this, the body of literature pertaining to AW-DED of alloy 36 is limited [18–20]. The literature pertaining to the welding of alloy 36, especially multi-pass welds, can help predict the behaviour of alloy 36 in a process like AW-DED, since it is essentially based on the principles of welding. Among these studies, a common observation is the presence of intergranular cracks [5, 21–23]. Naturally, such defects are undesirable and may lead to premature failure during the service life of a product in load-bearing applications. Therefore, to further establish the application of AW-DED to alloy 36 there is an explicit need to develop an understanding of the resulting microstructure and properties. To build on this, a systematic experimental study was performed followed by extensive characterisation to understand the response of alloy 36 to AW-DED. Gas tungsten arc welding (GTAW) was used to deposit blocks using a commercially available alloy 36 wire at five heat inputs ranging from 200 J mm^{-1} to 550 J mm^{-1}. The effect of heat input on the microstructure and chemical composition of the deposited blocks was investigated. Lastly, two larger blocks were deposited at the extremes of the heat input, i.e. 200 J mm^{-1} and 550 J mm^{-1}, to quantify the mechanical properties and linear CTE of the as-deposited alloy 36.

4.2. EXPERIMENTAL OVERVIEW

Blocks of 80 × 15 × 15 mm^3 were deposited using a commercially available alloy 36 wire of 1.2 mm diameter. The chemical composition of this wire and the process parameters corresponding to the deposited blocks can be found in Tables 3.1 and 3.2, respectively (section 3.1). Bead-on-plate experiments were performed prior to deposition of the blocks at various heat inputs to measure the dimensional characteristics of the beads using optical microscopy. The maximum inter-pass temperature was limited to approximately 150 °C during the deposition and was monitored using a K-type thermocouple [24]. Following deposition, four transverse sections were taken from each block at similar locations to observe the microstructure. The extracted specimens were prepared according to the procedures stated in section 3.4 (chapter 3), for the purpose of optical microscopy, SEM analysis, XRD, XRF, and hardness measurements.

The as-deposited alloy 36 at the lower and upper extremes of the heat input range was also analysed using EBSD. A step size of 0.5 µm was used to map areas of 1 × 1 mm^2 during the scans. The current and the acceleration voltage were 3.2 nA and 20 kV, respectively. Lastly, tensile and dilatometric tests were performed on specimens extracted from two larger blocks of 150 × 20 × 60 mm^3 deposited at the upper and lower extreme of the heat input range, hereafter referred to as blocks A1 and E1. Detailed information on the techniques used to characterise the microstructure and functional properties is given in sections 3.4 and 3.5, respectively.

4.3. RESULTS AND DISCUSSION

4.3.1. DEPOSITION AND MICROSTRUCTURE OF ALLOY 36

The dimensional characteristics of the bead-on-plate welds corresponding to the five heat inputs used to deposit the blocks are shown in Figures 4.1 (a) and (b). In general, the weld bead size and wetting angle increase with heat input, owing to higher deposition rates resulting from the progressively increased wire feed speed. The maximum wetting angle corresponds to the highest heat input condition, 550 J mm^{-1}, and is limited to 45 °. This aspect is critical during AW-DED, and an optimal range can aid in the prevention of defects related to lack of fusion. The relatively low scatter in the dimensional characteristics shown in Figures 4.1 (a) and (b) indicates uniformity in the geometry of the beads. Hence, the process parameters corresponding to these beads are considered optimum for the deposition of multi-bead structures by AW-DED.

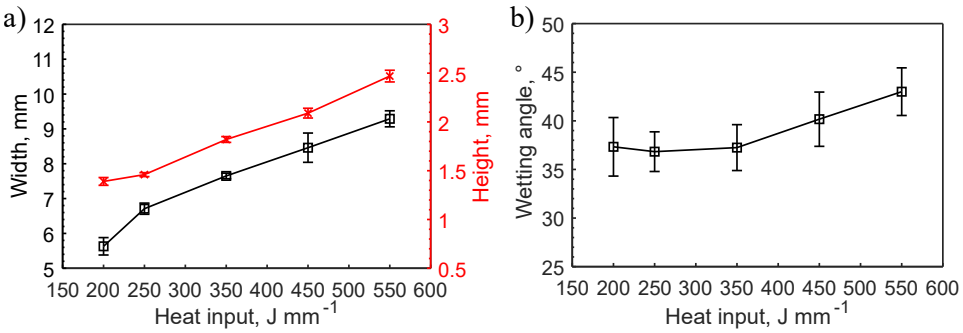

Figure 4.1: Dimensions and wetting angle of the bead-on-plate welds corresponding to the five heat inputs used for the deposition of the blocks, in (a) and (b), respectively.

The macroscopic overview of the blocks deposited at five heat inputs, referred to as blocks A to E, is shown in Figures 4.2 (a-0 to e-0), respectively. The corresponding microstructural characteristics observed at similar locations in the blocks are highlighted in Figures 4.2 (a-1 to e-1). In general, the blocks consist of columnar grains that extend through multiple layers. Columnar grains grow epitaxially in the blocks and tend to be orientated parallel to the building direction, as grain formation is favoured along the direction of maximum heat flow [25]. The substructure mainly comprises cellular features as highlighted in Figures 4.2 (a-1) to (e-1), with the occasional presence of columnar dendritic features. The different substructures arise from local variations in the solidifying conditions in the melt pool from the combined effect of the temperature gradient (G) and the growth rate of the solid-liquid interface (R), as illustrated in section 2.2 (chapter 2). Locally varying solidification conditions are expected, since the blocks were deposited in the pulsed current mode, which would likely lead to a relative acceleration and deceleration of the solid-liquid interface during the low- and high-current phases. Moreover, such grain features have typically been observed in the microstructure of the single-phase austenitic alloy 36 fabricated by AM methods [13, 26, 27].

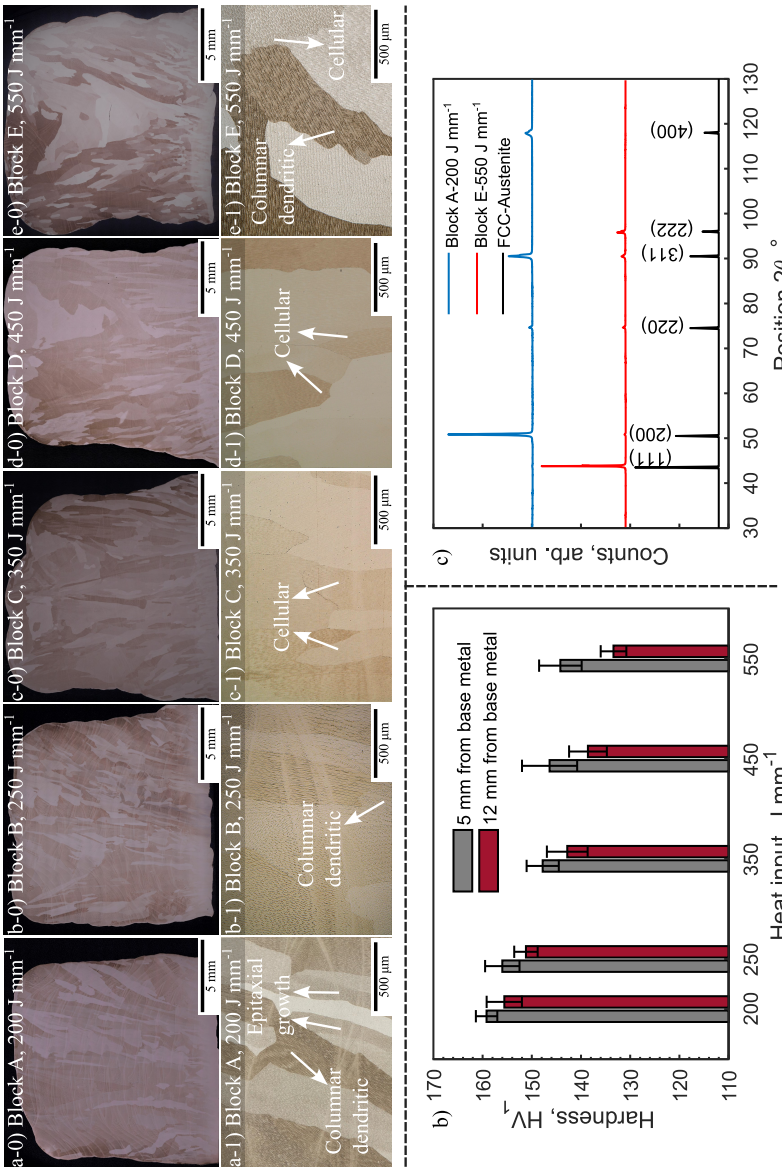

Figure 4.2: Macroscopic overview and microstructural characteristics of the as-deposited blocks, shown in (a-0) to (e-0) and (a-1) and (e-1), respectively. The microhardness of the as-deposited alloy 36 at five heat inputs measured from the transverse cross-sections at 5 mm and 12 mm from the substrate in (b), and the XRD patterns of the blocks deposited at the lower and upper extreme of the heat input range in (c).

In the case of block E, extensive grain coarsening is observed in the upper half of the block. The difference in the morphology and size of the grains observed in blocks A and E is evident when comparing Figures 4.2 (a-0) and (e-0). This is reflected in the microhardness measurements as shown in Figure 4.2 (b). The tendency for grain coarsening during deposition becomes more pronounced with increasing heat input, as block E exhibits the largest hardness difference between 5 mm and 12 mm from the substrate. In comparison, block A shows a relatively uniform distribution of hardness, which is indicative of a homogeneous microstructure at different heights along the building direction.

The average grain width in blocks A and E was quantified from the transverse sections using the linear intercept method [28]. The results are shown in Table 4.1 and corroborate the trend observed in the hardness measurements, implying that the decrease in hardness with increasing heat input is a consequence of an increase in the average grain width. According to the equilibrium binary Fe–Ni phase diagram (shown in section 2.3), alloy 36 remains in the austenitic phase field in a broad temperature range (~ 450 °C–1400 °C) [29]. In addition, alloy 36 tends to have a low thermal diffusivity, implying that thermal energy is likely to accumulate over time [30]. The cooling rate during AW-DED decreases when the heat input is increased, as the cooling rate varies inversely with the heat input [31]. The reduction in cooling rate subjects the single-phase alloy 36 to elevated temperatures for longer periods, consequently facilitating grain growth [32]. Therefore, increasing the heat input from 200 J mm^{-1} towards 550 J mm^{-1} was found to induce grain coarsening during the deposition of alloy 36, thereby reducing the hardness of the as-deposited alloy.

Table 4.1: Average grain width in blocks A and E as determined from the transverse cross-sections.

Grain width, µm	Distance from base plate	
	5 mm	12 mm
Block A	270 ± 30	310 ± 20
Block E	390 ± 40	1120 ± 200

The blocks deposited at the lowest and highest heat inputs were analysed using XRD, and the resulting patterns are presented in Figure 4.2 (c). The blocks are found to be entirely austenitic, which is expected in alloy 36 as the binary Fe–Ni alloy system exists in the fcc structure above a Ni content of 30 at.% [33]. Beyond this Ni content, the transformation to the bcc α-phase is extremely sluggish and realistically impossible during the timescales associated with AW-DED. However, the indices of the maximum intensity peaks differ for block A and E in the figure. In block A, the peak with the maximum intensity is a result of reflections from the (100) planes, whereas, in block E it is due to the reflections from (111) planes. This occurs due to the difference in the grain morphology, as shown in Figures 4.2 (a-0) and (e-0), and the orientation of the grains between blocks A and E. The microstructure of block E is not homogeneous throughout the build as severe grain coarsening is observed in block E.

The high heat input used for the deposition of block E led to this grain coarsening, since the microstructure of block A is observed to be relatively homogeneous after being deposited at a much lower heat input. Consequently, the large grains in block E may have dominated the Bragg criteria leading to the maximum reflection intensity from the (111) planes. However, the maximum intensity from the (200) planes is expected in the case of block A, as for cubic alloys the preferential grain growth direction is <100> [34, 35].

The results of the XRF analysis performed on the five blocks are shown in Figure 4.3. The Ni content in all blocks was found to be maintained in the vicinity of 36 wt.%, meaning that the increase in heat input did not lead to elemental loss. This is a critical aspect in Fe–Ni LTE alloys, as the lowest thermal expansion is observed at approximately 36 wt.% of Ni. The other major alloying elements were also observed to agree with the chemical composition limits of the as-received feedstock wire.

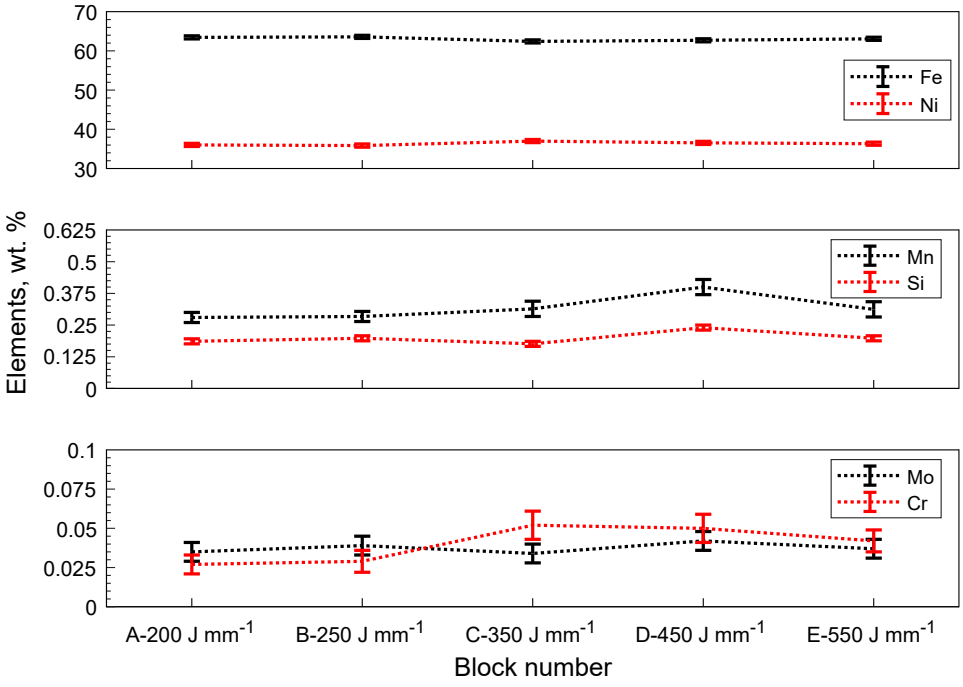

Figure 4.3: Major alloying elements in alloy 36 deposited at various heat inputs.

4.3.2. CHARACTERISATION OF CRACKING

The blocks deposited at heat inputs ranging from 250–550 J mm^{-1} were found to be susceptible to intergranular cracking. The effect of heat input on the intensity of cracking is quantified in Figure 4.4 (a). The total crack length per block, quantified from four cross-sections, is used as a qualitative indicator for the susceptibility to cracking and is found to increase with increasing heat input. Depending on the heat

input, the nature of cracking observed in this study can be distinguished into micro- and macro-cracking, as shown for the heat input conditions of 250 and 550 J mm^{-1} in Figure 4.4 (b). The transition from micro-cracking to macro-cracking occurred above a heat input of 350 J mm^{-1} (block C). In the case of block B, the grain boundaries were generally found to be decorated with voids, along with micro-cracks, as shown for the heat input condition of 250 J mm^{-1} in Figure 4.4 (b). This could represent the initial stage of crack initiation by void formation and coalescence. The micro-cracks in block B could only be identified by SEM observation. Larger cracks in block C were observed, which were wide enough for identification with optical microscopy. The lengths of the longest cracks observed in blocks B and C were 0.6 mm and 0.8 mm, respectively. In comparison, the largest crack in blocks D and E was measured as 1.4 mm and 2.9 mm, respectively. A further increase in heat input resulted in large macro-cracks that were commonly observed in blocks D and E, as shown for the heat input conditions of 450 and 550 J mm^{-1} in Figure 4.4 (b).

The cracks observed in block E were wide enough to allow SEM observation of the crack flanks as shown in Figure 4.4 (c). At lower magnifications, the crack flank appears flat, the presence of rounded micro-voids (< 1 µm in diameter) is revealed at a higher magnification. This implies that there was limited ductility during failure of the material. In other words, a quasi-cleavage fracture mechanism prevailed at the grain boundaries during AW-DED of alloy 36 at heat inputs ranging from 250–550 J mm^{-1}, thereby resulting in intergranular cracking. The wavy morphology of the crack flank and the absence of dendritic features on the fracture surface suggest that cracking occurred in the solid state. Furthermore, enrichment of elements such as S and P, which are known to promote the formation of low melting point compounds, either interdendritic or intergranular, was not detected during chemical analysis of the crack flanks [36]. Therefore, the observed cracking phenomenon cannot be attributed to solidification cracking.

For further analysis, EBSD was used and image quality (IQ) maps of samples taken from blocks A and E are shown in Figures 4.5 (a) and (b), respectively. The highly non-tortuous character of the high-angle grain boundaries with a misorientation greater than 15 ° (white arrows) is noticeable in these maps. In Figure 4.5 (a), serrated boundaries are also observed that are identified as low-angle grain boundaries (black arrows) with misorientation between 5 ° and 15 °. The crack is identified to form along a high angle grain boundary (red arrow), as seen in the IQ map corresponding to block E, whereas the IQ map of the sample from block A is free of cracks.

During AM, repeated thermal cycling can induce non-uniform stresses and strains in the deposited material. A qualitative assessment of these strains can be realised through EBSD by plotting kernel average misorientation (KAM) maps [37, 38]. In Figures 4.5 (c) and (d), KAM maps are shown that correspond to the IQ maps of Figure 4.5 (a) and (b), respectively. The KAM values were calculated using the third nearest neighbour with a misorientation threshold of 5 °. High KAM values are associated with areas around the crack and the triple point (red circle in Figure 4.5 (d)) of the grains. This implies that the strain was localised at these locations rather than distributed throughout the material. The average KAM value calculated from both maps in Figures 4.5 (c) and (d) is similar, 0.59 ° and 0.54 °, respectively. The total

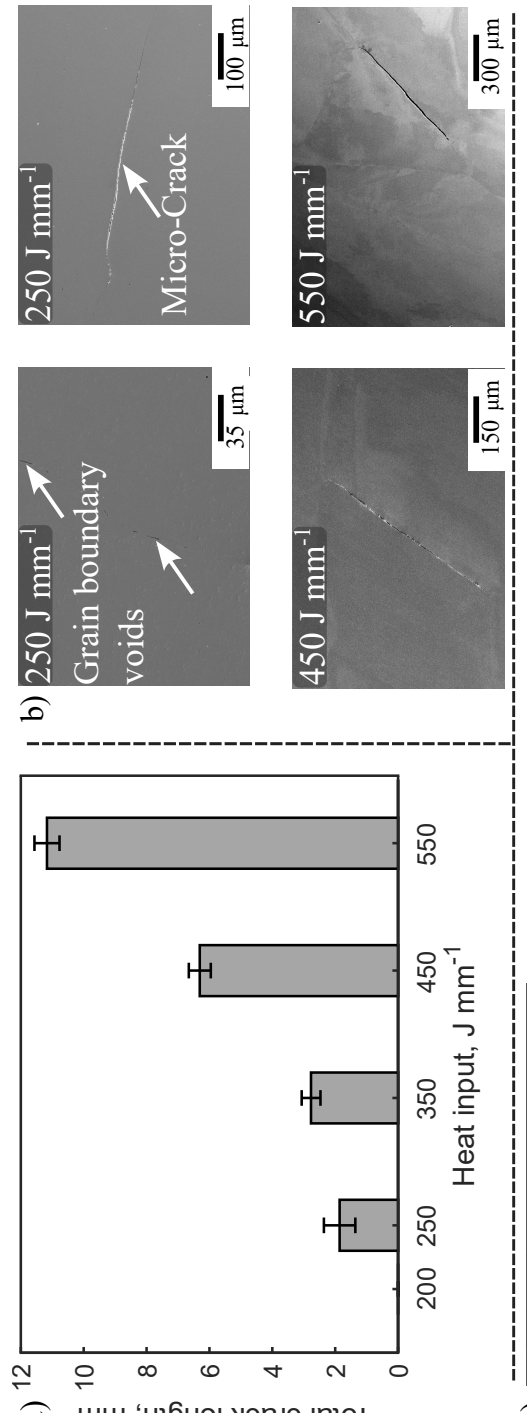

Figure 4.4: Experimentally derived variation of the total crack length per block versus the heat input in (a). Observation of intergranular voids and cracks corresponding to different heat input conditions in (b). Micrographs of a crack observed in block E, revealing a characteristic wavy appearance of the crack flank in (c). The total crack length per block was measured from 4 cross-sections taken parallel to the BD-TD plane in each block.

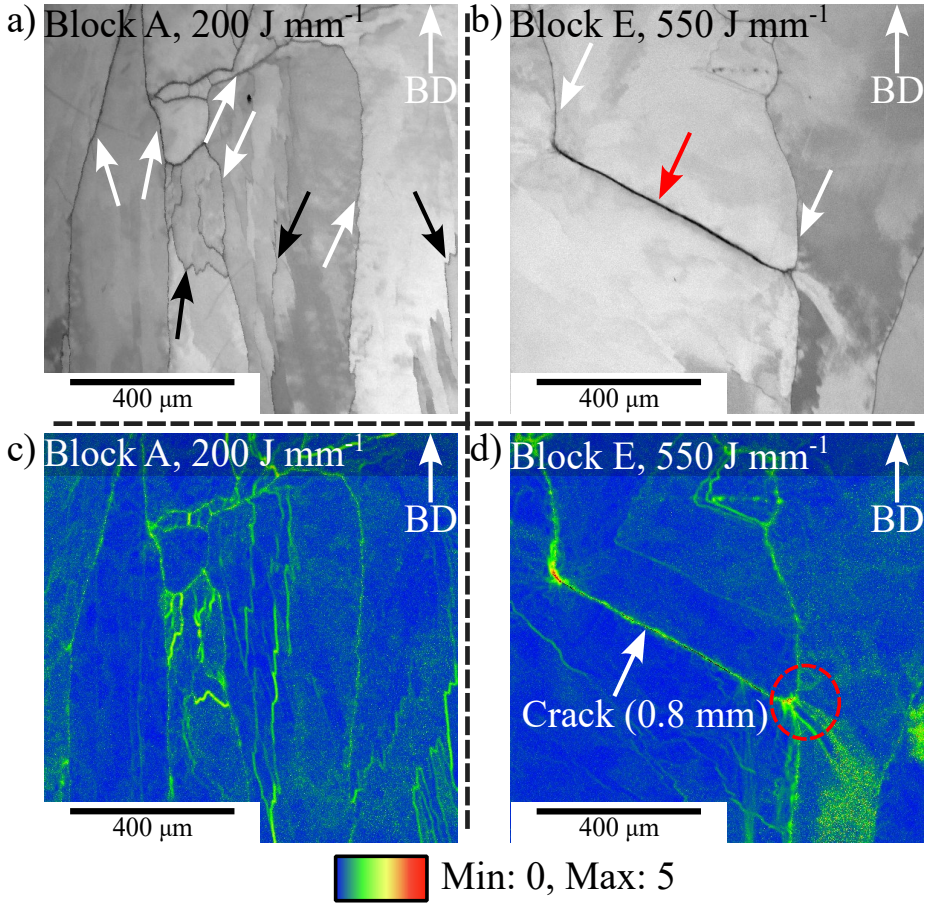

Figure 4.5: Image quality maps showing the grain boundary morphology in the microstructure of block A in (a), and a grain boundary crack in the microstructure of block E in (b). The KAM maps corresponding to the IQ maps of (a) and (b), are shown in (c) and (d), respectively.

length of high- and low-angle grain boundaries measured in Figure 4.5 (a) is 5.7 mm and 2.4 mm, respectively, while in Figure 4.5 (b) the lengths are 3.2 mm and 0.9 mm, respectively. The higher grain boundary area observed in the KAM map of block A effectively promotes the partitioning of the strain among several grain boundaries. Hence, the triple point and the associated grain boundaries in Figure 4.5 (b), must accommodate higher strains, compared to Figure 4.5 (a). A crack then forms if the built-up strain at the grain boundary exceeds the strength of that grain boundary. In summary, the KAM maps give evidence of strain in the as-deposited alloy 36. Although the two maps exhibit similar average KAM values, cracking is observed only in block E. This behaviour is attributed to the higher heat input applied during its deposition, which promotes grain coarsening and, in turn, increases the strain accommodated per

grain boundary. Consequently, alloy 36 becomes more prone to cracking as the heat input increases from 200 J mm^{-1} towards 550 J mm^{-1} during the GTAW-based AW-DED.

The results of this section, regarding cracking during AW-DED of alloy 36, can be explained by the phenomenon of ductility-dip cracking (DDC). This is a solid-state cracking phenomenon that occurs when the transient accumulation of stresses/strains can exhaust the limited ductility of a material at elevated temperatures [39]. A material specific temperature range is identified in which the ductility drops and is referred to as the ductility-dip range. Ductility-dip cracks are commonly reported in materials that display non-tortuous grain boundaries and are often associated with triple junctions of the grains [40]. Grain boundary sliding is one of the known mechanisms that leads to DDC [39–41]. In the studies pertaining to assess the weldability of alloy 36 and Ni-base alloys, DDC cracks have been reported to have a similar morphology to the results shown in this section [42, 43]. The role of grain boundary sliding in causing DDC was reported in a study investigating the phenomenon of reheat cracking in alloy 36 [44]. Additionally, it has been shown in a weldability assessment study of alloy 36 that lowering the heat input reduces the depth of the ductility-dip range of the alloy [45]. This implies that a higher level of stress/strain can be tolerated by the material before cracking occurs. Furthermore, a reduction in heat input during AW-DED of alloy 36 can facilitate a lowering of the extent of strain localisation at a grain boundary, thereby improving the resistance to cracking as shown earlier in this section. Lastly, grain boundary engineering can potentially mitigate DDC as this phenomenon is related to the morphology of the grain boundaries. In view of the chemical composition, the effect of impurity elements such as S and P is known to be deleterious with respect to DDC [5, 46]. These elements are also known to increase the susceptibility to solidification cracking in steels, since they promote the persistence of interdendritic liquid films towards the end of solidification. The alloy 36 wire used in this study had extremely low levels of S and P. Enrichment of these elements at the grain boundaries/crack flanks during AW-DED of alloy 36 was not observed during chemical analysis. Therefore, alloy 36 with relatively low levels of S and P can still experience DDC due to the transient build-up of stresses and strains during AW-DED, together with a microstructure that is inherently vulnerable to such cracking.

4.3.3. FUNCTIONAL PERFORMANCE OF AS-DEPOSITED ALLOY 36

The tensile properties of as-deposited alloy 36 in the case of the crack-free condition (block A1, 200 J mm^{-1}) and the high heat input DDC-susceptible condition (block E1, 550 J mm^{-1}), are shown in Figure 4.6. For the crack-free deposition condition, the observed mechanical properties are found to be in good agreement with the material properties specified by the alloy 36 wire manufacturer. The average yield strength is found to be slightly lower, 6.6% and 5.2% for the samples oriented in the building (vertical) and welding (horizontal) directions, respectively, than the material specification of 280 MPa. However, the average ultimate tensile strength and elongation of the tested samples exceeded the material specification of 350 MPa and 25%, respectively. No significant anisotropy was observed between the average tensile properties of the vertically and horizontally oriented samples. In the case of alloy 36 fabricated in the high heat input (550 J mm^{-1}) condition, the average tensile

properties were found to be well below the material supplier's specifications, as seen in Figure 4.6. This was due to the observation of premature failure in 6 out of 8 tested specimens. In 2 of the prematurely failed specimens, failure was observed before the onset of yielding, which led to a complete brittle failure. This premature failure was due to the opening of internal ductility-dip cracks during tensile loading.

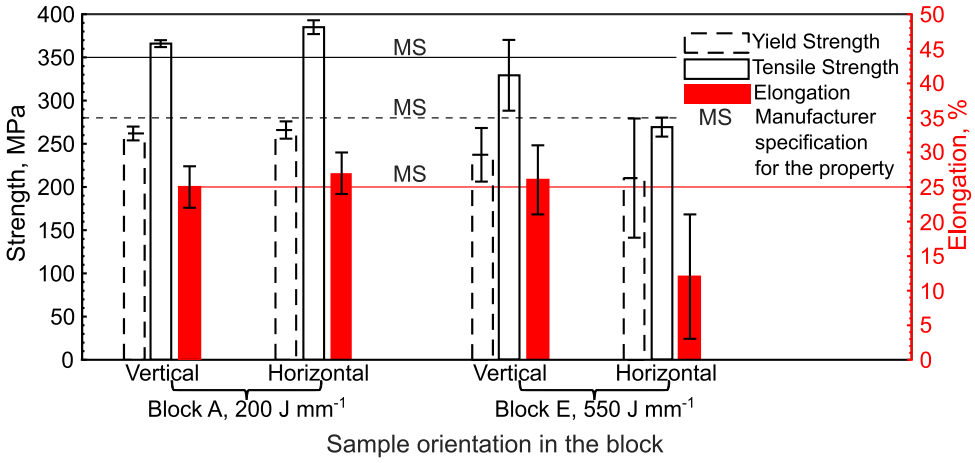

Figure 4.6: Tensile properties of the as-deposited alloy 36 in the extreme conditions of the heat input, i.e. 200 and 550 J mm^{-1}. Vertical and horizontal refers to samples oriented in the building and travel directions, respectively, and MS-lines indicate the manufacturer specification of the alloy 36 wire.

The fracture surfaces of two samples (one per direction) as observed in a SEM are shown in Figure 4.7. The presence of cleavage regions that are visible in the low-magnification figures of the fracture surface suggests that the failure was predominantly brittle. The arrows in the figures indicate internal cracks and linearly arranged voids on the fracture surface. The internal cracks (Figures 4.7 (a-0) and (b-0)) and the voids (Figure 4.7 (a-1)) are potential failure initiation sites, as the sample has failed in the vicinity of these defects. In addition, such defects can act as stress concentrators, thus increasing the likelihood of premature failure. These defects can be associated with the phenomenon of ductility-dip cracking that occurred during the deposition of alloy 36 in the high heat input condition of block E1. Consequently, due to the presence of ductility-dip cracks, an inherently ductile alloy at room temperature (alloy 36) can be prone to brittle failure in a tensile loading environment. Since the same alloy when deposited in the crack-free low heat input condition of block A1 (200 J mm^{-1}) displays a good mechanical response that is consistent with the material specifications of the feedstock wire.

The temperature-displacement curves of the as-deposited alloy 36 in heat input conditions corresponding to blocks A1 and E1 are shown in Figure 4.8. The displacement curves corresponding to different specimens are observed to be nearly identical, as seen in the figure.The thermal expansion exhibits an approximately linear dependence on temperature in the range from room temperature (RT) to

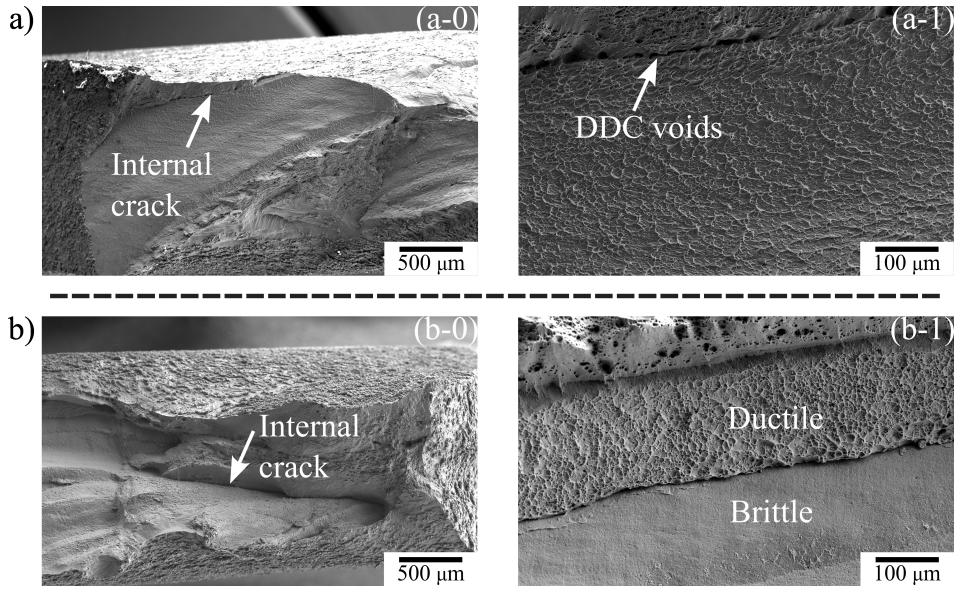

Figure 4.7: Fracture surfaces of the tensile samples oriented vertically and horizontally at different magnifications in (a) and (b), respectively.

127 °C, and again above 277 °C onwards. However, between 140 °C and 277 °C the variation is non-linear. In this temperature range, the magnetostrictive effect of alloy 36 diminishes and the thermal expansion due to lattice vibrations takes over. Therefore, resulting in a typical thermal expansion behaviour at temperatures above 300 °C, as seen in the displacement curves. The mean CTE of as-deposited alloy 36 corresponding to the curves shown in Figure 4.8, are listed in Table 4.2. The observed CTE values are on par with those reported for the conventionally processed alloy 36 [1, 2]. Therefore, AW-DED is a potential alternative to the conventional and powder-based processing of alloy 36.

The alloy deposited under both heat input conditions exhibits the lowest CTE in the temperature range between RT and 100 °C. This reflects the characteristic low thermal expansion behaviour of alloy 36. In general, the CTE of the vertically built samples is observed to be slightly higher than those of the horizontally built samples, regardless of heat input, as seen in Table 4.2. The disparity between the CTE of the vertical and horizontal samples cannot be attributed to differences in the grain morphology, as previously observed, or crystallographic texture. This is due to the dependence of the thermal expansion on the symmetry of the crystal, or in other words, the thermal expansion of a cubic system is isotropic regardless of the crystallographic direction [47]. However, under the influence of stress, thermal expansion can display anisotropic behaviour, as magnetovolume effects—which underpin the low thermal expansion anomaly in alloy 36—are strongly affected by stress [48]. It is well known that additively manufactured components can experience non-uniform complex residual stress states [49]. The presence of residual stresses

in alloy 36 produced by selective laser melting was shown by Yakout *et al.* [30]. The stress states of the deposited parts were not quantified in this study; however, it is reasonable to assume that the blocks will be subject to the development of residual stresses. These stresses can perturb the magnetic domain arrangement in the ferromagnetic alloy 36 by a combination of stress-induced irreversible domain-wall motion and reversible mechanisms such as domain wall-bowing and magnetisation rotation [50]. This, in turn, influences the magnetovolume effects, which in the case of alloy 36 are critical to its low CTE. The perturbations in the domain arrangement are partially retained in the material upon the removal of stress due to the irreversibility of the domain wall motion, potentially modifying the magnetovolume response. Hence, the difference in the CTE between the vertically and horizontally built samples is likely a result of the residual stress history experienced by the deposited blocks. This argument has been supported by the recent work of Huang *et al.* [51] in which they showed that the CTE of alloy 36 fabricated by laser powder bed fusion was entirely influenced by residual stresses, rather than factors such as grain morphology, grain boundary density, and crystallographic texture.

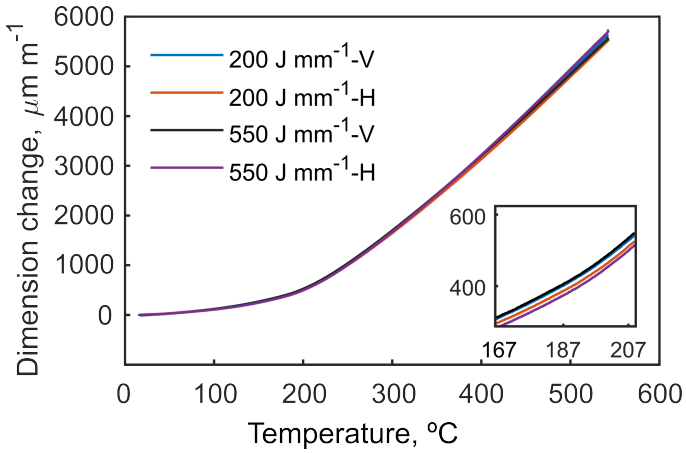

Figure 4.8: Temperature-displacement curves of the as-deposited alloy 36 in the extreme conditions of the heat input (200 J mm^{-1} and 550 J mm^{-1}). V (vertical) and H (horizontal) refers to samples oriented in the building and travel directions, respectively.

Intergranular cracking (DDC) was observed during the deposition of alloy 36 at a HI of 550 J mm^{-1}, whereas cracking was avoided when a HI of 200 J mm^{-1} was utilised to deposit alloy 36. The comparison of CTE values for these two HI conditions indicates that intergranular cracking negligibly affects the thermal dimensional performance of alloy 36. If intergranular cracking had a significant influence on CTE, a clear disparity would be identified in the CTE values of alloy 36 deposited in heat inputs of 200 and 550 J mm^{-1}. Specifically in the low temperature regime (below the Curie temperature) where the lattice thermal expansion is countered by the spontaneous volume magnetostriction. However, the density of cracks and the

width or size of the cracks could be important factors to consider when evaluating the effect of cracks on the thermal expansion of alloy 36. It is possible that the effect of cracks on thermal expansion becomes pronounced above a certain density of cracks. Similarly, the width/size of the cracks, or quantified by the aspect ratio of the cracks, may also influence the thermal expansion. These factors were not explicitly considered in this study and are recommended for future work. However, the dilatometry samples in the case of alloy 36 deposited at a HI of 550 J mm^{-1} were machined in the vicinity of locations where intergranular cracks were observed by metallographic observations. Therefore, purely form the viewpoint of using alloy 36 for its thermal expansion properties, the use of the high HI condition of 550 J mm^{-1} is justified. This will lead to intergranular cracking while facilitating a higher deposition rate compared to the low HI condition. However, in applications that impose tensile load on alloy 36 structures fabricated by AW-DED intergranular cracking cannot be tolerated, and it is essential to lower the HI. Naturally, a crack-free deposit with good expansion properties can then be obtained but at the cost of the deposition rate, which in turn could be offset by using a multi-machine deposition approach.

Table 4.2: The mean linear CTE of as-deposited alloy 36 in the lower and upper extreme conditions of the heat input range. The CTE values are in the unit of $\times 10^{-6}$ °C^{-1}, and the uncertainty in measurement: $\pm 0.01 \times 10^{-6}$ °C^{-1}.

Mean CTE	HI: 200 J mm^{-1}		HI: 550 J mm^{-1}	
Temperature range, °C	Vertical	Horizontal	Vertical	Horizontal
RT–100	1.40	1.39	1.48	1.27
RT–200	2.74	2.67	2.79	2.60
RT–300	5.85	5.73	5.92	5.81
RT–400	8.34	8.15	8.32	8.36

4.4. CONCLUSIONS

This chapter investigated the deposition of alloy 36 using a wire-based DED technique. The effect of heat input on cracking susceptibility, tensile behaviour, and thermal expansion of alloy 36 was explored. Based on the results presented in this chapter, the following conclusions can be drawn:

1. Cold wire GTAW-based AW-DED can be employed to fabricate the low thermal expansion alloy 36 without the presence of lack of fusion defects. In this regard, the use of a suitable range for the wetting angle of the weld beads is critical during overlapping to avoid these defects.

2. The microstructure of the as-deposited alloy 36 is mainly composed of columnar grains with non-tortuous grain boundaries. Additionally, due to the single-phase nature of alloy 36, it is prone to grain coarsening during AW-DED, which renders the alloy as susceptible to DDC.

3. The macroscopic Ni content in the as-deposited alloy 36 is maintained at 36 wt.%, and the alloy remains entirely austenitic under various heat input conditions.

4. The susceptibility of alloy 36 to DDC decreases with a reduction in heat input. This behaviour is attributed to the larger grain boundary area available at lower heat input, which facilitates a more uniform distribution of the accumulated strain.

5. Avoiding cracking is necessary for structural applications of alloy 36 as the presence of intergranular cracks can lead to premature failure. However, the mechanical properties of as-deposited alloy 36 in the crack-free condition meet the specifications of the material supplier.

6. The mean linear CTE values of the as-deposited alloy 36 in low (defect-free) and high (susceptible to DDC) heat input conditions are comparable to those displayed by the conventionally processed alloy.

REFERENCES

[1] *Low-expansion alloys*. Metals Handbook Desk Edition. ASM International, 1998, pp. 665–667. DOI: 10.31399/asm.hb.mhde2.a0003159.

[2] E. L. Frantz. *Low-expansion alloys*. Properties and Selection: Nonferrous Alloys and Special-Purpose Materials. Vol. 2. ASM International, 1990, pp. 889–896. DOI: 10.31399/asm.hb.v02.a0001099.

[3] *Stainless steel 1.4404 material data sheet*. thyssenkrupp Materials (UK) Ltd. Accessed: Mar. 04, 2025. Available: https://www.thyssenkrupp-materials.co.uk/stainless-steel-316l-14404.html. 2025.

[4] J. L. Corbacho, J. C. Suérez, and F. Molleda. *Welding of Invar Fe-36Ni alloy for tooling of composite materials*. Welding International 12, 12 (1998), pp. 966–971. DOI: 10.1080/09507119809448543.

[5] T. Ogawa, H. Sakurai, and T. Koseki. *Weldability of Invar and its large-diameter pipe*. Welding Journal 65, 8 (1986), pp. 213–226.

[6] S. Yamamoto, T. Edamitsu, M. Ujita, S. Kishimoto, N. Takeuchi, K. Nakamura, and K. Yamamoto. *Realization of Invar alloy LNG piping*. Accessesd: Mar. 12, 2025. Available: http://members.igu.org/html/wgc2003/WGC_pdffiles/10325_1045211427_4649_1.pdf. 2003.

[7] M. Yakout, A. Cadamuro, M. A. Elbestawi, and S. C. Veldhuis. *The selection of process parameters in additive manufacturing for aerospace alloys*. International Journal of Advanced Manufacturing Technology 92, 5–8 (2017), pp. 2081–2098. DOI: 10.1007/s00170-017-0280-7.

[8] M. Yakout, M. A. Elbestawi, and S. C. Veldhuis. *A study of thermal expansion coefficients and microstructure during selective laser melting of Invar 36 and stainless steel 316L*. Additive Manufacturing 24 (2018), pp. 405–418. DOI: 10.1016/j.addma.2018.09.035.

[9] J. Allen. *An investigation into the comparative costs of additive manufacture vs. machine from solid for aero engine parts*. STO Meeting Proceedings. 2006, 17:1–17:10. DOI: 10.14339/RTO-MP-AVT-139-17-pdf.

[10] S. W. Williams, F. Martina, A. C. Addison, J. Ding, G. Pardal, and P. Colegrove. *Wire + arc additive manufacturing*. Materials Science and Technology 32, 7 (2016), pp. 641–647. DOI: 10.1179/1743284715Y.0000000073.

[11] S. H. Huang, P. Liu, A. Mokasdar, and L. Hou. *Additive manufacturing and its societal impact: A literature review*. International Journal of Advanced Manufacturing Technology 67, 5–8 (2013), pp. 1191–1203. DOI: 10.1007/s00170-012-4558-5.

[12] C. Qiu, N. J. E. Adkins, and M. M. Attallah. *Selective laser melting of Invar 36: Microstructure and properties*. Acta Materialia 103 (2016), pp. 382–395. DOI: 10.1016/j.actamat.2015.10.020.

[13] H. Asgari, M. Salarian, H. Ma, A. Olubamiji, and M. Vlasea. *On thermal expansion behavior of invar alloy fabricated by modulated laser powder bed fusion*. Materials and Design 160 (2018), pp. 895–905. DOI: 10.1016/j.matdes.2018.10.025.

[14] Q. Yang, K. Wei, X. Yang, H. Xie, Z. Qu, and D. Fang. *Microstructures and unique low thermal expansion of Invar 36 alloy fabricated by selective laser melting*. Materials Characterization 166.110409 (2020). DOI: 10.1016/j.matchar.2020.110409.

[15] N. Khanna, S. Mistry, R. A. Rahman Rashid, and M. K. Gupta. *Investigations on density and surface roughness characteristics during selective laser sintering of Invar-36 alloy*. Materials Research Express 6,8, no.086541 (2019). DOI: 10.1088/2053-1591/ab18bd.

[16] H. Tan, Y. Wang, G. Wang, F. Zhang, W. Fan, Z. Feng, and X. Lin. *Investigation on microstructure and properties of laser solid formed low expansion Invar 36 alloy*. Journal of Materials Research and Technology 9, 3 (2020), pp. 5827–5839. DOI: 10.1016/j.jmrt.2020.03.108.

[17] N. J. Harrison, I. Todd, and K. Mumtaz. *Thermal expansion coefficients in Invar processed by selective laser melting*. Journal of Materials Science 52, 17 (2017), pp. 10517–10525. DOI: 10.1007/s10853-017-1169-4.

[18] F. Veiga, A. Suárez, T. Artaza, and E. Aldalur. *Effect of the heat input on wire-arc additive manufacturing of Invar 36 alloy: Microstructure and mechanical properties*. Welding in the World 66, 6 (2022), pp. 1081–1091. DOI: 10.1007/s40194-022-01295-4.

[19] E. Aldalur, A. Suárez, and F. Veiga. *Thermal expansion behaviour of Invar 36 alloy parts fabricated by wire-arc additive manufacturing*. Journal of Materials Research and Technology 19 (2022), pp. 3634–3645. DOI: 10.1016/j.jmrt.2022.06.114.

[20] J. Fowler, A. Nycz, M. Noakes, C. Masuo, and D. Vaughan. *Wire-arc additive manufacturing: Invar deposition characterization*. Proceedings of the 30th Annual International Solid Freeform Fabrication Symposium. 2019, pp. 616–624. DOI: 10.26153/tsw/17299.

[21] J. L. Corbacho, J. C. Suárez, and F. Molleda. *Grain coarsening and boundary migration during welding of Invar Fe-36Ni alloy*. Materials Characterization 41, 1 (1998), pp. 27–34. DOI: 10.1016/S1044-5803(98)00020-5.

[22] F. Li, W. Guo, B. Lin, B. Qi, L. Chen, W. Yu, and Y. Zhu. *Interfacial microstructure and mechanical properties of Fe-36Ni Invar alloy GTAW joint*. Indian Journal of Engineering & Materials Sciences 24 (2017), pp. 290–294.

[23] H. Nakagawa, F. Matsuda, A. Nagai, and N. Sakabata. *Weldability of Fe-36%Ni alloy (report I) : Hot cracking with cross-bead test (materials, metallurgy, weldability)*. Transactions of JWRI 9, 2 (1980), pp. 197–204.

[24] *Invar M93 pipes and tubes for LNG transfer lines*. ArcelorMittal. Accessed: Mar. 12, 2025. Available: https://www.spacematdb.com/spacemat/manudatasheets/Invar%20M93.pdf. 2008.

[25] S. Kou. *Heat flow in welding*. Welding Metallurgy. 3rd ed. John Wiley & Sons, 2021. Chap. 2, pp. 37–60.

[26] K. Wei, Q. Yang, B. Ling, X. Yang, H. Xie, Z. Qu, and D. Fang. *Mechanical properties of Invar 36 alloy additively manufactured by selective laser melting*. Materials Science and Engineering: A 772.138799 (2020). DOI: 10.1016/j.msea.2019.138799.

[27] G. Jiao, X. Fang, M. Zhang, Z. Li, R. Cai, H. Wu, and K. Huang. *Synergistic improvement of mechanical property and thermal expansion of wire-arc DED Invar alloy enabled by a novel deposition strategy*. Journal of Manufacturing Processes 121 (2024), pp. 121–135. DOI: 10.1016/j.jmapro.2024.05.031.

[28] *Standard test methods for determining average grain size*. ASTM Standard E112-13, 2021.

[29] I. V. Vernyhora, V. A. Tatarenko, and S. M. Bokoch. *Thermodynamics of f.c.c.-Ni–Fe alloys in a static applied magnetic field*. ISRN Thermodynamics 2012, no. 917836 (2012). DOI: 10.5402/2012/917836.

[30] M. Yakout, M. A. Elbestawi, S. C. Veldhuis, and S. Nangle-Smith. *Influence of thermal properties on residual stresses in SLM of aerospace alloys*. Rapid Prototyping Journal 26, 1 (2020), pp. 213–222. DOI: 10.1108/RPJ-03-2019-0065.

[31] D. Jafari, T. H. Vaneker, and I. Gibson. *Wire and arc additive manufacturing: Opportunities and challenges to control the quality and accuracy of manufactured parts*. Materials and Design 202, no. 109471 (2021). DOI: 10.1016/j.matdes.2021.109471.

[32] N. A. Rosli, M. R. Alkahari, M. F. b. Abdollah, S. Maidin, F. R. Ramli, and S. G. Herawan. *Review on effect of heat input for wire arc additive manufacturing process*. Journal of Materials Research and Technology 11 (2021), pp. 2127–2145. DOI: 10.1016/j.jmrt.2021.02.002.

[33] L. McKeehan. *The crystal structure of iron-nickel alloys*. Physical Review 21 (1923), pp. 402–407. DOI: 10.1103/PhysRev.21.402.

[34] W. A. Tiller. *Preferred growth direction of metals*. Journal of Metals 9 (1957), pp. 847–855. DOI: 10.1007/BF03397928.

[35] W. Kurz and D. J. Fisher. *Introduction*. Fundamentals Of Solidification. Trans Tech Publications Ltd., 1984. Chap. 1, pp. 1–14.

[36] G. Agarwal, A. Kumar, I. M. Richardson, and M. J. M. Hermans. *Evaluation of solidification cracking susceptibility during laser welding in advanced high strength automotive steels*. Materials & Design 183, no. 108104 (2019). DOI: 10.1016/j.matdes.2019.108104.

[37] X. Min, S. Emura, X. Chen, X. Zhou, K. Tsuzaki, and K. Tsuchiya. *Deformation microstructural evolution and strain hardening of differently oriented grains in twinning-induced plasticity β titanium alloy*. Materials Science and Engineering: A 659 (2016), pp. 1–11. DOI: 10.1016/j.msea.2016.01.105.

[38] X. Zhang, H. Chen, L. Xu, J. Xu, X. Ren, and X. Chen. *Cracking mechanism and susceptibility of laser melting deposited Inconel 738 superalloy*. Materials and Design 183, no. 108105 (2019). DOI: 10.1016/j.matdes.2019.108105.

[39] J. C. Lippold. *Solid-state cracking*. Welding Metallurgy and Weldability. Hoboken: John Wiley & Sons, Inc., 2015. Chap. 4, pp. 130–213.

[40] S. Kou. *Ductility dip cracking*. Welding Metallurgy. 3rd ed. John Wiley & Sons, 2021. Chap. 14, pp. 379–397.

[41] J. N. DuPont, J. C. Lippold, and S. D. Kiser. *Solid-solution strengthened Ni-base alloys*. Welding Metallurgy and Weldability of Nickel-Base Alloys. John Wiley & Sons, 2011. Chap. 3, pp. 47–156.

[42] Y.-C. Zhang, H. Nakagawa, and F. Matsuda. *Weldability of Fe-36%Ni alloy (report VI): Further investigation on mechanism of reheat hot cracking in weld metal (materials, metallurgy & weldability)*. Transactions of JWRI 14, 2 (1985), pp. 325–334.

[43] M. G. Collins, A. Ramirez, and J. C. Lippold. *An investigation of ductility dip cracking in nickel-based weld metals - part II*. Welding Journal 82 (2003), pp. 348–354.

[44] Y.-C. Zhang, H. Nakagawa, and F. Matsuda. *Weldability of Fe-36%Ni alloy (report V): Behaviors of grain-boundary sliding and cavity formation preceding reheat hot cracking in weld metal (materials, metallurgy & weldability)*. Transactions of JWRI 14, 2 (1985), pp. 319–324.

[45] Y.-C. Zhang, H. Nakagawa, and F. Matsuda. *Weldability of Fe-36%Ni alloy (report III) : Dynamic observation of reheat hot crack and evaluation of hot ductility of reheated weld metal (materials, metallurgy & weldability)*. Transactions of JWRI 14, 1 (1985), pp. 107–117.

[46] F. Matsuda, H. Nakagawa, S. Minehisa, N. Sakabata, A. Ejima, and K. Nohara. *Weldability of Fe-36% Ni alloy (report II): Effect of chemical composition on reheated hot cracking in weld metal (materials, metallurgy & weldability)*. Transactions of JWRI 13, 2 (1984), pp. 241–247.

[47] *Effect of cold working and recrystallization of Invar alloys*. Physics and Application of Invar Alloys: Honda Memorial Series on Materials Science No. 3. Ed. by H. Saito. Tokyo: Maruzen Company LTD, 1978. Chap. 20, pp. 474–493.

[48] B. D. Cullity and C. D. Graham. *Magnetostriction and the effects of stress*. Introduction to Magnetic Materials. 2nd ed. Hoboken: John Wiley & Sons, Inc., 2009, pp. 241–275. DOI: 10.1002/9780470386323.

[49] K. Carpenter and A. Tabei. *On residual stress development, prevention, and compensation in metal additive manufacturing*. Materials 13, 255 (2020). DOI: 10.3390/ma13020255.

[50] L. Kraus and P. Švec. *Magnetoelastic hysteresis of amorphous ribbons*. Journal of Applied Physics 93, 10 (2003), pp. 7220–7222. DOI: 10.1063/1.1540043.

[51] G. Huang, G. He, Y. Liu, and K. Huang. *Anisotropy of microstructure, mechanical properties and thermal expansion in Invar 36 alloy fabricated via laser powder bed fusion*. Additive Manufacturing 82, no. 104025 (2024). DOI: 10.1016/j.addma.2024.104025.

5

DEPOSITION OF LOW THERMAL EXPANSION ALLOYS BY TWIN-WIRE FEEDING[¶]

THE feasibility of obtaining on-demand low thermal expansion (LTE) alloy compositions based on the Fe–Ni system was demonstrated. A twin-wire feeding approach was adapted to allow in situ deposition of alloys 42, 46, and 52 by simultaneously feeding alloy 36 and Ni wires into a melt pool. Two distinct modes of liquid metal transfer to the melt pool were observed: intermittent and continuous metal transfer, as revealed by melt pool imaging. In contrast to the intermittent metal transfer mode, the continuous metal transfer mode resulted in better compositional and dimensional stability of the beads during the twin-wire feeding approach. The Curie temperatures of the as-deposited in situ LTE alloys were comparable to those of the conventional LTE alloys. The mean linear coefficient of thermal expansion of alloy 46 evaluated in various temperature ranges was on par with its commercial counterpart. Hence, the twin-wire feeding approach allowed the successful generation of on-demand thermal expansion properties.

5.1. INTRODUCTION

The Fe–Ni alloys with low thermal expansion (LTE), characterised by low linear coefficients of thermal expansion (CTE), are used in applications where the geometry of the components must remain stable in response to imposed thermal loads [1–3]. During heating and cooling, the volume change due to spontaneous magnetostriction counteracts the dimensional change arising from lattice vibrations in LTE Fe–Ni alloys, resulting in low CTE values [4, 5]. Alloy 36 contains 36 wt.% Ni and displays the

[¶]The contents of this chapter are in part based on a journal article published as: A. Sood, J. Schimmel, M. Bosman, C. Goulas, V. Popovich, and M. J. M. Hermans. *Fabrication of low thermal expansion Fe–Ni alloys by in-situ alloying using twin-wire arc additive manufacturing.* Materials & Design 240, no. 112837 (2024).

lowest CTE between room temperature (RT) and 150 °C, approximately 2.1 µm m^{-1} °C^{-1}, among the LTE alloys nominally composed of Fe and Ni [3]. In comparison, alloy 46, which comprises 46 wt.% Ni, exhibits a lower CTE than alloy 36 in a larger temperature range of RT–400 °C [6].

The CTE of the two alloys in different temperature ranges are compared in Table 5.1. For temperatures above 300 °C, alloy 46 offers a lower CTE than alloy 36. This dependence of thermal expansion on the Ni content in the Fe–Ni system can be exploited for site-specific or desired thermal expansion properties. In addition, LTE Fe–Ni alloy products are traditionally fabricated using machining processes [7]. Due to the single-phase austenitic microstructure of these alloys, machining becomes cumbersome as the alloys tend to adhere to the surface of the tool, severely degrading the tool life [8]. As a result, subtractive manufacturing of LTE alloys is generally associated with long lead times and high costs. Therefore, the utilisation of additive manufacturing (AM) processes, especially arc wire-DED, is justified for efficient processing of LTE Fe–Ni alloys. Moreover, a unique advantage of utilising AW-DED over subtractive manufacturing is the possibility of functionally grading a structure, which then offers site-specific material properties [9]. This can be achieved by controlling the material composition, for example, by combining different alloys, or by tailoring the microstructure, such as via optimisation of the crystallographic texture [10].

Table 5.1: Mean linear CTE of commercially available LTE alloys in different temperature ranges [3, 6].

Mean CTE, µm m^{-1} °C^{-1}	Temperature range	
	30–300 °C	30–400 °C
Alloy 36	6.10	8.70
Alloy 46	7.50	7.50

In the case of LTE Fe–Ni alloys, functional grading may be achieved by altering the amount of Ni, or by combining alloy 36 with a high-thermal expansion alloy that offers greater strength. For the latter, Bobbio *et al.* [11, 12] used DED-laser powder deposition to generate functionally graded materials (FGM), with the aim of creating a unique blend of thermal dimensional stability and strength by combining V and Ti-6Al-4V to alloy 36 in two different studies. In both studies, the as-deposited FGMs were observed to be susceptible to cracking due to the formation of detrimental intermetallic phases in the gradient region. However, the authors were successful in computationally predicting the experimentally observed phases in the gradient regions. In another study, Hofmann *et al.* [13] created a radial gradient from stainless steel 304L (AISI 304L) to alloy 36 using DED-laser powder deposition. Despite the mismatch in the CTE of the two alloys, a crack-free FGM of AISI 304L/Invar 36 was successfully deposited, thus achieving an FGM with ferromagnetic and paramagnetic properties at RT. Furthermore, in situ alloying can be used during AW-DED to deposit desired alloy compositions. This involves the simultaneous feeding of two metal wires to a melt pool to create 3D structures. Twin-wire feeding AW-DED processing

can facilitate the on-demand generation of LTE alloy compositions by combining elemental Fe and Ni wires, or alloy 36 with a Ni wire. However, the literature related to the in situ fabrication of LTE Fe–Ni alloys using a twin-wire feeding approach is lacking, in contrast to the studies available on the deposition of alloy 36 FGMs using powder-based DED. Hence, in this chapter, the deposition of multiple Fe–Ni LTE alloys is considered. A twin-wire feeding approach is employed in the cold wire pulsed current gas tungsten arc welding (GTAW) process to enable in situ alloying. A graded wall comprising distinct segments of 42, 46, and 52 wt.% Ni in the building direction, and a mono-material block containing 46 wt.% Ni are deposited. This is achieved by varying the wire feed speeds of two wires: 36 wt.% Ni (alloy 36 wire) and a wire with approximately 96 wt.% Ni. The microstructure of the as-deposited alloys is characterised by optical microscopy and X-ray diffraction (XRD). The stability of the process in the twin-wire approach is established through melt pool imaging, and the as-deposited compositions are quantified using energy-dispersive spectroscopy (EDS). Lastly, dilatometry is used to establish the Curie transitions of the Ni compositions in the graded wall, and to quantify the mean CTE of alloy 46 from the as-deposited mono-material block. In summary, the conditions promoting a stable melt pool during the twin-wire feed process and chemical mixing, along with the resulting functional properties of in situ fabricated LTE alloys, are systematically addressed in this study. Consequently, the present work establishes the feasibility of utilising the twin-wire feed process for the on-demand generation of LTE alloys.

5.2. EXPERIMENTAL OVERVIEW

A Migatronic TIG COMMANDER AC/DC 400 power source and two independent wire feeders were used during the twin-wire feed deposition experiments. The twin-wire feeding AW-DED process is schematically described in Figure 5.1, showing the wire feeding arrangement during the experiments. The alloy 36 wire was always fed towards the centre of the melt pool antiparallel to the WD, whereas the Ni wire was fed towards the edge of the melt pool, as seen in Figure 5.1. A functionally graded two-bead thick wall and a mono-material block were deposited with the twin-wire feed approach (Figure 5.1) . The number of layers in the graded wall and the mono-material block were approximately 20 and 8, respectively. The consumables used during the experiments were solid metal wires of 1.2 mm diameter manufactured by voestalpine Böhler Welding. The wires are commercially known as 3Dprint AM Mold 36, alloy 36 wire, and UTP A 80 Ni, approximately 96 wt.% Ni wire. The chemical compositions of these wires are listed in Table 3.1 (section 3.1).

Table 5.2: Wire feed speeds of alloy 36 and Ni wires utilised in this study to obtain three distinct LTE alloy compositions.

Wire feed speed, mm s^{-1}	Alloy 42	Alloy 46	Alloy 52
Alloy 36 wire	23.40	21.70	19.10
Ni wire	2.60	4.30	6.90

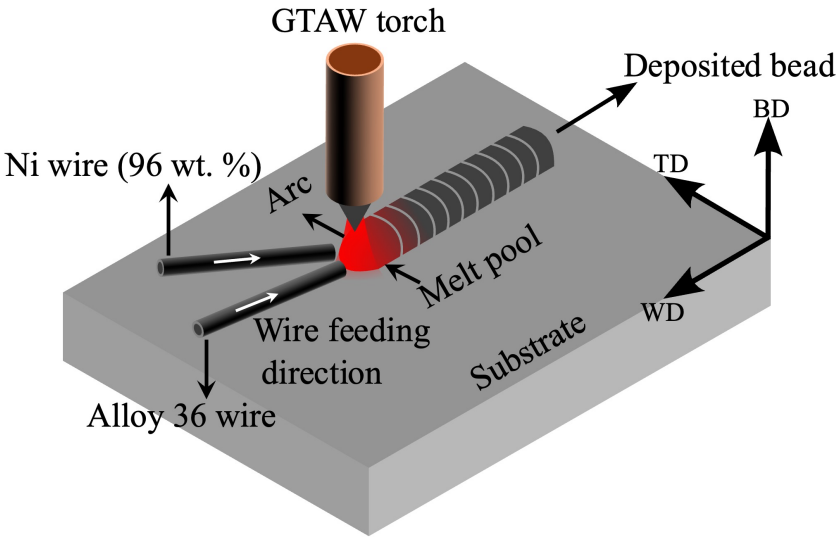

Figure 5.1: Schematic representation of the twin-wire feeding approach coupled with the GTAW process employed in this chapter.

The heat input (HI) setting during the twin-wire feeding experiments was adapted from the low HI condition reported in chapter 4, as it resulted in crack-free deposition of alloy 36. The wire feed speeds (WFS) were adjusted to achieve three distinct LTE alloy compositions with Ni amounts of 42, 46, and 52 wt.% through the twin-wire feed approach, as listed in Table 5.2. In the functionally graded wall, 5 layers of each alloy composition were deposited using the twin-wire feed approach, following the deposition of 4 layers of alloy 36 with single wire feeding. In contrast, the mono-material alloy 46 block was fabricated by depositing 2 layers of alloy 36 by single wire feeding and 6 subsequent layers using twin-wire feeding. The inter-pass temperature was limited to 120 °C during the experiments and monitored using a K-type thermocouple [14]. A Cavitar C300 welding camera was used to observe the melt pool during the experiments. The microstructural characteristics and chemical composition of the graded wall were analysed by SEM-EDS. Areas of $1.4 \times 1.3\,mm^2$ corresponding to the regions of alloy segments 42, 46, and 52 in the graded wall were mapped using EBSD with a step size of 0.8 µm. The beam current and acceleration voltage during the EBSD measurements were 3.2 nA and 20 kV, respectively. The Curie temperatures of the in situ deposited alloys 42, 46, and 52 in the graded wall were measured using an induction-heated dilatometer, via the energy jump method described in section 3.5 (chapter 3). The mean linear CTE of alloy 46 in various temperature ranges was established by extracting specimens from the mono-material block. The temperature-displacement curves corresponding to alloy 46 were experimentally determined using a dilatometer relying on furnace-based heating. The details of the characterisation techniques, such as optical microscopy, SEM-EDS, EBSD, dilatometry, and the corresponding sample preparation, are given in chapter 3.

5.3. RESULTS AND DISCUSSION

5.3.1. LIQUID METAL TRANSFER MODES DURING TWIN-WIRE FEEDING

Bead-on-plate experiments were performed to optimise the deposition during the twin-wire feed process. The overview of two beads obtained from these experiments is shown in Figure 5.2. The ratio of the wire feed speeds of the two wires was adjusted to achieve the composition of alloy 42 as this would be the first composition in the graded wall to be obtained by the twin-wire approach. The dimensional characteristics of the beads are listed in Table 5.3. From the table, it can be seen that bead 2 demonstrated the highest stability, as reflected by the lowest deviation in height, width, and wetting angle of the bead. Consequently, bead 2 is considered optimum for depositing 3D structures.

The stable deposition condition of bead 2 is primarily attributed to a reduction in the distance between the tip of the Ni wire and the substrate relative to the distance maintained in the case of bead 1. This implies that the positioning of the Ni wire has a pronounced effect on the melt pool behaviour during the twin-wire feeding approach. Hence, the melt pool behaviour in the context of Ni wire feeding is explored as follows.

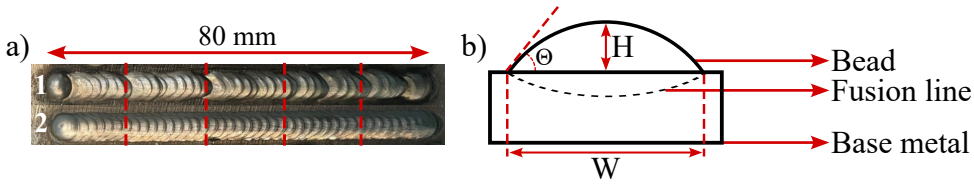

Figure 5.2: Beads obtained from the bead-on-plate experiments utilising the twin wire feeding approach in (a), bead 1 is deposited in the intermittent metal transfer mode and bead 2 in the continuous metal transfer mode. Schematic of the measured bead dimensions in (b), where w- width, h- height and Θ- wetting angle. The red dashed lines in (a), show the locations where the cross-sections were taken.

Table 5.3: Dimensional characteristics and the Ni content of the bead-on-plate welds shown in Figure 5.2. IT and CT refer to intermittent and continuous transfer modes, respectively.

Bead number	Height, mm	Width, mm	Wetting angle, °	Ni content, wt.%
1-IT	2.0 ± 1.3	4.7 ± 1.6	44 ± 9.3	43.4 ± 3.6
2-CT	1.5 ± 0.3	5.4 ± 0.5	38 ± 3.2	42.3 ± 1.1

Melt pool imaging was performed to understand the melt pool behaviour during the bead-on-plate experiments. This technique revealed two distinct modes of molten metal transfer during the twin wire feed process: intermittent metal transfer and continuous melting transfer, as shown in Figures 5.3 (a) and (b), respectively. The intermittent metal transfer mode occurred during the deposition of bead 1. This mode is characterised by interrupted liquid metal flow to the melt pool. A liquid metal

droplet forms at the tip of the wire and grows in size with time. This droplet can enter the melt pool in two ways: by bridging to the melt pool, or via free flight transfer from the wire to the melt pool. The droplet remains attached to the wire due to the surface tension and detaches as it encounters the melt pool, resulting in bridging transfer. Alternatively, the droplet can be released from the tip of the wire when the surface tension can no longer compensate for the downward forces due to its weight, arc pressure, and plasma drag, which results in free flight entry to the melt pool.

In intermittent metal transfer mode, a droplet entering the melt pool can cause instabilities in the melt pool, as shown in Figure 5.3 (a). In this figure, droplet detachment induces melt pool instabilities through oscillations of the liquid metal, leading to abrupt spatial variations in bead geometry. In contrast, during continuous metal transfer, droplets do not form at the wire tip; a stable liquid bridge persists throughout deposition, enabling smooth transfer of molten metal to the melt pool, as shown in Figure 5.3 (b). This allows for a stable deposition condition with the twin-wire approach, in contrast to the instabilities that can occur during the intermittent metal transfer mode, thereby resulting in geometrically varying weld beads.

The transition from intermittent to continuous metal transfer can be effectively managed through the strategic positioning of the wire relative to the substrate, as schematically illustrated in Figure 5.3 (c). Intermittent metal transfer mode occurs when the wire is fed to the melt pool at an increased height from the substrate, x_1, as depicted in Figure 5.3 (c-0), whereas a lower height, x_2, facilitates the continuous metal transfer mode, as shown in Figure 5.3 (c-1). Reducing the distance between the wire tip and the substrate allows the wire to contact the melt pool sooner, thus minimising the duration the wire tip spends within the arc column. Conversely, increasing this distance prevents the wire tip from making early contact with the melt pool, forcing a longer residence time within the arc column and resulting in droplet formation as the wire is fed. The growing droplet may then enter the melt pool upon contact (bridging transfer), or by detaching from the wire tip (free flight transfer). Therefore, precise wire positioning is essential to achieve stable deposition during the GTAW-based twin-wire feed process.

In addition to geometric stability, the continuous transfer of Ni to the melt pool in the case depicted in Figure 5.3 (b) is effective in achieving compositional homogeneity compared to the interrupted transfer shown in Figure 5.3 (a). This is reflected in the stable Ni content quantified in bead 2 compared to that of bead 1, as listed in Table 5.3. A melt pool during arc welding and, in turn, AW-DED is characterised by molten metal flow arising from the interaction of various forces—Marangoni, buoyancy, electromagnetic, and plasma shear—in combination with the material properties [15]. Naturally, during twin-wire feed-based AW-DED, the chemical mixing within the melt pool will be primarily governed by the chemical compatibility of the two wires used and the fluid flow in the melt pool. By maintaining the Ni wire in the condition depicted in Figure 5.3 (b), i.e. continuous metal transfer, the fluid flow within the melt pool remains stable, in contrast to the sudden perturbations caused by droplet entry into the melt pool, as observed in Figure 5.3 (a). Hence, the continuous metal transfer mode offers the compositional and geometrical stability required to

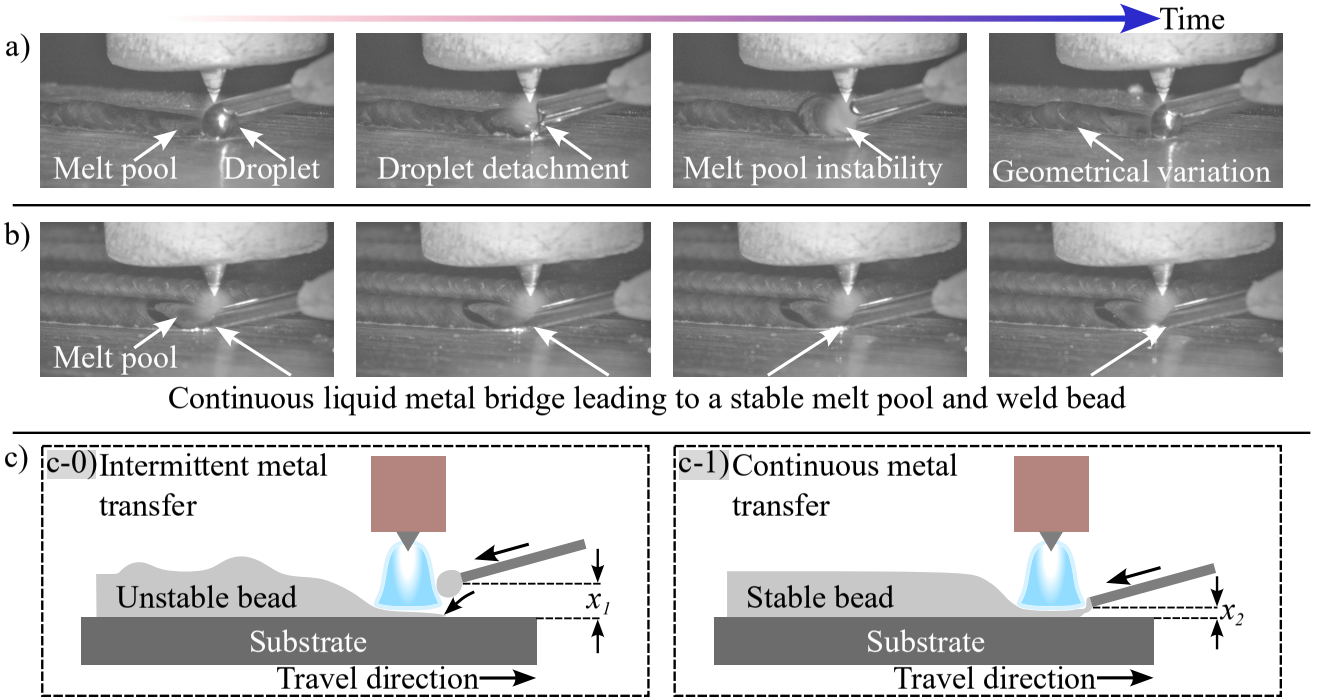

Figure 5.3: Intermittent and continuous liquid metal transfer modes during GTAW-based twin-wire feed processing, shown in (a) and (b), respectively. Schematic illustration of the two modes highlighting the impact of the wire placement in (c).

fabricate multi-bead structures using the twin-wire approach for in situ alloying. These multi-bead structures are presented and discussed in the following sections.

5.3.2. MICROSTRUCTURE AND CHEMICAL ANALYSES OF THE LOW THERMAL EXPANSION ALLOYS

The microstructures in the graded wall, corresponding to the regions comprising alloys 42, 46, and 52, are shown in Figures 5.4 (a), (b), and (c), respectively. Additionally, the microstructure of the mono-material alloy 46 block is shown in Figure 5.4 (d). The cross-sections of the wall and the block did not show lack of fusion defects nor intergranular cracks. This is achieved due to the high stability of the weld beads in the continuous metal transfer mode and the low heat input condition (based on chapter 4), utilised during the deposition of the structures, respectively.

The microstructure of both structures mainly consists of columnar grains that extend across multiple layers, as seen in Figure 5.4. Epitaxial growth of columnar grains is observed between layers, and the microstructure does not change with increasing amount of Ni as the grain morphology is similar for the three alloy compositions in the graded wall. This can be attributed to the formation of the single-phase austenitic solid-solution in the binary Fe–Ni system combined with a constant heat input used during the deposition of the wall. Typical solidification structures comprising of cellular and columnar dendritic features are observed in the microstructures of both the deposits, as highlighted in Figure 5.4. The formation of these structures results from the interplay between the thermal gradient (G) and the interface growth rate (R) in the melt pool, and the undercooling [16]. The G/R ratio in the melt pool controls the formation of the different grain structures such as planar, cellular, columnar dendritic and equiaxed dendritic, as discussed in section 2.2. As the G/R ratio decreases, the morphology of the substructures transforms from planar to cellular, then to columnar dendritic, and finally towards equiaxed dendritic at low G/R ratios or high undercoolings [17].

Considering a single melt pool in the microstructures obtained in this study, planar solidification was observed near the fusion lines, due to the thermal gradient being highest at the bottom of the melt pool. As the distance from the bottom of the melt pool increases, the planar solidification destabilises, and cellular/columnar dendritic solidification occurs due to a decrease in the G/R ratio. The microstructural features shown here are typical for alloy 36 processed using powder and wire-based DED methods, and were also observed earlier, as shown in section 4.3.1 (chapter 4) [7, 18, 19].

The graded wall was further analysed by EBSD with simultaneous EDS measurements. These results pertaining to the chemically stable regions of alloy segments 42, 46, and 52 in the graded wall are shown in Figure 5.5. The image quality maps clearly reveal the presence of long columnar grains in the LTE alloy segments, similar to the results presented previously in section 4.3.1 for alloy 36 deposition. The phase maps reveal the presence of only the γ phase (FCC austenite) in the three alloy segments. This is in contradiction with the results of Qiu *et al.* [20], as their EBSD results showed the presence of the γ phase along with precipitates of the α phase (BCC) in the microstructure of alloy 36 fabricated by selective laser melting. The

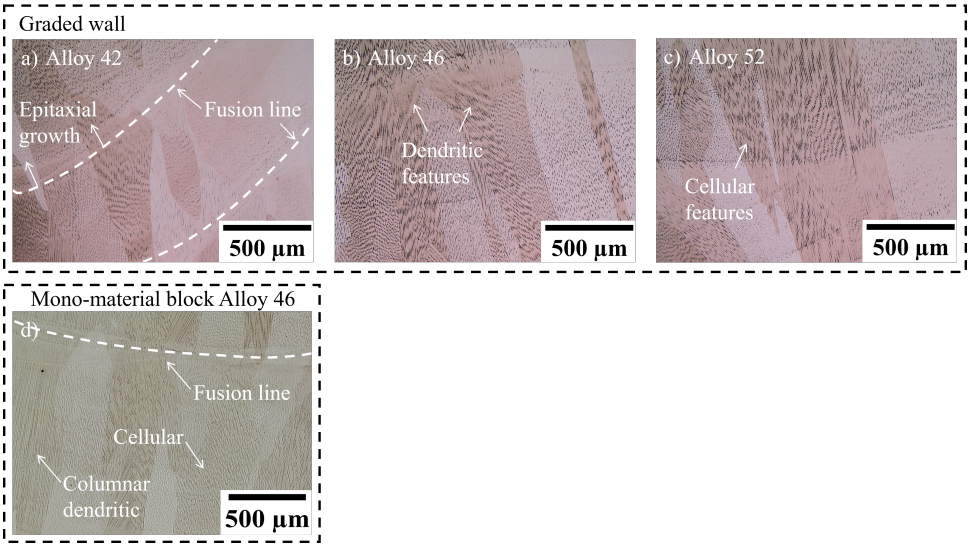

Figure 5.4: Microstructure of LTE alloy segments 42, 46, and 52, from the graded wall in (a), (b) and (c), respectively, and mono-material alloy 46 block in (d), revealing the grain morphology and sub-grain features.

observation of the α phase can be attributed to the nature of the feedstock material used in this study, which consisted of a mixture of Fe and Ni powders prepared to achieve the composition of alloy 36. Considering the relatively rapid solidification during selective laser melting, due to the high energy density of the heat source, the Fe–Ni powder blend is unlikely to mix adequately during solidification, which favours the stabilisation of the α phase.

The Ni maps of the alloy segments give evidence of a qualitative increase in the amount of Ni from alloys 42 to 46, and 52. Moreover, the Ni maps indicate a homogeneous distribution of Ni in the three in situ deposited alloy segments, as locally enriched regions in Ni are absent. This is further supplemented by chemical analyses of the three alloy segments in the graded wall, as presented in Figure 5.6. The locations where the map scans were taken for the three LTE alloy segments are marked by numbers, as shown in Figure 5.6 (a), and the results of the map scans corresponding to the three alloy segments are shown in Figure 5.6 (b). The maps show evidence of adequate chemical mixing between the alloy 36 and Ni wires during the twin-wire feeding process, as no clusters or segregated regions of Ni are observed. This behaviour is found to be consistent among the three LTE alloy compositions as seen from the map scans. Furthermore, it should be noted that the Ni wire is fed toward the side of the melt pool, as shown earlier in Figure 5.1. However, this does not cause any difference in the distribution of Ni across the width of the wall within a single layer. This is reflected in the map scans as they show similar results when comparing locations 1 to 2, 3 to 4, and 5 to 6.

In addition, the quantified Fe and Ni contents in alloy 42, 46, and 52 segments,

marked in Figure 5.6 (a), shows good stability of the elements throughout the wall width within a single layer, as shown in Figure 5.6 (c). Therefore, the flow in the melt pool can be considered sufficient to homogeneously distribute the added Ni during the twin wire-feeding process.

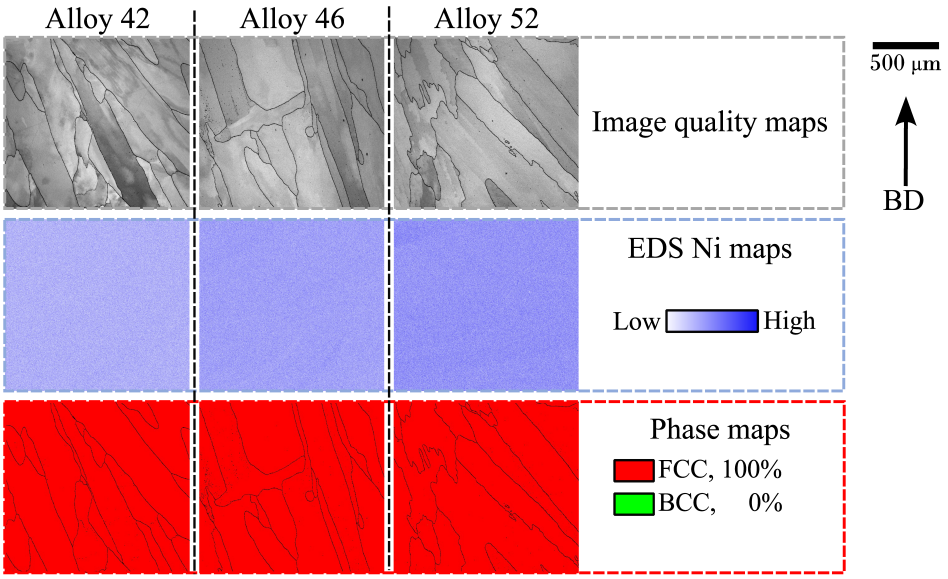

Figure 5.5: Image quality, Ni, and phase maps corresponding to the stable regions of alloy segments 42, 46, and 52 in the graded wall.

Point scans were performed to quantify the amount of Ni incorporated in the graded wall with the results presented as a colour map shown in Figure 5.7. Three distinct regions, characterised by average Ni contents of 42.0 ± 1.1, 45.8 ± 1.4, and 52.6 ± 0.8 wt.% were identified and are labelled, alloys 42, 46, and 52 in the figure, respectively. The low scatter in these measurements indicates that good control over the chemical composition can be achieved in the continuous metal transfer mode during the twin wire feeding process.

The Ni content in the first 2 layers is approximately 30–34 wt.% due to dilution with the base plate. However, in the third and fourth layers, it stabilises at approximately 36 wt.%, corresponding to the Ni content of the alloy 36 wire. Following this, the 2^{nd} wire is incorporated in the process to achieve the desired LTE alloy compositions of 42, 46, and 52 by varying the wire feed speeds of the two wires. In the transition regions, the Ni content varies between subsequent layers as the wire feed speeds of the alloy 36 and Ni wires are adjusted following the deposition of a layer. Therefore, in these regions, the Ni content gradually increases along the building direction (BD) until it approaches the required LTE alloy composition. The gradual change in the Ni content within the transition region implies that a sharp boundary between the thermal expansion properties can be avoided, thereby promoting structural compatibility among the different LTE alloy compositions. The

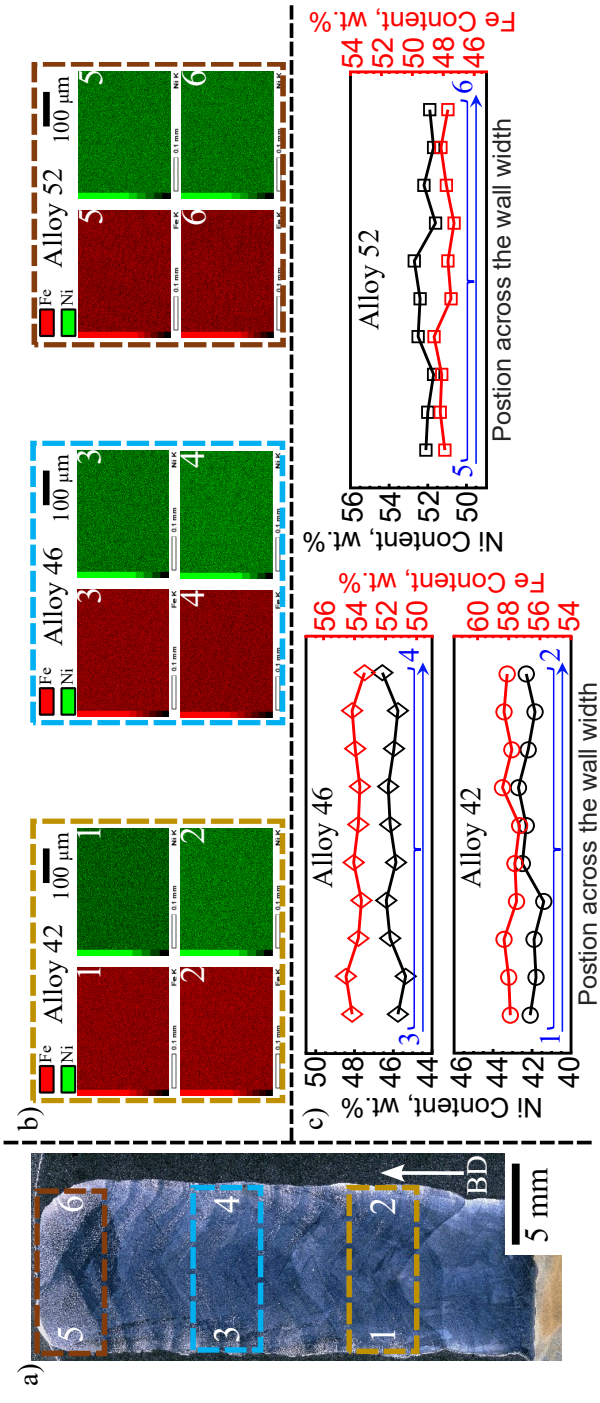

Figure 5.6: Transverse cross-section of the graded parallel to the building direction (BD) in (a). EDS maps corresponding to the numbered locations indicated in (a), shown in (b), and the results of the point scans shown in (c).

transition regions prior to each LTE alloy segment comprise approximately 2 layers, compared to the stable chemical composition of an alloy segment that extends across approximately 3 layers in the graded wall. Moreover, the mono-material alloy 46 block demonstrated good mixing and stability in Ni incorporation, as evidenced by an average Ni content quantified at 46.4 ± 0.9 wt.%.

From a material point of view, the compositional stability of the in situ synthesised LTE alloys is witnessed due to the solid-solution compatibility between Fe and Ni, as governed by the Hume-Rothery rules of forming a substitutional solid-solution [21]. Combining this inherent solid-solution compatibility between Fe and Ni with the continuous metal transfer mode of the twin-wire GTAW process ensures geometrically and chemically stable deposition of LTE alloys. Consequently, providing precise control over the in situ synthesised alloys, thereby opening the possibilities for tailoring the thermal expansion properties. Hence, using the twin-wire approach in AW-DED, the desired compositions of low-expansion alloys were successfully obtained.

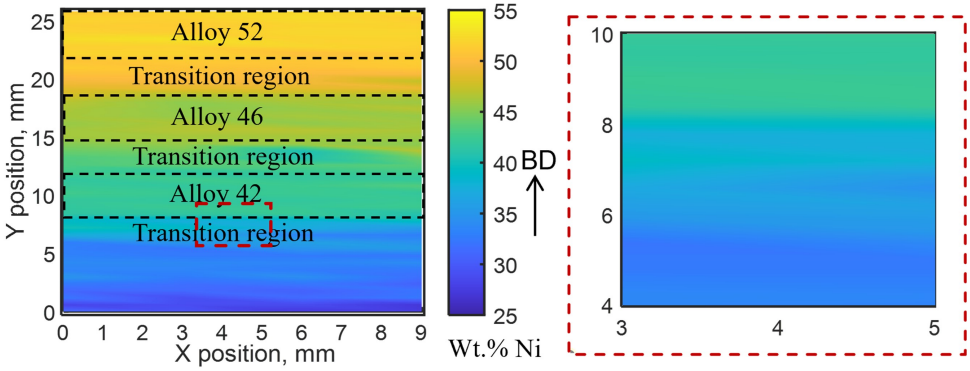

Figure 5.7: Colour map showing the distribution of Ni along the building direction of the graded wall as quantified by EDS point scans performed with a step size of 0.5 mm.

5.3.3. THERMAL PROPERTIES OF LOW THERMAL EXPANSION ALLOYS

The Curie temperature of the alloy segments in the graded wall was determined from the power versus temperature plots shown in Figure 5.8. The locations from which the specimens were extracted to establish the Curie temperatures are shown in Figure 5.8 (a). The plots in Figures 5.8 (b), (c), and (d) correspond to the specimens of alloy segments 42, 46, and 52, respectively. A clear jump in the applied power is observed in the plots of these segments. The measured Curie temperature of the as-deposited LTE alloys is comparable to that of the commercial alloys, as listed in Table 5.4. This further supports the results of the chemical analysis, which shows the compositional stability of the in situ synthesised LTE alloy compositions. In comparison, there is no evident jump in the power signal for the specimen taken from the transition region between the segments of alloys 42 and 46, but rather a sudden continuous variation,

as observed in Figure 5.8 (e). This can be attributed to the variation of the Ni content in this specimen, thereby not showing a clear Curie transition. However, the lower and upper bounds of the variation in the power signal are in agreement with the chemical compositional bounds of the specimen. The sudden disturbance in the power signal starts and ends at approximately 370 °C and 430 °C, respectively, which corresponds well with the Curie temperatures of the specimens pertaining to the segments of alloys 42 and 46.

The difference in the measured Curie temperatures of the as-deposited alloys compared to those of the commercial alloys is due to dissimilarities in the chemical compositions. On the one hand, the addition of elements, such as Mn, Si and Ti in the LTE Fe–Ni alloys of nominal composition causes a reduction in the Curie temperature [22]. On the other hand, the presence of cobalt is known to increase the Curie temperature and simultaneously decrease the thermal expansion [23, 24]. In this study, the alloy 36 wire has a maximum of 1 wt.% Co (≈ quantified as 0.40), while the Ni wire contained a maximum of 3.3 wt.% Ti (≈ quantified as 3.38). The effect of various alloying additions on the thermal expansion of alloy 36 is also shown in section 2.3. Moreover, the Curie temperature specification of the commercial LTE alloys is applicable to alloys that are nominally composed of binary Fe–Ni. Consequently, slight differences between the Curie points of the in situ deposited alloys and the commercial alloys are reasonable due to their respective chemical compositions.

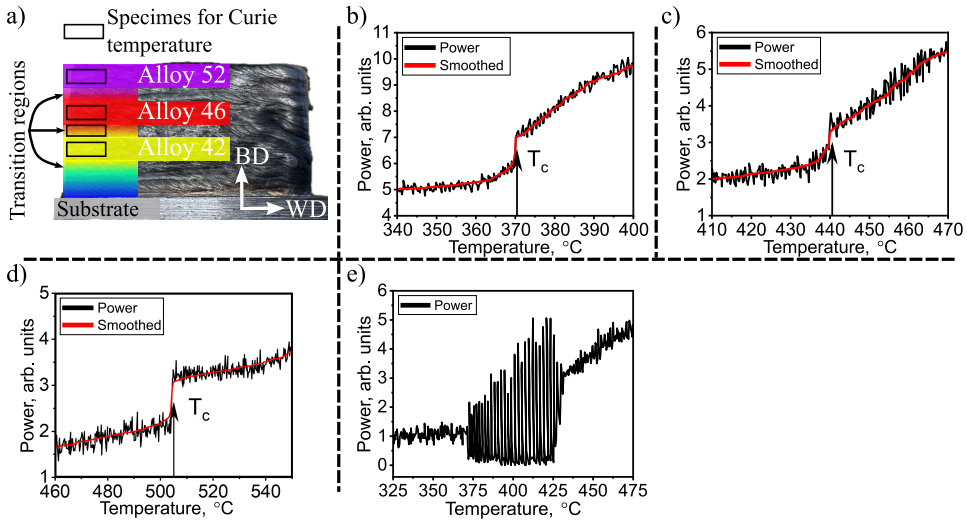

Figure 5.8: Overview of the graded wall schematically describing the orientation of the specimens extracted for the purpose of establishing the Curie temperatures in (a). The power-temperature plots of the as-deposited segments of alloys 42, 46, and 52 in (b), (c), and (d), respectively, and the transition region between alloy 42 and alloy 46 shown in (e).

In addition to the Curie temperature measurements of the as-deposited LTE alloy segments in the graded wall, the mean linear CTE values of alloy 46 in various

temperature ranges were also measured. The mono-material block of alloy 46 was used for this purpose. The temperature-displacement curves for specimens oriented in the building (V) and welding (H) directions of the mono-material block are shown in Figure 5.9 (a). In the temperature range between room temperature (RT) and approximately 410 °C, the alloy exhibits a low thermal expansion behaviour that is analogous to alloy 36. At temperatures above 410 °C, the thermal expansion is similar to that of a typical metal and is driven by lattice vibrations. However, at lower temperatures, the magnetovolume effects in the alloy compensate for the thermal expansion caused by lattice vibrations upon heating, thus resulting in the abnormal thermal expansion behaviour.

Table 5.4: Curie temperatures of the alloys produced by twin-wire feeding, compared with their commercial specifications [25].

Curie temperature, °C	Twin-wire feeding	Commercial specification
Alloy 42	371 ± 3.1	380
Alloy 46	441 ± 2.7	460
Alloy 52	505 ± 3.4	530

The mean linear CTE values of alloy 46 in various temperature ranges, presented in Figure 5.9 (b), were calculated from the curves shown in Figure 5.9 (a). The alloy shows an approximately constant thermal expansion in both orientations of the specimens for temperature ranges of 30–300 °C and 30–400 °C, as reflected by the mean CTE in Figure 5.9 (b). This is due to the characteristic Invar-type low thermal expansion behaviour of the Fe–Ni LTE alloys. The averages of the mean CTE values in different temperature ranges are higher for specimens oriented in the BD, as seen in Figure 5.9 (b). This is consistent with the trend observed for the mean CTE values of alloy 36, as reported in section 4.3.3 [26].

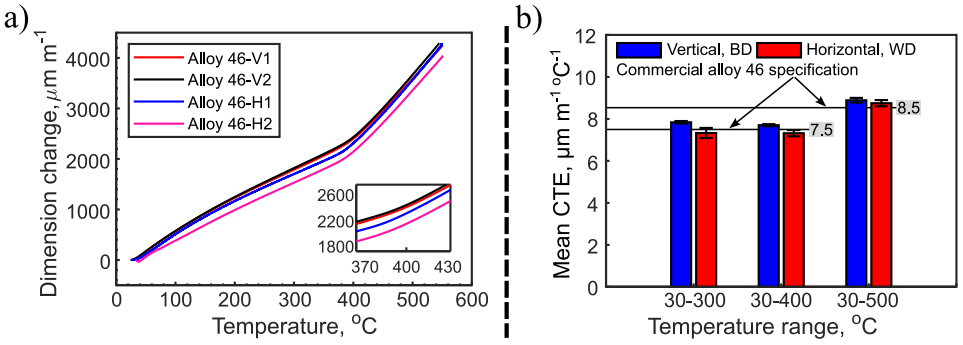

Figure 5.9: Temperature-displacement curves of the specimens extracted from the mono-material alloy 46 block oriented along the building (BD, V) and welding (WD, H) directions in (a). The corresponding linear mean CTE values of alloy 46 in various temperature ranges in (b).

The orientation-related differences in the mean CTE values are most likely to occur due to the build-up of non-uniform residual stresses during AW-DED, as addressed previously in section 4.3.3. Wang *et al.* [27] showed that residual stress anisotropy can lead to an effective thermal expansion anisotropy. In addition, stresses influence the magnetostriction of a magnetic material [28]. As the peculiarity in the thermal expansion behaviour of Fe–Ni alloys is due to the temperature-dependent compensation of the lattice thermal expansion by spontaneous volume magnetostriction, the thermal expansion behaviour of Fe–Ni LTE alloys will be affected under the influence of stresses.

The fabrication of components by AW-DED is subject to the development of residual stresses due to the intrinsic thermal cycles imposed on the component during processing [29]. Yakout *et al.* [30] showed the presence of tensile residual stresses (up to 350 MPa) in Invar 36 structures manufactured by laser-powder bed fusion (L-PBF). The residual stress states of the deposits were not quantified in this study, however, it is reasonable to assume the presence of residual stresses in the as-deposited mono-material block of alloy 46, likely exceeding in magnitude compared to the reported value in Invar 36 processed by L-PBF. Consequently, the anisotropy in the mean CTE values between the BD and WD oriented samples may be attributed to the influence of the stress-state in the block on the thermal expansion of alloy 46.

In addition, it is worth noting that the directional thermal expansion anisotropy observed in the CTE measurements is low, possibly because of the relaxation of residual stresses during the machining of the dilatometry samples. However, in a practical application of an as-deposited LTE alloy structure, this effect could become more pronounced. Therefore, a stress-relieving heat treatment based on the industrially employed Lement heat treatment, as described in section 2.3, may be sufficient to mitigate the impact of stress on the thermal expansion of the as-deposited LTE alloys [31]. In general, the CTE values of the as-deposited alloy 46 are comparable to those of the conventionally processed alloy. The compositional stability is also reflected in the similar character of the temperature-displacement curves for the different specimens. Hence, twin-wire feeding-based AW-DED is a suitable method for the on-demand generation of LTE alloys from the Fe–Ni system.

5.4. SUMMARY AND CONCLUSIONS

In summary, continuous and intermittent metal transfer modes were identified during the twin-wire feeding process. The continuous metal transfer mode was characterised by the formation of a persistent liquid metal bridge that allowed smooth transfer of Ni to the melt pool, resulting in a stable weld bead, as illustrated in Figure 5.10 (a). In contrast, the intermittent metal mode results in the formation of metal droplets at the tip of the Ni wire, as shown in Figure 5.10 (b). The entry of these droplets into the melt pool can lead to instabilities, causing the weld bead to change spatially. Therefore, the continuous transfer mode was utilised to fabricate LTE Fe–Ni alloys using the twin-wire feeding process. Because of the stable deposition and optimum chemical mixing in this mode, the in situ fabricated LTE Fe–Ni alloys exhibit thermal properties comparable to those of commercially available alloys. Consequently, the

twin-wire feed approach during AW-DED can potentially be used to offset the challenges associated with the conventional processing of LTE Fe–Ni alloys, providing alloys with on-demand thermal expansion properties.

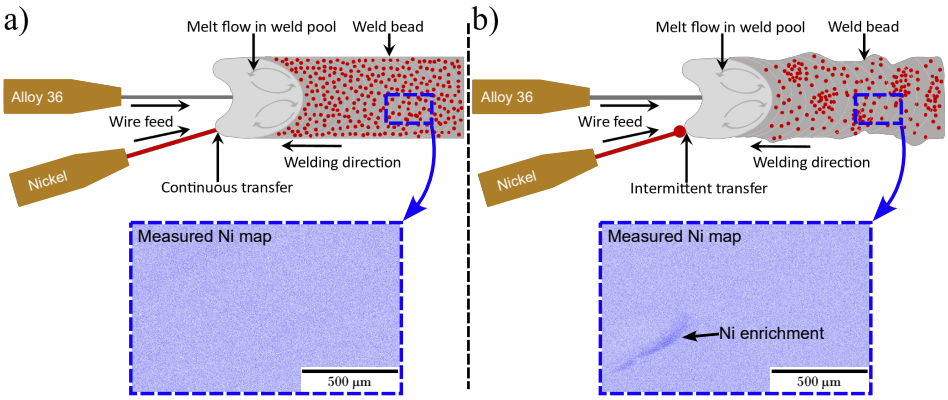

Figure 5.10: Schematic description of continuous metal transfer mode in (a), and intermittent metal transfer mode in (b), and the effect of the respective mode on the deposition and chemical stability during the twin-wire feeding process, shown by the corresponding measured Ni maps.

The following conclusions are drawn on the basis of the outcomes of this chapter:

1. The twin-wire feeding-based AW-DED enables the customised synthesis of Fe–Ni alloy compositions with low thermal expansion, providing the flexibility to tailor the thermal expansion properties of structures and obtain commercially unavailable alloy compositions.

2. The microstructure of the as-deposited low thermal expansion alloys 42, 46, and 52 is characterised by columnar grains and the formation of a single-phase austenitic structure.

3. The continuous metal transfer mode exhibits enhanced process stability relative to the intermittent metal transfer mode during the twin-wire feeding process, owing to the lack of melt pool instabilities in this mode.

4. Good control over desired compositions is achievable, regardless of the dynamic nature of the twin-wire feeding process. This is attributed to the observed stability within the continuous metal transfer mode and the solid solution compatibility inherent to the Fe–Ni alloy system.

5. The low thermal expansion alloys fabricated in situ through the twin-wire feeding process exhibit Curie temperatures and mean coefficients of thermal expansion that are comparable with those observed in conventionally produced alloys.

REFERENCES

[1] A. Sahoo and V. R. Medicherla. *Fe-Ni Invar alloys: A review*. Materials Today: Proceedings 43, 2 (2021), pp. 2242–2244. DOI: 10.1016/j.matpr.2020.12.527.

[2] E. F. Wassermann. *The Invar problem*. Journal of Magnetism and Magnetic Materials 100, 1–3 (1991), pp. 346–362. DOI: 10.1016/0304-8853(91)90828-X.

[3] *Low-expansion alloys introduction and overview*. Alloying: Understanding the Basics. Ed. by J. R. Davis and J. Davis. ASM International, 2001, pp. 587–594.

[4] S. Chikazumi, T. Mizoguchi, N. Yamaguchi, and P. Beckwith. *The Invar problem*. Journal of Applied Physics 39, 2 (1968), pp. 939–944. DOI: 10.1063/1.1656337.

[5] D. A. Colling and W. J. Carr. *Invar anomaly*. Journal of Applied Physics 41, 13 (1970), pp. 5125–5129. DOI: 10.1063/1.1658625.

[6] E. L. Frantz. *Low-expansion alloys*. Properties and Selection: Nonferrous Alloys and Special-Purpose Materials. Vol. 2. ASM International, 1990, pp. 889–896. DOI: 10.31399/asm.hb.v02.a0001099.

[7] H. Asgari, M. Salarian, H. Ma, A. Olubamiji, and M. Vlasea. *On thermal expansion behavior of invar alloy fabricated by modulated laser powder bed fusion*. Materials and Design 160 (2018), pp. 895–905. DOI: 10.1016/j.matdes.2018.10.025.

[8] B. Mills and A. H. Redford. *Machinability of engineering materials*. Dordrecht: Springer Science & Business Media, 1983. DOI: 10.1007/978-94-009-6631-4.

[9] C. Zhang *et al. Additive manufacturing of functionally graded materials: A review*. Materials Science and Engineering A 764, no. 138209 (2019). DOI: 10.1016/j.msea.2019.138209.

[10] V. Bhavar, P. Kattire, S. Thakare, S. Patil, and R. K. P. Singh. *A review on functionally gradient materials (FGMs) and their applications*. IOP Conference Series: Materials Science and Engineering 229, 1, no. 012021 (2017). DOI: 10.1088/1757-899X/229/1/012021.

[11] L. D. Bobbio, R. A. Otis, J. P. Borgonia, R. P. Dillon, A. A. Shapiro, Z. K. Liu, and A. M. Beese. *Additive manufacturing of a functionally graded material from Ti-6Al-4V to Invar: Experimental characterization and thermodynamic calculations*. Acta Materialia 127 (2017), pp. 133–142. DOI: 10.1016/j.actamat.2016.12.070.

[12] L. D. Bobbio, B. Bocklund, R. Otis, J. P. Borgonia, R. P. Dillon, A. A. Shapiro, B. McEnerney, Z. K. Liu, and A. M. Beese. *Experimental analysis and thermodynamic calculations of an additively manufactured functionally graded material of V to Invar 36*. Journal of Materials Research 33, 11 (2018), pp. 1642–1649. DOI: 10.1557/jmr.2018.92.

[13] D. C. Hofmann, S. Roberts, R. Otis, J. Kolodziejska, R. P. Dillon, J. O. Suh, A. A. Shapiro, Z. K. Liu, and J. P. Borgonia. *Developing gradient metal alloys through radial deposition additive manufacturing*. Scientific Reports 4, no. 5357 (2014). DOI: 10.1038/srep05357.

[14] *Invar M93 pipes and tubes for LNG transfer lines*. ArcelorMittal. Accessed: Mar. 12, 2025. Available: https://www.spacematdb.com/spacemat/manudatasheets/Invar%20M93.pdf. 2008.

[15] A. Ebrahimi, C. R. Kleijn, and I. M. Richardson. *A simulation-based approach to characterise melt-pool oscillations during gas tungsten arc welding*. International Journal of Heat and Mass Transfer 164, no. 120535 (2021). DOI: 10.1016/j.ijheatmasstransfer.2020.120535.

[16] T. DebRoy, H. L. Wei, J. S. Zuback, T. Mukherjee, J. W. Elmer, J. O. Milewski, A. M. Beese, A. Wilson-Heid, A. De, and W. Zhang. *Additive manufacturing of metallic components – Process, structure and properties*. Progress in Materials Science 92 (2018), pp. 112–224. DOI: 10.1016/j.pmatsci.2017.10.001.

[17] S. Kou. *Weld metal solidification II: Microstructure within grains*. Welding Metallurgy. 2nd ed. Hoboken: John Wiley & Sons, Inc., 2003. Chap. 8, pp. 199–214. DOI: 10.1002/0471434027.ch8.

[18] H. Tan, Y. Wang, G. Wang, F. Zhang, W. Fan, Z. Feng, and X. Lin. *Investigation on microstructure and properties of laser solid formed low expansion Invar 36 alloy*. Journal of Materials Research and Technology 9, 3 (2020), pp. 5827–5839. DOI: 10.1016/j.jmrt.2020.03.108.

[19] F. Veiga, A. Suárez, T. Artaza, and E. Aldalur. *Effect of the heat input on wire-arc additive manufacturing of Invar 36 alloy: Microstructure and mechanical properties*. Welding in the World 66, 6 (2022), pp. 1081–1091. DOI: 10.1007/s40194-022-01295-4.

[20] C. Qiu, N. J. E. Adkins, and M. M. Attallah. *Selective laser melting of Invar 36: Microstructure and properties*. Acta Materialia 103 (2016), pp. 382–395. DOI: 10.1016/j.actamat.2015.10.020.

[21] W. C. Leslie and E. Hornbogen. *Physical metallurgy of steels*. Physical Metallurgy. Ed. by R. W. Cahn and P. Haasen. 4th ed. Vol. 2. North-Holland, 1996. Chap. 17, pp. 1555–1620. DOI: 10.1016/B978-044489875-3/50022-3.

[22] M. Tsuda. *Effect of minor alloying elements on the mean thermal expansion coefficient of Fe36Ni invar alloy*. Tetsu-to-Hagane 80.12 (1994), pp. 944–949. DOI: 10.2355/tetsutohagane1955.80.12_944.

[23] V. M. Kalinin, F. N. Dunaev, and V. A. Kornyakov. *Effect of alloying elements on the Curie point of Fe-Ni invar alloys*. Soviet Physics Journal 5 (1970), pp. 129–131. DOI: 10.1007/BF00823460.

[24] C. Chen, B. Ma, S. Miao, and B. Liu. *Effect of cobalt on microstructure and mechanical properties of invar alloy*. Advances in Materials Processing. Ed. by Y. Han. Springer Singapore, 2018, pp. 855–864. DOI: 10.1007/978-981-13-0107-0_84.

[25] Carpenter Technology. *Controlled-Expansion Alloys*. CRS Holdings, Inc. Accessed: Mar. 04, 2025. Available: https://www.carpentertechnology.com/hubfs/PDFs/Controlled-ExpansionAlloys.pdf.

[26] A. Sood, J. Schimmel, V. M. Ferreira, M. Bosman, C. Goulas, V. Popovich, and M. J. Hermans. *Directed energy deposition of Invar 36 alloy using cold wire pulsed gas tungsten arc welding: Effect of heat input on the microstructure and functional behaviour*. Journal of Materials Research and Technology 25 (2023), pp. 6183–6197. DOI: doi.org/10.1016/j.jmrt.2023.06.280.

[27] X. L. Wang, C. M. Hoffmann, C. H. Hsueh, G. Sarma, C. R. Hubbard, and J. R. Keiser. *Influence of residual stress on thermal expansion behavior*. Applied Physics Letters 75, 21 (1999), pp. 3294–3296. DOI: 10.1063/1.125329.

[28] B. D. Cullity and C. D. Graham. *Magnetostriction and the effects of stress*. Introduction to Magnetic Materials. 2nd ed. Hoboken: John Wiley & Sons, Inc., 2009, pp. 241–275. DOI: 10.1002/9780470386323.

[29] Q. Wu, T. Mukherjee, A. De, and T. DebRoy. *Residual stresses in wire-arc additive manufacturing – Hierarchy of influential variables*. Additive Manufacturing 35, no. 101355 (2020). DOI: 10.1016/j.addma.2020.101355.

[30] M. Yakout and M. A. Elbestawi. *Residual stress formation in laser-based powder bed fusion (PBF-LB) of Invar 36*. ASTM Special Technical Publication. ASTM International, 2020, pp. 34–44. DOI: 10.1520/STP163120190149.

[31] B. S. Lement. *The dimensional behavior of Invar*. Ph.D. thesis. Cambridge, Massachusetts: Massachusetts Institute of Technology, 1949.

6

ENHANCING THE DEPOSITION AND CRACKING RESISTANCE OF ALLOY 36 DURING AW-DED[§]

IN this chapter, the phenomenon of intergranular cracking in alloy 36 during AW-DED is addressed through the combined approach of accelerated cooling via a CO_2 jet and the addition of TiC particles. Accelerated cooling was shown to reduce interpass deposition times and the susceptibility to cracking due to increased heat dissipation. A crack-free microstructure was achieved only when combined with the addition of TiC particles, which were observed to pin the high-angle grain boundaries and induce tortuosity, thereby limiting abnormal grain growth and mitigating intergranular cracking. Mechanical performance was restored compared to the cracked condition, and the critical low thermal expansion performance of the as-deposited alloy 36 was improved due to the enhanced ferromagnetic character of the alloy.

6.1. INTRODUCTION

The aerospace industry relies on alloy 36 moulding tools during the curing process of composite material-based aerospace structures. The minimal mismatch between the mean linear coefficient of thermal expansion (CTE) of alloy 36 and the composite materials ensures precise dimensional control of the composite structures during the curing process. For instance, the spring-back distortion of a 0.24 m carbon fibre composite aerospace antenna was shown to be approximately 20% lower when manufactured using an alloy 36 moulding tool, compared to a stainless steel AISI 430 tool [1]. Therefore, alloy 36 moulding tools enable the production of high-quality

[§]The contents of this chapter are in part based on a journal article published as: A. Sood, M. Bosman, R. Huizenga, C. Goulas, V. Popovich, and M. J. M. Hermans. *Enhanced cracking resistance and deposition of alloy 36 via accelerated cooling and TiC addition during wire arc additive manufacturing'*. Virtual and Physical Prototyping 20, 1, no. e2469827 (2025).

aerospace structures that retain their intended dimensionality after undergoing curing cycles. However, the traditional production of alloy 36 component through the subtractive manufacturing route has faced challenges related to cost, material waste, and the ability to create complex geometries [2, 3].

Advancements in metal additive manufacturing (AM) have opened new avenues for fabricating the unique alloy 36. In particular, arc wire-directed energy deposition (AW-DED) stands-out among metal AM processes for its ability to produce medium to large-scale components while maximising the deposition rates [4]. In recent years, substantial research has been conducted to expand the application of AM techniques in processing alloy 36 [5–15]. Despite the success in fabricating alloy 36 through the AM route, multiple studies report the persistence of intergranular cracking in the observed microstructures. Qiu *et al.* [16] observed the presence of cracks in as-printed and post-treated microstructures of alloy 36 deposited via selective laser melting. Tan *et al.* [17] employed laser metal deposition to fabricate alloy 36 specimens and reported the dependence of intergranular cracking on the laser scanning speed, given a constant laser power and spot diameter. Additionally, in chapter 4, the deposition of alloy 36 using AW-DED was explored at heat inputs (HI) ranging from 200–550 $J\,mm^{-1}$ [18]. Except for the alloy deposited at the lowest HI setting, intergranular cracking was encountered at other HI settings. In general, lowering the HI during AW-DED reduces the susceptibility of intergranular crack-sensitive alloys to cracking. However, this approach compromises a crucial advantage of AW-DED over other metal additive manufacturing (AM) methods, namely the ability to achieve high deposition rates. The reduction in HI inherently leads to a decrease in deposition rates, undermining the key benefit of high deposition rates in AW-DED. Therefore, it becomes essential to explore alternative strategies that do not rely on reducing the HI to address the challenge of cracking in alloy 36 during AW-DED. This chapter builds on the results presented in chapter 4 and aims to mitigate intergranular cracking during AW-DED of alloy 36 at the higher extreme of HI, i.e. 550 $J\,mm^{-1}$, which resulted in significant intergranular cracking as described in section 4.3.2. The higher HI regime is particularly relevant from a production perspective, as a higher HI translates to increased deposition rates. Moreover, it is also crucial from the standpoint of enhancing the mechanical properties, given that the presence of intergranular cracks has a deleterious impact on the tensile properties of alloy 36.

Table 6.1: Overview of the blocks deposited in this chapter.

Blocks	Conditions
SR	Reference
SCL	Accelerated cooling
SA to SC	Cooling and variable TiC
SDM	Deposition conditions of block SC

In this chapter, gas tungsten arc welding (GTAW) in pulsed current mode with front wire feeding was used to deposit alloy 36. To mitigate intergranular cracking from alloy 36, the deposition approach consists of providing a solid-state CO_2 cooling jet through the substrate and applying a paste containing TiC particles between the

deposited layers. The deposition conditions corresponding to the experiments are summarised in 6.1. The effect of the cooling jet on the deposits was characterised by melt pool observations and measurements of the time-temperature curves. The microstructural response of alloy 36 to the combined deposition approach of accelerated cooling and TiC particle addition was established through X-ray fluorescence (XRF), X-ray diffraction (XRD) and electron backscatter diffraction (EBSD) techniques. Lastly, mechanical and dilatometric tests were performed to quantify the functional performance of the as-deposited alloy. The results of this study demonstrate the geometrically stable deposition of alloy 36 structures at an increased HI, facilitated by the incorporation of a cooling jet during AW-DED. When combined with TiC particle addition, this approach enables defect-free fabrication of alloy 36 with improved functional performance compared to its conventional counterpart.

6.2. EXPERIMENTAL OVERVIEW

Table 6.2: The process parameters used in this chapter during the deposition experiments. TS–travel speed, WFS–wire feed speed, I_{base}–base current, I_{peak}–peak current, t_{base}–base time, t_{peak}–peak time, U_{ave}–average voltage, and HI–heat input.

HI J mm^{-1}	TS mm s^{-1}	WFS mm s^{-1}	I_{base} A	I_{peak} A	t_{base} s	t_{peak} s	U_{ave} V
550	3.2	50.0	135	300	0.2	0.2	12.0

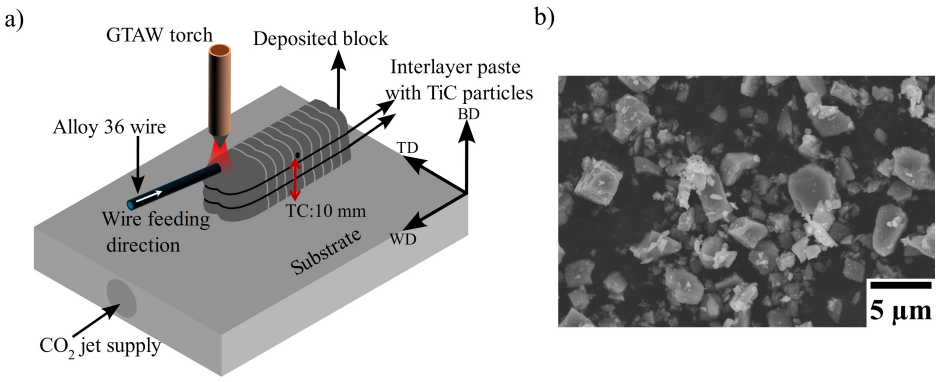

Figure 6.1: Schematic diagram of the AW-DED process employed in this study incorporating a CO_2 jet and interlayer paste with TiC particles in (a). Morphology of the TiC particles used in the present study, shown in (b).

The experiments comprised depositing five alloy 36 blocks, 10 layers each, of $80 \times 15 \times 15\,mm^3$ at a HI of $550\,J\,mm^{-1}$: a reference block without using CO_2 jet cooling and TiC powder particles, a block with accelerated CO_2 jet cooling, and three

blocks with accelerated cooling and varying amounts of TiC particles. The process parameters that comprise the heat input condition used in this chapter are listed in Table 6.2. A through hole of 8 mm diameter was drilled in the substrates used for blocks SA to SC to supply the CO_2 jet during deposition. The TiC powder particles were manufactured by Sigma Aldrich and were of 99.9% purity with a size limitation of 325 mesh. The deposition process is schematically described in Figure 6.1 (a). The TiC particles were mixed with a polyurethane resin and manually applied as a coating between successive passes. This method of powder application was adapted from other studies [19, 20]. The morphology of the as-received TiC powder particles is shown in Figure 6.1 (b). The alloy 36 wire was front fed to the melt pool during the experiments as seen in Figure 6.1 (a).

A specialised welding camera (Cavitar C300) with built-in laser illumination was used to observe the melt pool during the deposition process. The thermal history during the deposition process was recorded using K-type thermocouples connected to a YOKOGAWA DL 750 ScopeCorder data logger at a sampling rate of 1 kHz. The thermocouple (TC) was welded in the middle of the deposited bead at a height of approximately 10 mm from the substrate, as depicted in Figure 6.1 (a). An interpass temperature of $70 \pm 5\,°C$ was maintained during the deposition process. The microstructural characteristics of the deposited blocks were characterised using optical microscopy, SEM, XRD, and EBSD techniques. During EBSD analyses, a step size of 5 µm was used to obtain grain boundary maps, while a step size of 0.05 µm was used to reveal the incorporated TiC particles and the resulting effect on grain boundary morphology. Sample surfaces parallel to the BD-TD plane were used for microstructural characterisation. Similar surfaces were used to quantify the Ti content of the blocks through XRF. The carbon content was measured using a LECO elemental analyser by taking four 1 g samples from each block containing TiC particles.

Mechanical properties of the block deposited with the highest content of TiC particles were also measured. A larger block of $130 \times 15 \times 60\,mm^3$, referred to as block SDM, was deposited for the purpose of extracting rectangular plate-type tensile specimens. The geometry of the tensile specimen is shown previously in Figure 3.4. Tensile tests were performed at room temperature on two sets of samples, with orientations parallel to the building (BD, vertical) and welding (WD, horizontal) directions. A total of 8 samples were extracted with 4 samples per direction. Lastly, the mean linear thermal expansion coefficient (CTE) of samples extracted from block SDM was also quantified using a furnace-heated dilatometer. Cylindrical specimens of $\phi 4\,mm \times 10\,mm$ were machined for this purpose. The temperature-displacement (T-D) curves were measured for two sets of samples: the first set, oriented along the building direction (three samples), and the second set, oriented along the welding direction (three samples), to establish the properties in two directions. Detailed information on sample preparation and the characterisation techniques employed in this study can be found in chapter 3.

6.3. RESULTS AND DISCUSSION

6.3.1. DEPOSITION OVERVIEW AND MELT POOL OBSERVATIONS

The measured time-temperature curves during the deposition of alloy 36 for the cases when external cooling was off (reference) and on are shown in Figure 6.2 (a) and (b), respectively. An approximately constant interpass (T_i) temperature of 70 °C was maintained between successive passes for both cases as indicated in the figures. For the reference case, the time taken to deposit 5 beads was approximately 2100 s. In comparison, when accelerated cooling was used, the time taken to deposit five beads decreased to approximately 650 s, representing a 70% reduction. The accumulation of heat due to successive passes was also evident during the deposition without the use of accelerated cooling. The times t_1 to t_4 indicate the interpass times in Figure 6.2 (a-0) and are also applicable to Figure 6.2 (a-1). These interpass times are ordered as follows: $t_1 < t_2 < t_3 < t_4$ in the reference/no cooling case, and $t_1 < t_2 \approx t_3 \approx t_4$ in the accelerated cooling case. The accumulation of heat during AW-DED of alloy 36 can be attributed to the relatively low thermal diffusivity of the alloy [21]. For instance, the thermal diffusivity of alloy 36 at room temperature is approximately 3.2×10^{-6} m^2 s^{-1}, whereas for stainless steel 304 and low carbon steel, the values are approximately 4.0×10^{-6} m^2 s^{-1} and 1.9×10^{-5} m^2 s^{-1}, respectively [22–24].

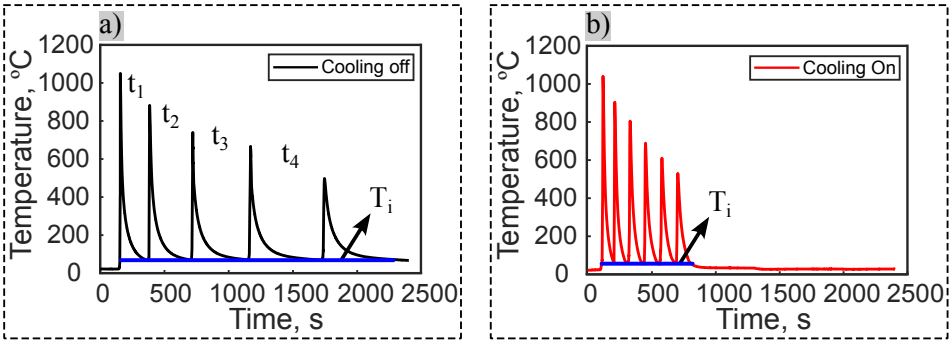

Figure 6.2: Time-temperature curves obtained during the deposition of alloy 36 without and with an accelerated cooling CO_2 jet in (a) and (b), respectively.

Melt pool observations were performed to establish the effect of cooling on the melt pool characteristics using a specialised welding camera. The melt pool observed in the cases of reference and accelerated cooling conditions is shown in Figure 6.3 (a) and (b), respectively, from which the respective melt pool length was obtained. The length of the melt pool in the reference case at t = 11 s during the deposition was measured as 18.8 mm. At a similar time, i.e. 13 s, during the deposition case with accelerated cooling, the length of the melt pool is measured as 15.3 mm. Due to the build-up of heat, the melt pool in the reference case is more elongated than in the case of external cooling. The melt pool elongates when the rate of latent heat release upon solidification at the tail of the melt pool along the centreline exceeds the heat dissipation rate [25]. The application of a CO_2 jet to the substrate effectively dissipates heat by imposing a heat sink effect on the substrate, thus preventing the

elongation of the melt pool. Furthermore, the strategy of forced cooling through the substrate ensures a homogeneous cooling effect throughout the deposition process, as the cooling jet remains active until the desired interpass temperature (~ 70 °C in this study) is achieved. The uniform cooling effect provided by the jet is evident in the relatively consistent length of the melt pool at time instances of t = 6 s, and t = 13 s, during the deposition case with accelerated cooling, as shown in Figure 6.3 (b).

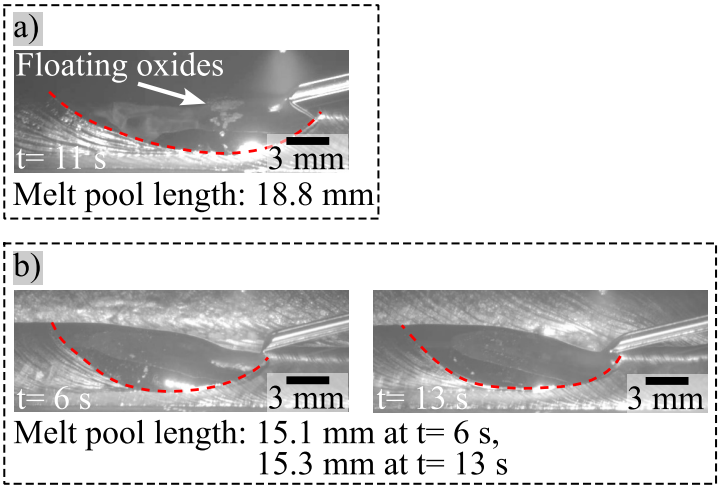

Figure 6.3: The observed melt pool during the deposition of alloy 36 without and with an accelerated cooling CO_2 jet in (a) and (b), respectively.

Large oxide islands floating on the melt pool were also observed for the reference case, as indicated in Figure 6.3 (a). These oxides are likely to form in the reference case due to a lack of appropriate shielding for the elongated melt pool. Upon solidification of the melt pool, these oxides appear on the deposited beads and negatively affect the surface quality, thus increasing the risk of lack of fusion defects unless properly cleaned. In addition, these oxides can be retained in the microstructure of the deposited material as inclusions. In general, the net effect of cooling is to promote heat extraction during AW-DED. This, in turn, is expected to reduce the tendency of grain coarsening during the deposition of the single-phase alloy 36 at a microstructural level.

6.3.2. MICROSTRUCTURAL AND CHEMICAL ANALYSES

The microstructures of alloy 36 under various deposition conditions are presented in Figure 6.4. Severe grain coarsening or abnormal grain growth is observed in the reference case (SR), leading to the formation of intergranular cracks. An example of this is shown in Figure 6.4 (a), where the crack is observed to form at the triple point of the coarse grains. The SEM observation of the crack flank reveals a wavy appearance, and some isolated instances of micro-dimples (Figure 6.4 (a-0)), thus suggesting limited ductility. The intergranular nature of the crack at the triple junction

of coarsened grains, combined with the characteristic morphology of the crack flank, confirms that the observed cracking is associated with the phenomenon of ductility-dip cracking (DDC). These findings are consistent with the results reported in section 4.3.2 (chapter 4).

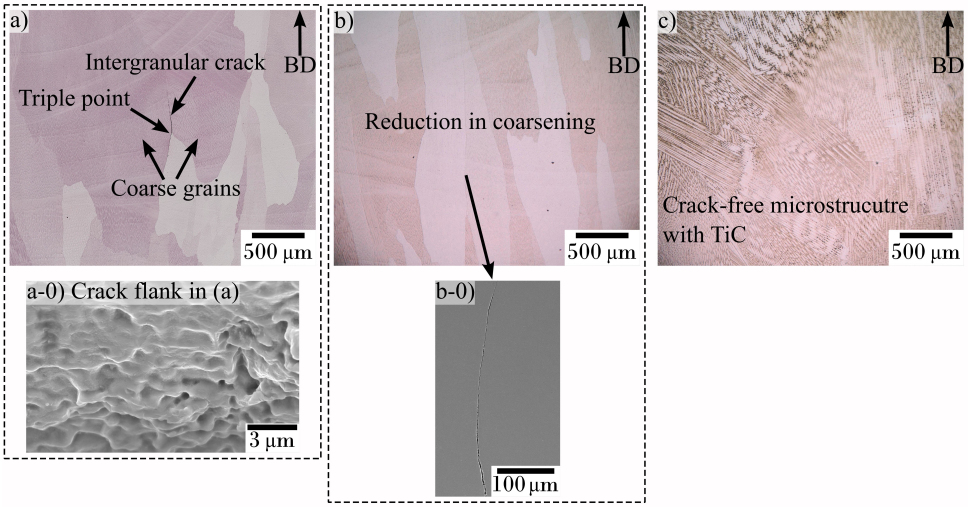

Figure 6.4: Microstructure of a sample from block SR showing coarsened grains and an intergranular crack in (a). Reduction in the extent of grain coarsening though accelerated cooling during the deposition of block SCL shown by the micrograph in (b), and an intergranular crack in (b-0). Crack-free microstructure of alloy 36 achieved through the addition of TiC in (c), corresponding to a sample from block SC.

Accelerated CO_2 jet cooling was employed to prevent grain coarsening during the deposition of alloy 36 (block SCL), and the resulting microstructure is shown in Figure 6.4 (b). At first glance, the cooling strategy appears to be effective in reducing grain coarsening, which in turn prevents the formation of large intergranular cracks, such as the one shown in Figure 6.4 (a). However, SEM observations revealed the persistence of micro-cracks in the microstructure obtained after using the cooling jet, as depicted in Figure 6.4 (b-0).

Table 6.3: Measured Ti and C contents in the as-deposited blocks.

Sample, wt.%	SA	SB	SC
Ti (XRF)	0.33 ± 0.01	0.52 ± 0.03	0.71 ± 0.04
C (LECO)	0.08 ± 0.01	0.16 ± 0.01	0.24 ± 0.02

The cooling strategy was further combined with the interlayer application of TiC powder particles during AW-DED of alloy 36. The designation and chemical composition of the blocks deposited with the combined approach of accelerated

cooling and TiC powder particles are listed in Table 6.3. The microstructure of block SC was found to be free of cracks, as shown in Figure 6.4 (c). Furthermore, the microstructure of block SC is observed to be more refined than that of block SR. Detailed analyses of the microstructures in blocks SR, SCL, and SA to SC were performed using EBSD, and the corresponding grain boundary maps are shown in Figure 6.5 (a), (b), and (c) to (e), respectively. Coarse columnar grains with non-tortuous grain boundaries are revealed in Figure 6.5 (a). The extent of grain coarsening is reduced in block SCL (only cooling), as observed in Figure 6.5 (b). The addition of TiC particles significantly modified the microstructures in terms of grain boundary morphology and columnar grain widths. As the TiC content increases (blocks SA to SC), the grain boundaries develop tortuosity, accompanied by a simultaneous reduction in the columnar grain width, as listed in Table 6.4, which was calculated using the linear intercept method [26]. This can also be qualitatively observed when comparing the grain boundary maps shown in Figure 6.5 (a)–(e).

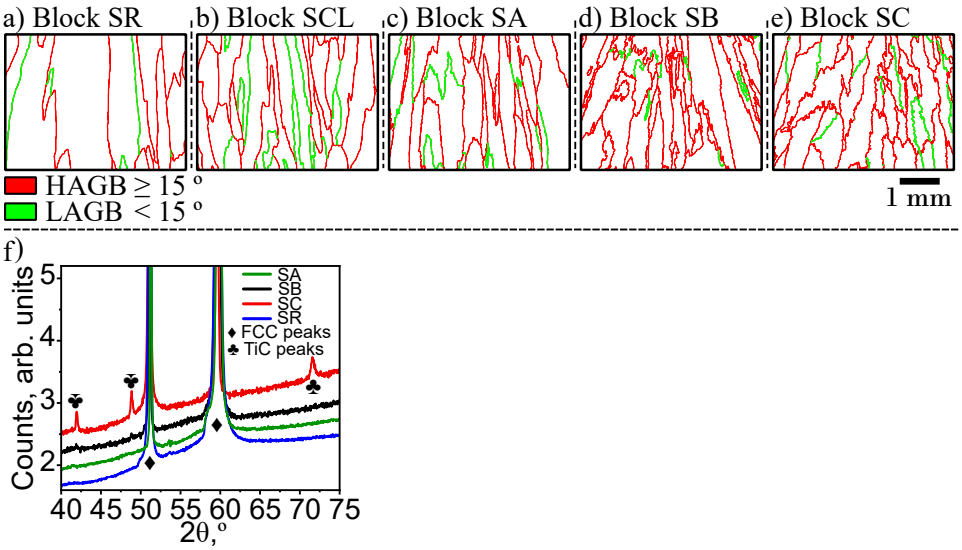

Figure 6.5: Grain boundary maps for samples of blocks SR, SCL, SA, SB, and SC in (a), (b), (c), (d), and (e), respectively. XRD patterns for samples of blocks SA, SB, SC, and SR revealing the detection of clear TiC peaks in the patterns of samples SB and SC in (f).

The grain boundary maps of blocks SB and SC also revealed the presence of stray equiaxed-like grains. This indicates that TiC particles can act as a grain-refining inoculant during AW-DED of alloy 36 by promoting heterogeneous nucleation. However, the limited occurrence of equiaxed-like grains in the microstructures of blocks SB and SC suggests that the content of TiC particles was likely insufficient to promote heterogeneous nucleation uniformly throughout the blocks. Future work can be undertaken to better understand the extent of heterogeneous nucleation in alloy 36 facilitated by TiC particles during AW-DED. The presence of ductility-dip

Table 6.4: The average columnar grain widths measured from the transverse cross-sections (BD–TD planes) of the deposited blocks. The cross-sections were taken at 25, 35, 45, and 55 mm from the start of the blocks.

Blocks	Average columnar grain width, μm
SR	1280 ± 260
SCL	760 ± 210
SA	510 ± 120
SB	470 ± 80
SC	380 ± 90

micro-cracks, similar to the crack shown in Figure 6.4 (b), was occasionally observed in the microstructures of blocks SA and SB. However, cracks were eliminated from block SC, which contained higher amount of TiC than blocks SA and SB. This suggests that a minimum level of TiC addition was necessary to completely prevent cracking during AW-DED of alloy 36. Phase identification was performed using XRD, and the resulting XRD patterns are presented in Figure 6.5 (f). Clear TiC peaks were identified in the patterns of samples taken from blocks SC and SB, with the absence of these peaks in the pattern of the sample taken from block SA. However, the peak intensities corresponding to the TiC phase were reduced in the pattern of block SB compared to block SC. The TiC phase fractions were quantified as 0.3% and 0.7% by weight, with an error of ± 0.2%, in blocks SB and SC, respectively.

The microstructure of block SC was further analysed with a low-step size setting during EBSD to investigate the introduction of TiC particles. The grain maps, phase maps, and simultaneous EBSD-EDS map scans for block SC, are shown in Figure 6.6. In general, the grain boundaries (GB) were decorated with faceted and irregularly shaped particles, as shown in Figure 6.6 (Intergranular TiC). Most of these particles were observed to be submicrometre in size, with few instances of particles ranging from submicrometre to micrometre scale. In modified Ni-base alloys, the presence of medium-sized precipitates (NbC or TiC), such as the intergranular TiC particles observed in Figure 6.6, has been reported to increase the resistance of these alloys to DDC during welding [27]. Similarly, the grain interiors also exhibited the presence of such particles (Intragranular TiC in Figure 6.6). However, most of the particles were observed at intergranular locations. An example of a nano-sized particle within a grain of block SC can be seen in Figure 6.6 (Nano-TiC). The corresponding EDS maps in Figure 6.6 show Ti enrichment, thus providing positive confirmation of TiC particles. The tortuosity in the GB arises from the presence of TiC particles. In addition, the alloy 36 material surrounding the TiC particles is observed to contain a negligible amount of Ti, as indicated by relatively weak Ti signal in the EDS maps. In summary, the tortuous GB resulting from the incorporation of TiC particles restricts grain growth, thus increasing the resistance to DDC compared to the non-tortuous GB of block SR [28, 29]. Altogether, these particles contribute to the clear TiC peaks observed in the XRD pattern of block SC, as shown earlier in Figure 6.5 (f). In comparison, the reduced peak intensity and the absence of TiC peaks in the XRD

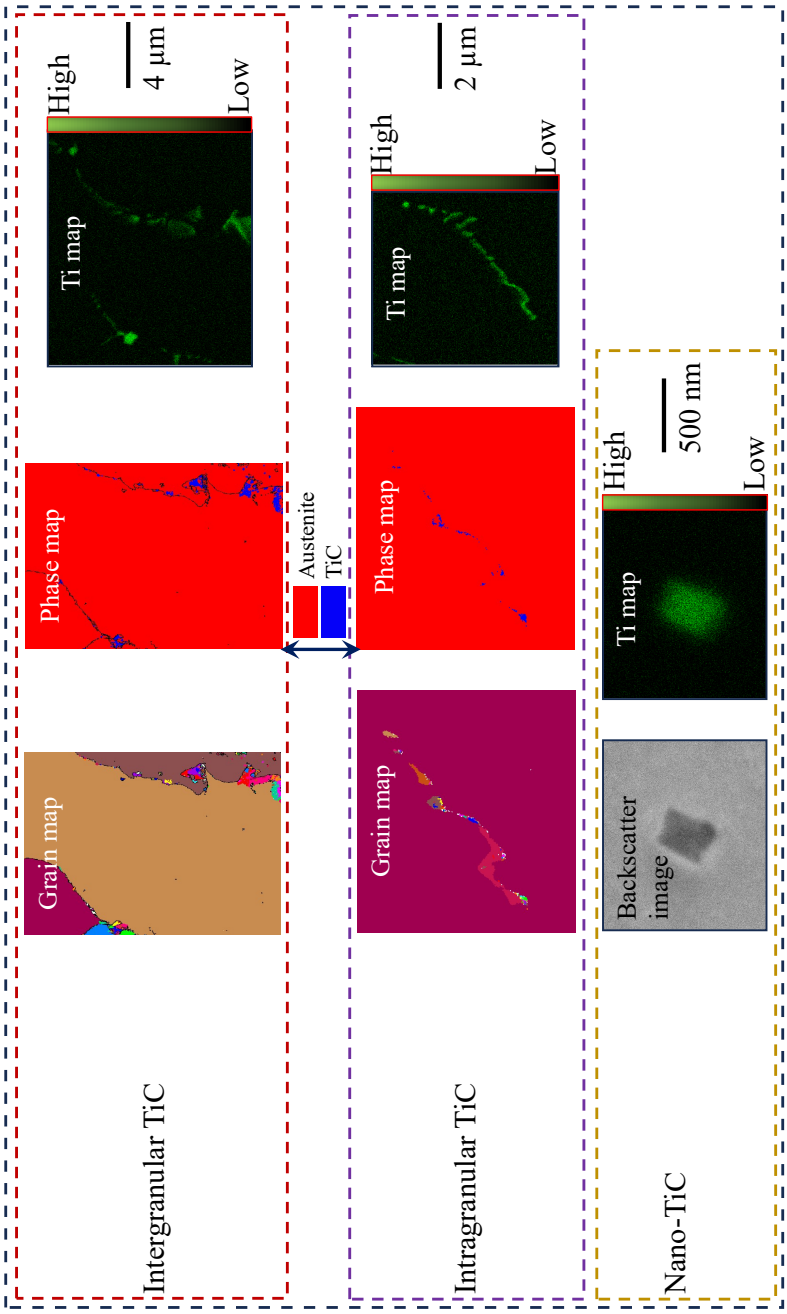

Figure 6.6: Morphology of the TiC particles observed in the microstructure of a sample taken from block SC.

patterns of blocks SB and SA can be attributed to the limited presence of nano-TiC particles. An example of such nano-TiC particles observed in the microstructure of block SB is shown in Figure 6.7.

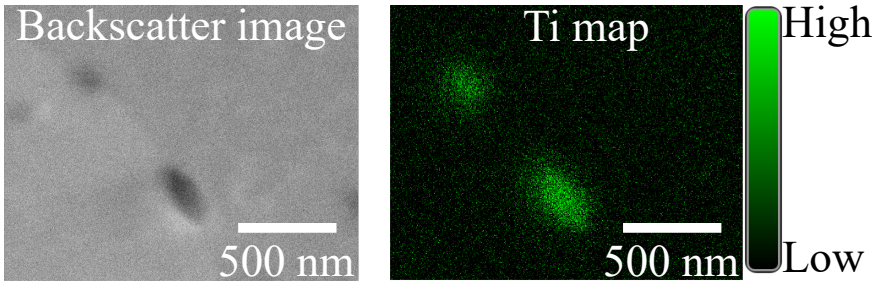

Figure 6.7: Chemical analysis of nano-TiC particles observed in the microstructure of a sample taken from block SB.

The mechanism responsible for the reduced susceptibility of alloy 36 to intergranular DDC due to accelerated cooling and the addition of TiC is schematically shown in Figure 6.8. During AW-DED of alloy 36, heat accumulation may occur due to the relatively low thermal diffusivity of the alloy [21]. This, along with the persistence of the alloy in the single-phase austenitic structure up to its liquidus temperature, promotes a microstructure conducive to grain coarsening. The propensity for grain coarsening arises from the low activation energy of grain growth in alloy 36 and the tendency of a system to minimise free energy through boundary migration [21, 30]. Therefore, grain coarsening occurs during AW-DED of alloy 36, as schematically illustrated in Figure 6.8 (a), leading to a net reduction in the total GB area.

Furthermore, AW-DED inherently induces non-uniform thermal stresses or strains, which the deposited material accommodates [31]. The reduction in GB area due to abnormal grain coarsening during AW-DED increases the stress/strain accommodated per GB. When the localised stress or strain surpasses the GB strength, intergranular DDC occurs, as shown schematically in Figure 6.8 (a).

A cooling system, such as the CO_2 jet utilised in this study, facilitates heat extraction from alloy 36 during AW-DED, thereby limiting grain coarsening, as illustrated in Figure 6.8 (b). The cooling jet mitigates heat accumulation by effectively transforming the substrate into a heat sink. Hence, the thermal energy available for GB migration and the duration for which the material remains at elevated temperatures are reduced. This promotes the retention of a greater GB area compared to the condition in Figure 6.8(a), where accelerated cooling is not applied. Consequently, the extent of DDC is reduced, with GBs exhibiting smaller and thinner cracks or micro-cracks, as observed in Figure 6.8 (b), in contrast to the larger crack shown in Figure 6.8 (a). The persistence of micro-cracks despite utilising accelerated cooling can be attributed to the overall cooling effect on the deposited material rather than a more targeted local cooling approach, such as directing the cooling jet behind the melt pool. Furthermore, the microstructure of alloy 36 deposited with accelerated cooling exhibits non-tortuous GBs, similar to those depicted in Figure

6.8 (a), which are inherently susceptible to DDC [28]. Naturally, alleviating DDC

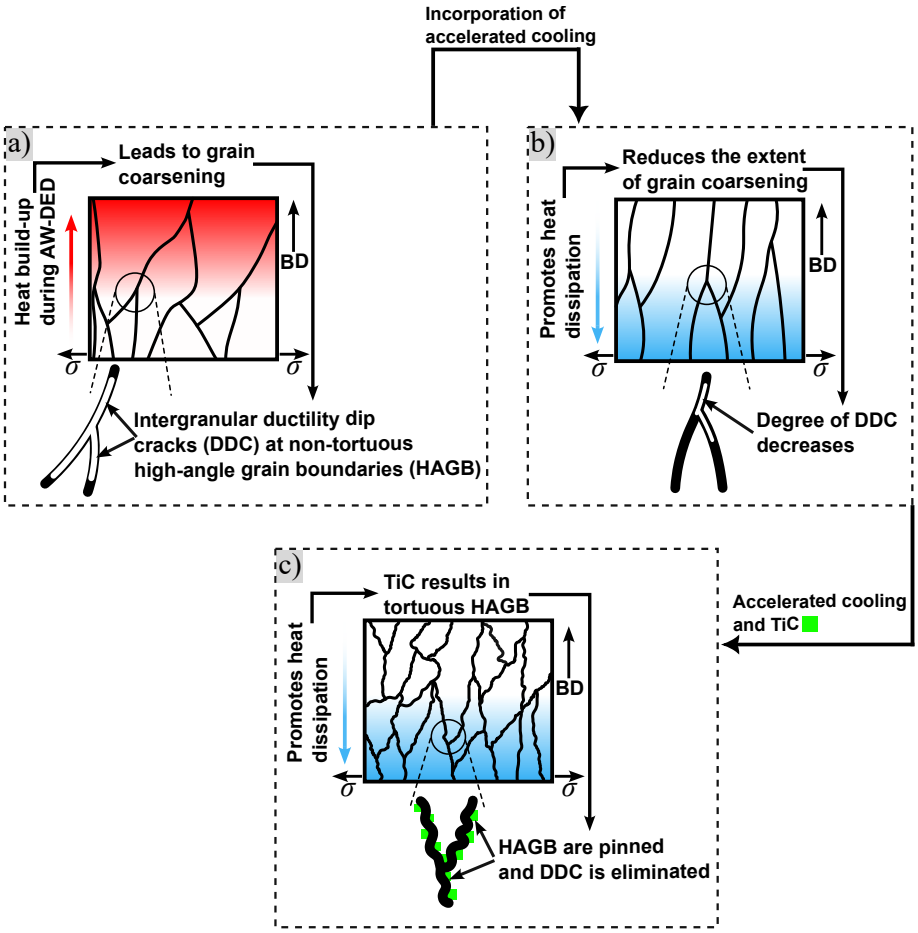

Figure 6.8: Schematic illustration of the microstructure development in alloy 36 during AW-DED in (a), by incorporating accelerated cooling in (b), and a combination of accelerated cooling and TiC particles in (c). Macroscopic stress acting in the microstructure is indicated by σ.

from alloy 36 during AW-DED requires modification of the GB morphology [32, 33]. This can be achieved by introducing TiC particles, as shown in Figure 6.8 (c). The presence of TiC particles in the melt pool allows effective pinning of the GB during solidification, thereby restricting their migration. This restriction on GB movement further reduces grain coarsening, leading to a decrease in columnar grain widths with increasing TiC content, as observed in blocks SA to SC. Additionally, the presence of equiaxed-like grains, similar to those observed in the microstructures of blocks SB and SC, contributes to increasing the GB area. The restriction on GB migration due to the presence of TiC particles helps to retain their tortuous morphology. This tortuosity

of the GB may also provide a mechanical interlocking effect between adjacent grains. Consequently, in block SC, the GBs transition from crack-susceptible to crack-resistant upon the introduction of TiC particles.

In summary, the microstructure of the as-deposited alloy 36 consists of columnar grains aligned along the building direction. However, these grains are susceptible to severe coarsening due to heat build-up during the deposition process, as observed in the microstructure of the reference (SR) sample. This coarsening can be mitigated by employing an external cooling strategy during deposition, such as the CO_2 jet used in this study, which effectively promotes heat dissipation. The accelerated cooling strategy also reduces the extent of DDC in alloy 36 due to its influence on the microstructure. Nevertheless, the combined approach of cooling and the incorporation of TiC powder particles was necessary to eliminate DDC in alloy 36. This indicates that the cooling strategy alone, as applied in this study, was insufficient to completely prevent DDC. An improvement of the cooling strategy could involve the development of a setup utilising a specialised nozzle capable of delivering a cooling medium trailing the arc. Future studies employing this setup during the deposition of alloy 36 are recommended, as the present study demonstrates a noticeable improvement in both the microstructure and the interpass times of alloy 36 deposited with accelerated cooling.

In addition, the use of accelerated cooling may also have been beneficial in reducing the minimum amount of TiC required to eliminate DDC. Without cooling, it is highly likely that alloy 36 would remain prone to grain coarsening until higher amounts of TiC than those used in block SC are incorporated, due to the heat accumulation effects during AW-DED. Ductility-dip cracking is characterised by GB failure due to their reduced ductility at elevated temperatures under the influence of stress/strain [34]. In general, single-phase fcc alloys (alloy 36) are prone to DDC due to a loss of GB ductility at elevated temperatures [27, 35]. The fabrication of alloy 36 by AW-DED subjects the material to the ideal conditions for DDC, namely elevated temperatures caused by molten metal deposition and the generation of process-induced stresses/strains. During AW-DED of alloy 36, the addition of TiC particles effectively pins the GBs and induces tortuosity, thereby resisting grain coarsening. These combined effects, resulting from the presence of TiC particles at GBs, promote a crack-free microstructure by reducing the susceptibility of alloy 36 to DDC.

6.3.3. FUNCTIONAL PROPERTIES

The engineering stress-strain curves obtained from the tensile tests performed on samples from block SDM are shown in Figure 6.9 (a). The properties were evaluated along two directions of the block to quantify any directional anisotropy. This is represented by the results of samples oriented in the horizontal (H, WD) and the vertical (V, BD) directions. As shown in Figure 6.9 (b), the mechanical properties of block SDM are in good agreement with the expected values from the wire manufacturer specifications (MS), regardless of orientation. This agreement is attributed to the absence of DDC in block SDM. The tensile properties corresponding to the reference in Figure 6.9 (b) are adapted from section 4.3.3 (chapter 4) to highlight

the detrimental effect of DDC on the mechanical performance of as-deposited alloy 36. Intergranular ductility-dip cracks act as stress concentrators or sites for preferential damage, leading to premature failure of alloy 36 subjected to tensile loading. In contrast, the addition of TiC increases the resistance of the grain boundaries to DDC by effectively pinning them and preventing crack formation. The average tensile strength, yield strength, and elongation of alloy 36 deposited with the combined approach are increased by 24%, 18%, and 60%, respectively, compared to the reference alloy. Hence, DDC during AW-DED of alloy 36 is mitigated by the combined approach of accelerated cooling and the addition of TiC particles, thus recovering or exceeding the expected mechanical properties of alloy 36.

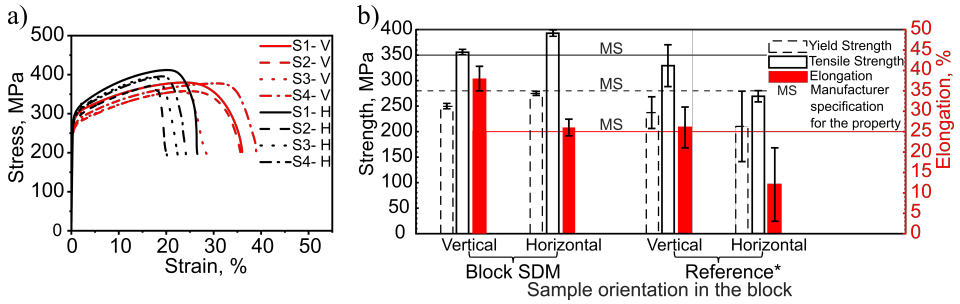

Figure 6.9: Measured strain-strain curves of the specimens extracted from block SDM oriented along the building (V) and welding (H) directions in (a). Tensile properties calculated from the curves in (a), shown in (b). *: The poor tensile properties for reference in (b) are adopted from section 4.3.3.

However, the mechanical properties are observed to vary depending on the orientation of the specimens in the block. The horizontally oriented specimens are found to be stronger and less ductile compared to vertically oriented specimens. This strength-ductility anisotropy between the horizontally and vertically oriented specimens can be related to the strong directionality of the columnar grains. The vertical specimens are extracted with their length oriented along the building direction of block SDM, which aligns the specimen length with the long axis of the columnar grains. Due to this alignment, the grain boundary density in the vertical specimens is reduced relative to the horizontal specimens. Consequently, the hindrance to dislocation slip by grain boundaries is lower in vertical specimens than in horizontal specimens. This results in the conflicting behaviour of strength and ductility between the horizontally and vertically oriented specimens. A similar trend has also been observed in other studies addressing the mechanical properties of S304L steel and alloy 36 fabricated by AW-DED [7, 36].

The measured temperature-displacement (T-D) curves of specimens from block SDM are shown in Figure 6.10 (a). For comparison, an averaged T-D curve of two samples from SR block (without cooling or TiC addition) is also added to the figure. The mean linear coefficient of thermal expansion (CTE) in different temperature ranges were calculated from these curves and are presented in Figure 6.10 (b). No significant anisotropy was observed between the CTE of specimens oriented vertically

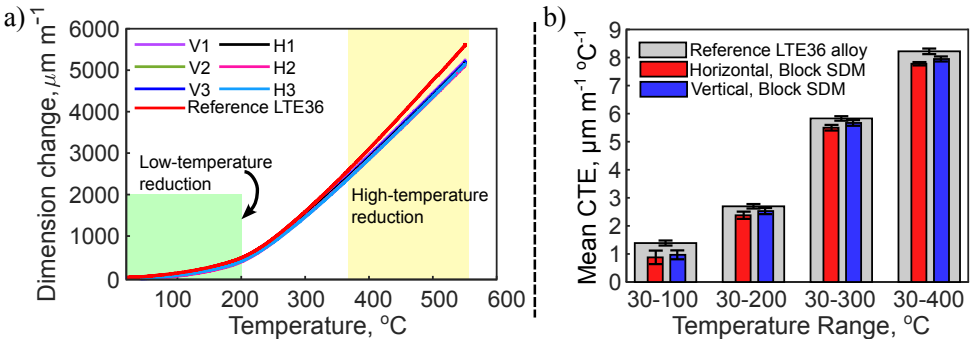

Figure 6.10: Temperature-displacement curves of the specimens extracted from block SDM oriented along the building (V) and welding (H) directions in (a). Mean CTEs in various temperature ranges calculated from the T-D curves in (a), shown in (b).

and horizontally within the block. However, a noticeable reduction in the CTE of specimens from block SDM is observed when compared to the CTE of the reference alloy 36 (block SR). This reduction of CTE is highlighted in two parts in Figure 6.10(a). Firstly, a prominent low-temperature reduction in the thermal expansion behaviour of block SDM, approximately 34% lower than reference, is revealed in the low-temperature range of 30–100 °C, i.e. well below the Curie transition. Secondly, a high-temperature reduction of the thermal expansion that occurs upon exceeding the ferromagnetic ordering temperature (Curie transition). This high-temperature reduction can be attributed to the composite nature of alloy 36 comprising TiC particles. The mean linear CTE of TiC particles, reported to be approximately 6.99 $\mu m\,m^{-1}\,°C^{-1}$ in a temperature range of 30–500 °C, is lower than that of the reference alloy 36 in the same range, which is 10.10 $\mu m\,m^{-1}\,°C^{-1}$, as determined from Figure 6.10 (a) [37]. The crossover between the mean CTE of the reference alloy 36 and TiC particles, determined from room temperature, occurs at around 300 °C; above this temperature, the CTE of TiC particles is lower than that of the reference alloy 36. The as-deposited alloy 36 comprising TiC particles can be considered a metal matrix composite. For such materials, the net thermal expansion is typically estimated using a rule-of-mixtures approximation. Hence, the lower CTE of TiC particles compared to that of the reference alloy 36 above temperatures of 300 °C leads to a high-temperature reduction in the CTE of alloy 36 comprising TiC particles (block SDM) relative to reference alloy 36 (block SR).

However, it should be noted that this high-temperature reduction holds little significance for aerospace mould tooling applications of alloy 36. This is because these tools are typically limited to a maximum operational temperature in the vicinity of 200 °C during the composite curing cycles [38].

Based on the above reasoning for the high-temperature reduction, it can also be argued that the mean linear CTE of alloy 36 comprising TiC particles in the temperature range of 30–100 °C should increase compared to that of the reference alloy 36. Since for temperatures below 300 °C, the CTE of TiC particles is higher than that of the reference alloy 36. Moreover, the CTE of alloy 36 in various temperature

ranges are expected to increase with the addition of Ti and C, provided these elements are present in the solid-solution matrix. However, the addition of TiC particles to alloy 36 in this study contributes marginally to the chemical composition of the solid-solution matrix. This is valid based on the low solubility product of TiC in austenite (0.0165 at 1200 °C), indicating that these particles remain stable with limited dissolution at high temperatures in the austenitic matrix of alloy 36 [39]. In addition, the Ti maps in Figure 6.6 reveal that the alloy 36 matrix surrounding the TiC particles lacks Ti. Consequently, the low thermal expansion behaviour of alloy 36 should be minimally influenced by TiC from the perspective of chemically induced changes. However, due to the repetitive thermal cycles in AW-DED, some degree of dissolution can be expected, which in turn could result in a marginal, yet observable increase in the CTE of alloy 36. For instance, the change in the CTE of FeNi36 alloy per mass % of Ti addition in the temperature range of 30–100 °C is reported to be approximately 0.86 µm m^{-1} °C^{-1} [40]. Hence, contrary to the expected increase in the same temperature range, a low-temperature reduction is observed in the thermal expansion behaviour of alloy 36 comprising TiC particles compared to that of the reference alloy 36, as highlighted in Figure 6.10 (a). This appears as a prominent reduction in the mean linear CTE of block SDM evaluated in the temperature range of 30–100 °C, relative to that of block SR, as shown in Figure 6.10 (b).

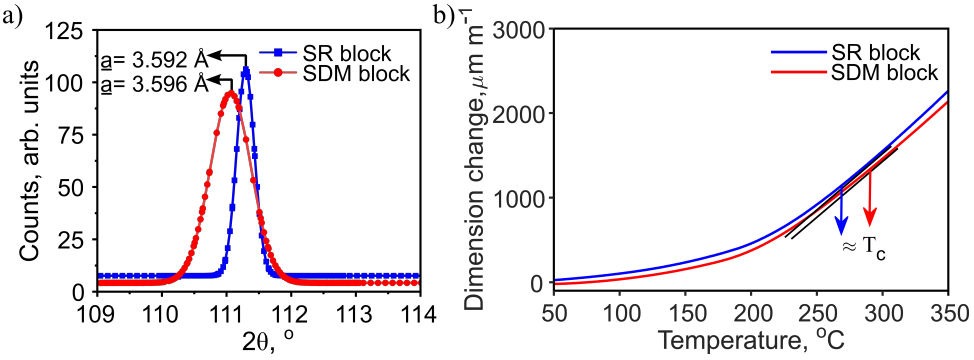

Figure 6.11: Lattice parameters obtained from the XRD patterns of specimens from blocks SR and SDM in (a), symbols correspond to the measured points to which the solid lines are fitted. Approximation of the Curie temperatures from the averaged T-D curves of samples from blocks SDM and SR in (b).

To understand the observed low-temperature reduction of CTE in this work, the effect of TiC addition on the lattice parameter of the deposited specimens was explored. The high-angle XRD diffraction peaks corresponding to specimens of blocks SR and SDM are shown in Figure 6.11 (a). The values of the lattice parameters (a), listed in Figure 6.11 (a), were calculated using the corresponding Nelson-Riley extrapolation plots [41]. In Figure 6.11 (a), it is evident that the addition of TiC resulted in an increase in the a value, from 3.592 Å to 3.596 Å, which reveals as a relative shift in the XRD peak positions. This suggests that the marginal increase in a value is linked to the reduction in CTE observed in this study. The relationship

between increasing a value and reduction in the CTE of alloy 36 can be explained based on the simultaneous improvement in magnetic exchange coupling. The magnetic exchange coupling (exchange interaction) is fundamental in the description of ferromagnetism [42, 43]. The increase in the a value is expected to influence the Fe-Fe exchange interaction such that its ferromagnetic character is enhanced. This argument is supported by the computational work of Rancourt *et al.* [44] that addressed the physical phenomenon underlying the low thermal expansion behaviour of Invar 36. Using local moment models, they demonstrated that the Fe-Fe magnetic exchange bonds in Invar 36 improve their ferromagnetic character as the interatomic separation increases. In addition to the computational work, Gorria *et al.* [45] provided experimental evidence using X-ray absorption spectroscopy, suggesting that stresses induced in Invar 36 by mechanical treatments primarily affect the Fe–Fe interatomic distances. An increase in these distances was found to favour ferromagnetism.

An estimate about the trend of the exchange integral can be made through the relationship between the ferromagnetic Curie temperature and the exchange integral, as described by the mean field theory in equation 6.1,

$$T_c = \frac{J_{ex} Z_T S(S+1)}{3k_B}, \tag{6.1}$$

where, T_c is the Curie Temperature, Z_T is the co-ordination number, S is the atomic spin quantum number, J_{ex} is the exchange integral, and k_B is the Boltzmann constant [46]. The Curie temperature and the exchange integral are directly proportional for a constant value of the other parameters, which is the case in this study. Therefore, T_c would only increase if the exchange integral, J_{ex}, increases. The Curie temperature for the SDM block is observed to be lower than that of block SR, as illustrated by the averaged T-D curves shown in Figure 6.11 (b). This implies that the difference in the T_c between blocks SDM and SR is due to the higher exchange integral, which arises from an increase in a value due to the addition of TiC in block SDM. The synergy between the lattice parameter and magnetic exchange interaction also supports the observed prominent reduction of the CTE in the low-temperature range, well below the Curie transition. Therefore, the increase in the lattice parameter of alloy 36 enhances its ferromagnetic character, and consequently its low thermal expansion behaviour. This leads to a prominent reduction in the CTE at temperatures well below the Curie transition, as observed in this chapter.

6.4. CONCLUSIONS

In this chapter, the effect of accelerating the cooling and adding TiC particles during AW-DED of alloy 36 was studied. The relationship between the process conditions and the functional behaviour of the low thermal expansion alloy was established. The results are concluded as follows:

1. Employing accelerated cooling during AW-DED of the single-phase alloy 36 reduces the susceptibility to ductility-dip cracking (DDC) and shortens the interpass times by approximately 70%. However, the elimination of DDC requires the addition of TiC particles.

2. The microstructure of alloy 36 is refined by adding TiC particles due to a reduction in the extent of grain coarsening during AW-DED. The degree of grain coarsening decreases as the TiC content increases, effectively promoting the pinning of high-angle grain boundaries (HAGBs). The TiC particles also induce tortuosity in the HAGBs. This morphological change further contributes to the reduction in susceptibility to DDC.

3. The tensile properties of alloy 36 containing TiC particles are significantly improved compared to the TiC-free alloy, which exhibits DDC. The average tensile strength, yield strength, and elongation increase by 24%, 18%, and 60%, respectively.

4. The mean CTE of alloy 36 comprising TiC particles in the temperature range of 30–100 °C is lower than that of the TiC-free alloy. This reduction is attributed to the increase in the lattice parameter observed in the TiC-containing alloy, which enhances the ferromagnetic character of the alloy.

REFERENCES

[1] D. B. Shah, K. M. Patel, A. I. Patel, V. Pariyal, and S. J. Joshi. *Experimental investigation on spring-back deformation during autoclave curing of parabolic antenna reflectors*. Composites Part A 115 (2018), pp. 134–146. DOI: 10.1016/j.compositesa.2018.09.017.

[2] N. Khanna and A. Srivastava. *Optimization and analysis of surface roughness for INVAR-36 in end milling operations*. Materials Today: Proceedings 5, 2 (2018), pp. 5281–5288. DOI: 10.1016/j.matpr.2017.12.111.

[3] S. M. Abbasi, M. Morakabati, R. Mahdavi, and A. Momeni. *Effect of microalloying additions on the hot ductility of cast FeNi36*. Journal of Alloys and Compounds 639 (2015), pp. 602–610. DOI: 10.1016/j.jallcom.2015.03.167.

[4] S. W. Williams, F. Martina, A. C. Addison, J. Ding, G. Pardal, and P. Colegrove. *Wire + arc additive manufacturing*. Materials Science and Technology 32, 7 (2016), pp. 641–647. DOI: 10.1179/1743284715Y.0000000073.

[5] F. Veiga, A. Suarez, E. Aldalur, and T. Artaza. *Wire arc additive manufacturing of invar parts: Bead geometry and melt pool monitoring*. Measurement 189, 110452 (2022), p. 110452. DOI: 10.1016/j.measurement.2021.110452.

[6] A. G. D. Val, X. Cearsolo, A. Suarez, F. Veiga, I. Altuna, and M. Ortiz. *Machinability characterization in end milling of Invar 36 fabricated by wire arc additive manufacturing*. Journal of Materials Research and Technology 23 (2023), pp. 300–315. DOI: 10.1016/j.jmrt.2022.12.182.

[7] F. Veiga, A. Suárez, T. Artaza, and E. Aldalur. *Effect of the heat input on wire-arc additive manufacturing of Invar 36 alloy: Microstructure and mechanical properties*. Welding in the World 66, 6 (2022), pp. 1081–1091. DOI: 10.1007/s40194-022-01295-4.

[8] E. Aldalur, A. Suárez, and F. Veiga. *Thermal expansion behaviour of Invar 36 alloy parts fabricated by wire-arc additive manufacturing*. Journal of Materials Research and Technology 19 (2022), pp. 3634–3645. DOI: 10.1016/j.jmrt.2022.06.114.

[9] J. Wang, R. Biswal, G. Chen, G. R. Pardal, Y. Lu, J. Ding, and S. Williams. *On the composition gradient of steel/Invar functionally graded material manufactured by wire-based direct energy deposition*. Additive Manufacturing 96, no. 104594 (2024), p. 104594. DOI: 10.1016/j.addma.2024.104594.

[10] A. Iturrioz, E. Ukar, and J. C. Pereira. *Influence of the manufacturing strategy on the microstructure and mechanical properties of Invar 36 alloy parts manufactured by CMT-WAAM*. International Journal of Advanced Manufacturing Technology 136 (2024), pp. 729–744. DOI: 10.1007/s00170-024-14853-5.

[11] T. Wegener, S. Pramanik, T. Niendorf, and J. Günther. *On the cyclic deformation behavior of wire-based directed energy deposited Fe-Ni Invar alloy*. Materials Science and Engineering: A 918, no. 147403 (2024). DOI: 10.1016/j.msea.2024.147403.

[12] A. Fernández-Zabalza, F. Veiga, A. Suárez, and J. R. A. López. *The use of virtual sensors for bead size measurements in wire-arc directed energy deposition*. Applied Sciences 14, no. 1972 (2024). DOI: 10.3390/app14051972.

[13] G. Jiao, X. Fang, M. Zhang, Z. Li, R. Cai, H. Wu, and K. Huang. *Synergistic improvement of mechanical property and thermal expansion of wire-arc DED Invar alloy enabled by a novel deposition strategy*. Journal of Manufacturing Processes 121 (2024), pp. 121–135. DOI: 10.1016/j.jmapro.2024.05.031.

[14] G. Jiao, X. Fang, X. Chen, N. Xi, M. Zhang, Y. Liu, H. Wu, and K. Huang. *The origin of low thermal expansion coefficient and enhanced tensile properties of Invar alloy fabricated by directed energy deposition*. Journal of Materials Processing Technology 317, no. 117994 (2023). DOI: 10.1016/j.jmatprotec.2023.117994.

[15] G. Jiao, X. Fang, X. Li, M. Zhang, Z. Zhang, H. Li, and K. Huang. *High performance ultrasonic vibration assisted Wire-arc directed energy deposition of Invar alloy*. Journal of Materials Processing Technology 332, 118543 (2024). DOI: 10.1016/j.jmatprotec.2024.118534.

[16] C. Qiu, N. J. E. Adkins, and M. M. Attallah. *Selective laser melting of Invar 36: Microstructure and properties*. Acta Materialia 103 (2016), pp. 382–395. DOI: 10.1016/j.actamat.2015.10.020.

[17] H. Tan, Y. Wang, G. Wang, F. Zhang, W. Fan, Z. Feng, and X. Lin. *Investigation on microstructure and properties of laser solid formed low expansion Invar 36 alloy*. Journal of Materials Research and Technology 9, 3 (2020), pp. 5827–5839. DOI: 10.1016/j.jmrt.2020.03.108.

[18] A. Sood, J. Schimmel, V. M. Ferreira, M. Bosman, C. Goulas, V. Popovich, and M. J. Hermans. *Directed energy deposition of Invar 36 alloy using cold wire pulsed gas tungsten arc welding: Effect of heat input on the microstructure and functional behaviour*. Journal of Materials Research and Technology 25 (2023), pp. 6183–6197. DOI: doi.org/10.1016/j.jmrt.2023.06.280.

[19] J. R. Kennedy, A. E. Davis, A. E. Caballero, S. Williams, E. J. Pickering, and P. B. Prangnell. *The potential for grain refinement of Wire-Arc Additive Manufactured (WAAM) Ti-6Al-4V by ZrN and TiN inoculation*. Additive Manufacturing 40, no. 101928 (2021). DOI: 10.1016/j.addma.2021.101928.

[20] M. J. Bermingham, S. D. McDonald, and M. S. Dargusch. *Effect of trace lanthanum hexaboride and boron additions on microstructure, tensile properties and anisotropy of Ti-6Al-4V produced by additive manufacturing*. Materials Science and Engineering: A 719 (2018), pp. 1–11. DOI: 10.1016/j.msea.2018.02.012.

[21] J. L. Corbacho, J. C. Suárez, and F. Molleda. *Grain coarsening and boundary migration during welding of Invar Fe-36Ni alloy*. Materials Characterization 41, 1 (1998), pp. 27–34. DOI: 10.1016/S1044-5803(98)00020-5.

[22] VDM Metals GmbH. *Vdm alloy 36*. https://www.vdm-metals.com/en/alloy36. Accessed: 2025-05-26. 2021.

[23] H.-M. Yun, R. J. Fields, and J. L. McClure. *Thermophysical properties of stainless steels*. Journal of Research of the National Institute of Standards and Technology 103, 2 (1998), pp. 165–172. DOI: 10.6028/jres.103.013.

[24] Y. Yamazaki, S. Ueda, K. Hasegawa, and K. Tsuchiya. *Measurement of thermal diffusivity and conductivity of steels by the laser flash method*. ISIJ International 42, 5 (2002), pp. 498–502. DOI: 10.2355/isijinternational.42.498.

[25] S. A. David and J. M. Vitek. *Correlation between solidification parameters and weld microstructures*. International Materials Review 34, 1 (1989), pp. 213–245. DOI: 10.1179/imr.1989.34.1.213.

[26] *Standard test methods for determining average grain size*. ASTM Standard E112-13, 2021.

[27] A. J. Ramirez and J. C. Lippold. *New insight into the mechanism of ductility-dip cracking in Ni-base weld metals*. Hot Cracking Phenomena in Welds. Ed. by T. Böllinghaus and H. Herold. Berlin: Springer-Verlag, 2005, pp. 19–41. DOI: 10.1007/3-540-27460-X_2.

[28] J. C. Lippold. *Solid-state cracking*. Welding Metallurgy and Weldability. Hoboken: John Wiley & Sons, Inc., 2015. Chap. 4, pp. 130–213.

[29] Y. Li, J. Wang, E. H. Han, W. Wu, and H. Hänninen. *Multi-scale study of ductility-dip cracking in nickel-based alloy dissimilar metal weld*. Journal of Materials Science and Technology 35, 4 (2019), pp. 545–559. DOI: 10.1016/j.jmst.2018.10.023.

[30] B. Gwalani, R. Salloom, T. Alam, S. G. Valentin, X. Zhou, G. Thompson, S. G. Srinivasan, and R. Banerjee. *Composition-dependent apparent activation-energy and sluggish grain-growth in high entropy alloys*. Materials Research Letters 7, 7 (2019), pp. 267–274. DOI: 10.1080/21663831.2019.1601644.

[31] H. Zhang, R. Li, J. Liu, K. Wang, Q. Weijian, L. Shi, L. Lei, W. He, and S. Wu. *State-of-art review on the process-structure-properties-performance linkage in wire arc additive manufacturing*. Virtual and Physical Prototyping 19, 1, no. e2390495 (2024). DOI: 10.1080/17452759.2024.2390495.

[32] J. Q. Chen, H. Lu, W. Cui, J. M. Chen, and Y. F. Huang. *Effect of grain boundary behaviour on ductility dip cracking mechanism*. Materials Science and Technology 30, 10 (2014), pp. 1189–1196. DOI: 10.1179/1743284713Y.0000000431.

[33] A. J. Ramirez, J. W. Sowards, and J. C. Lippold. *Improving the ductility-dip cracking resistance of Ni-base alloys*. Journal of Materials Processing Technology 179, 1–3 (2006), pp. 212–218. DOI: 10.1016/j.jmatprotec.2006.03.095.

[34] D. Qian, J. Xue, A. Zhang, Y. Li, N. Tamura, Z. Song, and K. Chen. *Statistical study of ductility dip cracking induced plastic deformation in polycrystalline laser 3D printed Ni-based superalloy*. Scientific Reports 7, no. 2859 (2017). DOI: 10.1038/s41598-017-03051-x.

[35] T. Böllinghaus, H. Herold, C. E. Cross, and J. C. Lippold. *Ductility-dip cracking*. Hot Cracking Phenomena in Welds II. Ed. by T. Böllinghaus, H. Herold, C. E. Cross, and J. C. Lippold. Springer, 2008. Chap. Part V, pp. 389–455. DOI: 10.1007/978-3-540-78628-3.

[36] L. Ji, J. Lu, C. Liu, C. Jing, H. Fan, and S. Ma. *Microstructure and mechanical properties of 304L steel fabricated by arc additive manufacturing*. MATEC Web of Conferences. Vol. 128. EDP Sciences, 2017. DOI: 10.1051/matecconf/201712803006.

[37] R. O. Elliott and C. P. Kempter. *Thermal Expansion of Some Transition Metal Carbides*. Journal of Physical Chemistry 62, 5 (1958), pp. 630–631. DOI: 10.1021/j150563a030.

[38] *Composites: Form and Manufacture*. Composite Materials for Aircraft Structures. Ed. by A. Baker, S. Dutton, and D. Kelly. 2nd ed. American Institute of Aeronautics and Astronautics (AIAA), 2004, pp. 113–169.

[39] K. Nakama, K. Sugita, and Y. Shirai. *Effect of MC type carbides on age hardness and thermal expansion of Fe-36 wt%Ni-0.2 wt%C alloy*. Metallography, Microstructure, and Analysis 2, 6 (2013), pp. 383–387. DOI: 10.1007/s13632-013-0101-9.

[40] M. Tsuda. *Effect of minor alloying elements on the mean thermal expansion coefficient of Fe36Ni invar alloy*. Tetsu-to-Hagane 80.12 (1994), pp. 944–949. DOI: 10.2355/tetsutohagane1955.80.12_944.

[41] J. B. Nelson and D. P. Riley. *An experimental investigation of extrapolation methods in the derivation of aaccurate unit-cell dimensions of crystals*. Proceedings of the Physical Society 57, 3 (1945), pp. 160–177. DOI: 10.1088/0959-5309/57/3/302.

[42] B. D. Cullity and C. D. Graham. *Magnetostriction and the effects of stress*. Introduction to Magnetic Materials. 2nd ed. Hoboken: John Wiley & Sons, Inc., 2009, pp. 241–275. DOI: 10.1002/9780470386323.

[43] J. M. D. Coey and S. S. P. Parkin, eds. *Handbook of magnetism and magnetic materials*. Springer Nature Switzerland AG, 2021. DOI: 10.1007/978-3-030-63210-6.

[44] D. G. Rancourt and M.-Z. Dang. *Relation between anomalous magnetovolume behavior and magnetic frustration in Invar alloys*. Physical Review B 54, 17 (1996), pp. 12225–12231. DOI: 10.1103/PhysRevB.54.12225.

[45] P. Gorria *et al. Stress-induced large Curie temperature enhancement in $Fe_{64}Ni_{36}$ Invar alloy*. Physical Review B 80, no. 064421 (2009). DOI: 10.1103/PhysRevB.80.064421.

[46] K. S. Anand, D. Goswami, P. P. Jana, and J. Das. *Correlating the lattice parameter and Curie temperature of γ-Ni in Fe-Ni-base alloys*. AIP Advances 9, 5, no. 055126 (2019). DOI: 10.1063/1.5097345.

7

GENERAL DISCUSSION, CONCLUSIONS AND OUTLOOK

7.1. GENERAL DISCUSSION AND CONCLUSIONS

THE present study employs gas tungsten arc welding-based directed energy deposition (DED) to fabricate low thermal expansion (LTE) Fe–Ni alloys, with a particular focus on alloy 36. This alloy exhibits an approximately invariant coefficient of thermal expansion in the vicinity of room temperature. As a result, alloy 36 is widely regarded as indispensable in the aerospace sector. However, given the challenges associated with machining and shaping the alloy using conventional subtractive manufacturing methods, the adoption of metal additive manufacturing (AM) presents a promising route for its efficient processing. Metal AM techniques generally offer increased processing flexibility for the fabrication of metre-sized components, especially when arc-wire AM processes are used. These technologies are distinguished by high deposition rates and minimal material waste, making them well-suited for constructing large structures at reduced material costs.

The inherent layer-by-layer material addition in metal AM facilitates the fabrication of components that are close to their final shapes. This results in extensive reductions in material wastage, or high material utilisation, compared to subtractive manufacturing. Typically, the buy-to-fly (BTF) ratio, defined by the ratio of the weight of the starting raw material to the weight of the finished product, in subtractive manufacturing of aircraft components ranges from 6–20, while in AW-DED a BTF ratio of 2 or less can be achieved [1–3]. Unlike subtractive manufacturing, which produces mono-material structures, AW-DED methods enable the deposition of structures with spatially varying functional properties. The deposition parameters can be specifically tailored to embed desired microstructural gradients within a component. In addition, the fabrication of multi-material components is feasible by switching to a different wire material or simultaneously feeding multiple wires during the deposition process, thereby creating compositional gradients. In this regard, it is imperative to ensure the employment of chemically compatible materials, or a compositional design approach, to avoid the formation of microstructural constituents that deteriorate the functional performance of a component. Hence, the capability of multi-material deposition or

microstructure control allows for the on-demand generation of material properties during the fabrication sequence of arc-wire AM processes. This feature is unique to metal AM processes and unattainable through traditional subtractive manufacturing methods. Consequently, arc-wire AM methods have seen rapid advancement over the past decade, while attaining significant attention from various industries. However, material-specific challenges can arise because of process-induced effects during AM, thus limiting the application of this technology for successful fabrication of functional components. For instance, consider the response of the single-phase austenitic alloy 36 to AW-DED. This alloy maintains an exceptionally low mean linear coefficient of thermal expansion (CTE) in a temperature range of 25–200 °C, which is driven by temperature dependant magnetovolume effects on the overall thermal expansion of the alloy below its Curie temperature [4]. Due to its low CTE, alloy 36 is widely employed in the aerospace industry as the preferred material for moulding tools. However, as discussed in chapter 2, existing studies on AM of alloy 36 often report the persistence of intergranular cracking in the as-deposited microstructure, thus limiting the application of AM in fabricating the LTE alloy. In addition, the ability of metal AM to achieve tailored functional properties remains largely unexplored in relation to the predominantly binary nature of the LTE alloys. Hence, expanding the application of AM methods in the fabrication of alloy 36 and other LTE alloy components requires further investigation. This allows for a comprehensive understanding of the material response to the prevailing process conditions experienced during AM, thus enabling the exploitation of the unique LTE properties in Fe–Ni alloys via AM.

The objective of this work was to elucidate the microstructural and functional response of alloy 36 to AW-DED, thus expanding the current understanding of the process-property relationships. Extensive experimental efforts have been undertaken to further establish this link. In chapter 4, alloy 36 was deposited at heat inputs ranging from 200–550 J mm^{-1}, with subsequent assessment of the resulting microstructure and functional performance. Unlike the deposition of thin walls without bead overlapping, as reported in existing studies on AW-DED of alloy 36, multi-bead overlapped structures within a wide parameter window were deposited in the present work. The low expansion alloy showed sensitivity to abnormal grain growth as the heat input increased from 200 towards 550 J mm^{-1}. The resistance to grain growth is extremely low in LTE alloys due to their single-phase microstructure. This coupled with the localised thermal energy from the heat source during AW-DED promotes the coarsening of grains that exhibit straight or highly non-tortuous grain boundaries. To put the severity of grain coarsening in perspective, some grain widths were greater than 3–4 mm, when heat inputs of 450 and 550 J mm^{-1} were utilised during the deposition process. In AW-DED, a localised travelling heat source imposes inhomogeneous temperature fields, resulting in non-uniform thermal contraction and expansion of the material. This phenomenon, in conjunction with the temperature-dependent elastic-plastic behaviour of the material, can lead to the introduction of thermo-mechanical stresses and strains within the material. The CTE of the alloy at temperatures well above its Curie temperature is analogous to that of a typical metal, regardless of its invariant thermal expansion in the vicinity of room temperature. This justifies the development of thermal stress or strain in the alloy at temperatures between 0.5–0.8

of its melting temperature, which is the typical temperature range for ductility-dip cracking (DDC) to occur in Ni-base alloys [5, 6]. The coarsened microstructure of alloy 36, characterised by straight grain boundaries, combined with the development of thermo-mechanical forces during AW-DED resulted in a material with increased susceptibility to intergranular cracking. Upon examination of the features of the crack flank, these grain boundary defects were attributed to the phenomenon of DDC. This cracking phenomenon occurs due to a complex interaction between factors that can be classified into two broad categories: metallurgical factors related to the chemical composition of the material, thus determining the thermo-physical properties, and those arising from the process conditions. For an alloy to exhibit DDC, it must meet specific criteria, including being subjected to an elevated temperature cycle and possessing an inherently crack-susceptible microstructure, i.e. single-phase fcc alloys with non-tortuous grain boundaries. The time spent at elevated temperatures leads to grain coarsening in single-phase materials, along with the development of thermo-mechanical tensile stresses/strains. Intergranular DDC occurs when the strength of the grain boundary is exhausted by the stresses or strains localised at these boundaries.

Naturally, the residence time at elevated temperatures can be controlled during AW-DED by selecting an optimised heat input. Reducing the heat input increases the cooling rate, which reduces the residence time of the material at elevated temperatures. This, in turn, reduces the extent of thermally driven abnormal grain growth in alloy 36, thus refining its microstructure. Consequently, DDC was successfully eliminated from the alloy by reducing the heat input from 550 to 200 $J\,mm^{-1}$ during AW-DED, accompanied by a notable reduction in the average grain width, approximately 31% and 72% at different heights along the building direction. The elimination of DDC was evidenced by evaluating the mechanical performance of alloy 36 deposited in the lower and upper extreme conditions of the heat input range, referred to as the low heat input condition (200 $J\,mm^{-1}$) and the high heat input condition (550 $J\,mm^{-1}$). Specifically, the average yield strength, tensile strength, and elongation of the alloy deposited in the low heat input condition were improved by 16%, 23%, and 38%, respectively, compared to that of the alloy deposited in the high heat input condition. The inferior performance in the latter case was due to the presence of internal cracks attributed to DDC. However, the critical thermal expansion behaviour of alloy 36, deposited under low and high heat input conditions, remained identical; in other words, the presence of cracks and differences in grain structure did not affect its thermal dimensional stability. This can be rationalised by the fact that thermal expansion is directionally isotropic in cubic systems [7]. The deterioration of mechanical performance in alloy 36 due to DDC underscores the importance of eliminating this phenomenon in applications where mechanical integrity is critical, such as cryogenic storage, pipeline systems, and space probes. However, in the context of aerospace moulding tools, where thermal dimensional stability is the primary requirement, processing conditions are not strictly restricted to ensure DDC-free microstructures in alloy 36 components produced by AW-DED.

Following the successful defect-free fabrication of alloy 36 in low heat input condition, chapter 5 explores a twin-wire feeding approach to generate multiple

LTE alloy compositions through in situ alloying. Given the poor workability and associated bulk scrap generation during subtractive processing of LTE alloys, the twin-wire feeding method is pivotal in broadening the application of AM-based fabrication routes to these materials. In addition, this approach shows promise for the repair manufacturing of existing composite moulding tools in the aerospace industry, regardless of their chemical composition. Hence, a twin-wire feeding strategy, which involved the simultaneous feeding of alloy 36 wire and high-nickel content wire into a melt pool, was employed during the GTAW-based AW-DED process.

Melt pool observations during twin-wire deposition revealed two distinct metal transfer modes, depending on the wire feeding arrangement. In the continuous metal transfer mode, the deposited beads were characterised by geometrical stability and chemical homogeneity. Conversely, in the intermittent metal transfer mode, beads exhibited spatially varying geometrical characteristics with locally enriched nickel regions. The continuous metal transfer mode involves smooth feeding of liquid metal into the melt pool via a persistent liquid metal bridge, whereas the intermittent mode is characterised by the sporadic entry of individual liquid metal droplets through interrupted bridging or free-flight transfers. The continuous mode was further utilised to successfully deposit multi-bead compositionally graded and mono-material structures. The graded structure featured stable regions of alloys 42, 46, and 52, resulting in a spatial gradient of the Curie temperature—and the resulting thermal expansion behaviour—along the build direction. Meanwhile, the mono-material structure deposited by the twin-wire feeding approach consisted entirely of alloy 46, exhibiting CTE values comparable to those of the commercially available alloy. Hence, on-demand generation of thermal expansion properties was achieved while maintaining stable and defect-free deposition. In addition, the insights gained from the twin-wire feeding approach during GTAW-based AW-DED are transferable to GMAW-based AW-DED, which holds greater relevance for the industrial fabrication of LTE alloys. This is attributed to the increased design freedom combined with the higher deposition rates typically associated with GMAW-based AW-DED relative to GTAW-based AW-DED.

The twin-wire feeding-based deposition of desired LTE alloy compositions primarily stems from the inherent solid solution compatibility between Fe and Ni, despite the highly dynamical non-equilibrium conditions in AW-DED. For instance, Figure 7.1 illustrates the temperature-displacement curves of LTE alloys 40 and 48, fabricated through the twin-wire approach. The curve of alloy 36 which was deposited with the standard single-wire process is included for the reader's convenience. Additionally, alloy 46, which was previously reported in chapter 5, is also presented for the sake of comparison. It is evident from the figure that LTE alloys belonging to the Fe–Ni system offer a range of thermal expansion properties. Alloys with Ni contents ranging from 36 to 42 wt.% are primarily valuable for mould tooling applications, whereas those within the 42 to 52 wt.% range, while still of interest for aerospace applications, are crucial for glass-to-metal sealing purposes [8–10]. The natural compatibility between Fe and Ni, combined with the twin-wire feeding approach during AW-DED, provides a robust foundation for the on-demand generation of LTE properties. Consequently, this exploits the "Invar problem", which is discussed in chapter 2, to efficiently meet the

stringent requirements for thermal dimensional stability in the aerospace industry.

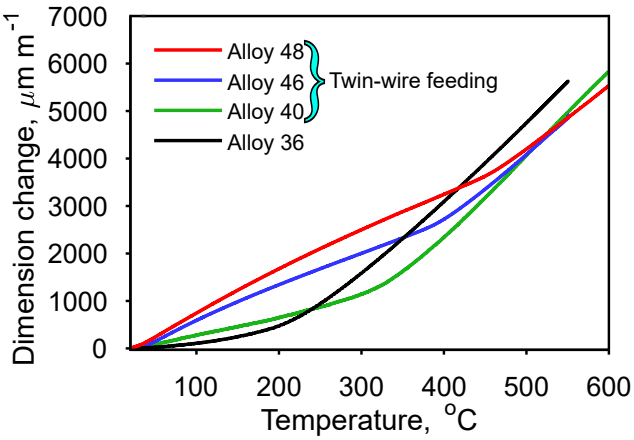

Figure 7.1: Temperature-displacement curves of various LTE alloys showing distinct thermal expansion behaviour depending on the Ni content. Alloys 40, 46, and 48 were deposited with the twin-wire feeding approach, as described earlier in chapter 5, for the generation of desired LTE alloy compositions.

The measured CTE values of alloy 36 and 46 specimens, as reported in chapters 4 and 5, respectively, were observed to share a common trend. In that regard, the CTE of the vertically oriented specimens was consistently lower than that of the horizontally oriented specimens. Such anisotropy in the CTE of LTE alloys fabricated by AW-DED can be explained based on the non-uniform residual stresses developed in a material during the deposition process. These non-uniform stresses can alter the magnetic domain structure in alloy 36 through both reversible mechanisms—such as domain-wall bowing and magnetisation rotation—and irreversible mechanisms, primarily domain-wall movements [11, 12]. Upon stress relaxation, the prior stress-induced alterations in domain configuration may be partially retained due to the irreversible nature of domain-wall movements. This irreversibility arises from stress-induced domain-wall movements between non-magnetic pinning sites, as described by the extended Jiles–Atherton phenomenological model to account for stress in addressing magnetoelastic hysteresis of ferromagnetic materials [13]. The partial reversion of the domain arrangement to that of a stress-free arrangement upon stress relaxation, which occurs when specimens are extracted from as-deposited blocks, explains the observed minor anisotropy of CTE between vertically and horizontally oriented specimens. The maximum absolute difference in CTE between vertically and horizontally oriented specimens was observed to be approximately 0.21 and 0.52 $\mu m\,m^{-1}\,°C^{-1}$, for alloys 36 and 46, respectively. Recent findings reported by Huang *et al.* also support the view that CTE in additively manufactured alloy 36 is primarily influenced by residual stresses, rather than by preferred grain orientations or variations in grain size (diameter or width) [14].

The reduction in heat input facilitated the DDC-free deposition of alloy 36 and other LTE alloys. Generally, AW-DED is preferred for applications that require high

deposition rates and involve large build volumes, typically in the order of metres. However, the heat input reduction-based route to mitigate DDC in alloy 36 during AW-DED presents a contradiction, as it potentially compromises the high deposition rates that make AW-DED advantageous. Therefore, it is essential to explore alternative strategies that mitigate DDC in alloy 36 during AW-DED without relying on heat input reduction. As concluded in chapter 4, DDC in alloy 36 originated primarily from two factors: grain coarsening due to excessive thermal energy in high heat input condition (550 J mm^{-1}) and a microstructure dominated by straight grain boundaries that exhibited low resistance to grain growth. Taking these factors into account, alloy 36 was deposited in chapter 6 via a combined approach of accelerated cooling and TiC particle addition in the high heat input condition, i.e. 550 J mm^{-1} during AW-DED. This approach successfully transformed the microstructure in alloy 36 from DDC-susceptible to DDC-resistant, without compromising the heat input.

Accelerated cooling via a CO_2 jet was utilised during the deposition of alloy 36, effectively reducing the extent of grain coarsening. The average grain width in the alloy deposited with accelerated cooling was reduced by 41% compared to the reference case (without cooling and TiC), also resulting in a reduced susceptibility to DDC. Furthermore, melt pool observations indicated an approximately 20% reduction in the average melt pool length during the deposition of alloy 36 with accelerated cooling, compared to the reference condition. Hence, the use of accelerated cooling ensured effective dissipation of heat, while simultaneously lowering the extent of grain coarsening and intergranular cracking. However, DDC mitigation was achieved by introducing TiC particles into alloy 36 during AW-DED. These particles were effective in pinning the high-angle grain boundaries, while modifying the boundary morphology from straight to tortuous, and consequently inhibiting grain growth. As reported in Chapter 4, the kernel average misorientation (KAM) maps revealed increased strain localisation in alloy 36 deposited under the high heat input condition, compared to that deposited under the low heat input condition. This increase in strain localisation was attributed to a reduction in the available grain boundary area in the high heat input condition. Localised strain at triple junctions and grain boundaries facilitates void nucleation, assisted by grain boundary sliding, ultimately leading to DDC [15]. Similar to the mechanism responsible for mitigating DDC through heat input reduction, the combined approach of accelerated cooling and TiC addition also promotes strain partitioning in alloy 36 among grain boundaries, thereby reducing strain localisation [16]. With this combined approach, the average grain width was reduced by approximately 70% compared to the reference case, effectively eliminating DDC in alloy 36 deposited at a heat input of 550 J mm^{-1}.

In the present study, TiC particles were manually introduced as an interlayer paste during the deposition process. Although this method successfully incorporated the particles into the melt pool, exploring a more comprehensive method, such as integrating a nozzle with the welding torch for powder feeding, could enhance the distribution and effectiveness of TiC particles. Eliminating DDC resulted in an improved mechanical performance of alloy 36 containing TiC particles compared to that of the alloy deposited in the reference case. Specifically, the average yield strength, tensile strength, and elongation increased by 18%, 24%, and 60%, respectively, due to

the absence of DDC. This improvement is also observed to exceed the enhancement in the mechanical performance of alloy 36 achieved by reducing the heat input, as demonstrated in chapter 4.

Concerning the thermal expansion behaviour of the as-deposited alloy 36 with TiC addition, the measured mean linear CTE across multiple temperature intervals was consistently lower than expected. The most pronounced reduction—approximately 34% relative to to the reference alloy—occurred in the 30–100 °C range, i.e. well below the Curie transition. This suggests that the introduction of TiC particles affected the physical mechanism underlying its invariant thermal expansion. The Fe-Fe magnetic exchange bonds in alloy 36 are known to be antiferromagnetically aligned, since the corresponding exchange parameter for these bonds is reported to be negative [17]. Upon the introduction of TiC in alloy 36, its lattice parameter is measured at 3.596(2) Å, compared to 3.592(2) Å, for the reference TiC-free alloy. This increase in the lattice parameter upon TiC addition enhances the ferromagnetic character of alloy 36 as the Fe-Fe magnetic exchange bond in the alloy becomes less antiferromagnetic with an increase in the interatomic distance [18, 19]. Consequently, the Curie temperature of alloy 36 comprising TiC increases, which, in turn, results in a prominent reduction of CTE below the magnetic ordering temperature. It should be noted that this finding of low-temperature CTE reduction in alloy 36 is of particular significance for its application as a mould tooling material in the aerospace industry. Hence, the combined approach of accelerated cooling and particle addition enhanced the cracking resistance of alloy 36 while preserving the high deposition rates inherent to AW-DED and maintaining its characteristic low thermal expansion behaviour.

In summary, this study has explored the complexities associated with AW-DED of alloy 36, highlighting the adaptability and effectiveness of advanced process modifications. The results of the present work underscore the potential of AW-DED to fabricate LTE alloys to meet the rigorous demands of the aerospace industry and other critical applications, setting the stage for future technological innovations.

7.2. CONCLUSIONS

This thesis investigated the processing and performance of LTE Fe–Ni alloys, with a focus on alloy 36 fabricated by AW-DED. The present study addressed key aspects associated with the deposition of LTE alloys, such as grain coarsening, intergranular cracking, process stability, in situ alloying, and functional performance via various processing strategies, including heat input control, twin-wire feeding, accelerated heat dissipation, and alloying modifications. Based on the findings of the individual chapters, the following general conclusions can be drawn:

1. The susceptibility of alloy 36 to ductility-dip cracking (DDC) during AW-DED is closely related to grain boundary morphology and heat input. A reduction in heat input increases the grain boundary area, thereby allowing more effective distribution of localised strain and mitigating intergranular cracking in single-phase Fe–Ni alloys.

2. The mean linear coefficient of thermal expansion (CTE) of alloy 36 remains

consistent under different processing conditions. Despite variations in microstructure or cracking behaviour, the thermal stability of the alloy is retained due to its cubic crystal symmetry and magnetovolume response.

3. The low thermal expansion alloy domain in the Fe–Ni system can be synthesised through twin-wire feeding during AW-DED with reliable compositional control. Both mono-material and graded configurations were successfully deposited, enabling on-demand thermal expansion performance.

4. The continuous metal transfer mode during twin-wire feeding ensures homogeneous deposition and improved process control. The resulting as-deposited alloys exhibit single-phase austenitic microstructures characterised by a uniform distribution of the added Ni, driven by melt pool flow phenomena and chemical compatibility between Fe and Ni. Consequently, the functional properties of the as-deposited alloys agree with the standard specifications of their conventionally processed counterparts.

5. Mechanical performance in alloy 36 improves significantly when DDC is eliminated. The reduction in heat input refines the grain size and increases the grain boundary area, while the addition of TiC enhances the resistance to cracking by promoting the formation of tortuous high-angle grain boundaries, which impede grain growth. Both approaches reduce local strain accumulation, thereby mitigating DDC and leading to higher yield strength, tensile strength, and elongation in the DDC-free as-deposited alloy.

6. Alloy modification via TiC addition leads to a further reduction in CTE, particularly below the Curie temperature. This effect is attributed to lattice expansion and enhanced ferromagnetic exchange, which shift the low thermal expansion response to higher temperatures.

7.3. OUTLOOK

The results presented in this thesis demonstrate and extend the applicability of arc wire-directed energy deposition (AW-DED) to fabricate low thermal expansion (LTE) alloys belonging to the Fe–Ni system. Efforts to promote defect-free deposition through composition and parameter optimisation during AW-DED were undertaken, while also expanding the process to generate on-demand LTE alloy compositions. Moreover, the knowledge obtained from studying the response of LTE Fe–Ni alloys to AW-DED, in principle, can be extended to other chemically compatible binary alloy systems, thus advancing the adoption of AW-DED. The following recommendations are formulated based on the results obtained in the present study:

The reduction in heat input during AW-DED facilitated the crack-free deposition of alloy 36. This occurs at the expense of the deposition rates, although the rates achieved with low heat input settings exceed those obtained through powder-based additive manufacturing (AM) processes. However, when AW-DED is the preferred AM method for fabricating alloy 36 components, the selected consumable must incorporate elements that form precipitates during solidification, particularly at grain

boundaries. This will allow for an experimental effort that explores the limits in process parameter and printing strategies. In this context, AW-DED based on gas metal arc welding (GMAW) is particularly relevant due to the inherent design and process flexibilities.

A preliminary assessment of the effect of intergranular cracking on the thermal expansion of alloy 36 indicated that the thermal expansion remains unaffected by the presence of cracks. However, this topic merits further investigation to establish a definitive relationship between thermal expansion and cracking, or other microstructural defects typically associated with AW-DED. Should future studies confirm a dependency of thermal expansion on internal defects, it could become possible to manipulate process parameters intentionally to tailor thermal expansion characteristics by inducing preferential defects. Conversely, if thermal expansion is proven to be truly independent of defects, this would allow for a broader parametric window during AW-DED of alloy 36 for aerospace moulding tools, without compromising its distinctive low thermal expansion properties.

In the microstructural scales observed during AW-DED of LTE Fe–Ni alloys, the thermal expansion conforms to the symmetry of the crystal, exhibiting isotropic behaviour with respect to the crystallographic directions in fcc systems. However, residual stress development during AW-DED can affect the low-temperature invariant thermal expansion behaviour of alloy 36. Future studies focused on developing constitutive thermo-mechanical models could provide deeper insights into the generation and control of residual stress development during AW-DED. Consequently, this could open up opportunities to tailor the thermal expansion properties of LTE Fe–Ni alloys.

A notable advancement in the cost-effective and efficient processing of LTE alloys can be achieved by adopting a twin-wire approach in AW-DED. This method affords the freedom to harness a range of LTE alloy compositions with desired thermal expansion properties. Rapid advancements in AW-DED have led to the development of twin-wire feeding welding torches suitable for GMAW. In this process, the traditional single-wire welding torch is modified to enable the simultaneous feeding of two wires. Hence, the synergy between the twin-wire feeding approach and GMAW-based AW-DED can be exploited to harness design freedom and incorporate novel functionalities in compositionally graded aerospace moulding tools.

Another metal AM technique that has garnered significant attention along with AW-DED is laser wire-directed energy deposition (LW-DED). Typical challenges associated with AW-DED include distortions in the deposited structure and limitations in the scale of feature size, often in the order of millimetres, that can be incorporated into a component. The adoption of LW-DED can significantly reduce these distortions and allow for greater design complexity due to the combination of unmatched energy density and process flexibility offered by the laser wire-based additive manufacturing process. Consequently, both high-precision and mould tooling applications can benefit from systematic studies on LW-DED of LTE alloys.

REFERENCES

[1] J. Allen. *An investigation into the comparative costs of additive manufacture vs. machine from solid for aero engine parts*. STO Meeting Proceedings. 2006, 17:1–17:10. DOI: 10.14339/RTO-MP-AVT-139-17-pdf.

[2] A. Garcia-Colomo, D. Wood, F. Martina, and S. Williams. *A comparison framework to support the selection of the best additive manufacturing process for specific aerospace applications*. International Journal of Rapid Manufacturing 9, 2-3 (2020), pp. 194–211. DOI: 10.1504/IJRAPIDM.2020.10019230.

[3] B. Dutta and F.H. (Sam) Froes. *The additive manufacturing (AM) of titanium alloys*. Metal Powder Report 72, 2 (2017), pp. 96–106. DOI: 10.1016/j.mprp.2016.12.062.

[4] Carpenter Technology. *Controlled-Expansion Alloys*. CRS Holdings, Inc. Accessed: Mar. 04, 2025. Available: https://www.carpentertechnology.com/hubfs/PDFs/Controlled-ExpansionAlloys.pdf.

[5] A. J. Ramirez, J. W. Sowards, and J. C. Lippold. *Improving the ductility-dip cracking resistance of Ni-base alloys*. Journal of Materials Processing Technology 179, 1–3 (2006), pp. 212–218. DOI: 10.1016/j.jmatprotec.2006.03.095.

[6] D. Qian, J. Xue, A. Zhang, Y. Li, N. Tamura, Z. Song, and K. Chen. *Statistical study of ductility dip cracking induced plastic deformation in polycrystalline laser 3D printed Ni-based superalloy*. Scientific Reports 7, no. 2859 (2017). DOI: 10.1038/s41598-017-03051-x.

[7] H. Saito. *Invar and Invar type alloys*. Physics and Application of Invar Alloys: Honda Memorial Series on Materials Science No. 3. Ed. by H. Saito. Tokyo: Maruzen Company LTD, 1978. Chap. 22, pp. 513–549.

[8] *Standard specification for Iron-Nickel sealing alloys*. ASTM Standard F30-96, 2017. DOI: 10.1520/F0030-96R17.

[9] *Low-expansion alloys*. Metals Handbook Desk Edition. ASM International, 1998, pp. 665–667. DOI: 10.31399/asm.hb.mhde2.a0003159.

[10] R. J. Smith, G. J. Lewis, and D. H. Yates. *Development and application of nickel alloys in aerospace engineering*. Aircraft Engineering and Aerospace Technology 73, 2 (2001), pp. 138–146. DOI: 10.1108/00022660110694995.

[11] C. A. Ives, S. G. H. Staples, C. K. Vo, D. M. J. Cowell, S. Freear, and B. T. H. Varcoe. *Toward using the Villari effect for non-destructive evaluation of steel structures*. Journal of Applied Physics 134, 6, no. 065101 (2023). DOI: 10.1063/5.0147736.

[12] L. Kraus and P. Švec. *Magnetoelastic hysteresis of amorphous ribbons*. Journal of Applied Physics 93, 10 (2003), pp. 7220–7222. DOI: 10.1063/1.1540043.

[13] T. Suzuki and E. Matsumoto. *Comparison of Jiles–Atherton and Preisach models extended to stress dependence in magnetoelastic behaviors of a ferromagnetic material*. Journal of Materials Processing Technology 161, 1-2 (2005), pp. 141–145. DOI: 10.1016/j.jmatprotec.2004.07.016.

[14] G. Huang, G. He, Y. Liu, and K. Huang. *Anisotropy of microstructure, mechanical properties and thermal expansion in Invar 36 alloy fabricated via laser powder bed fusion*. Additive Manufacturing 82, no. 104025 (2024). DOI: 10.1016/j.addma.2024.104025.

[15] A. J. Ramirez and J. C. Lippold. *New insight into the mechanism of ductility-dip cracking in Ni-base weld metals*. Hot Cracking Phenomena in Welds. Ed. by T. Böllinghaus and H. Herold. Berlin: Springer-Verlag, 2005, pp. 19–41. DOI: 10.1007/3-540-27460-X_2.

[16] S. Kihara, J. B. Newkirk, A. Ohtomo, *et al. Morphological changes of carbides during creep and their effects on the creep properties of Inconel 617 at 1000 °C*. Metallurgical Transactions A 11 (1980), pp. 1019–1031. DOI: 10.1007/BF02654716.

[17] K. Lagarec, D. G. Rancourt, S. K. Bose, B. Sanyal, and R. A. Dunlap. *Observation of a composition-controlled high-moment/low-moment transition in the face centered cubic Fe–Ni system: Invar effect is an expansion, not a contraction*. Journal of Magnetism and Magnetic Materials 236, 1-2 (2001), pp. 107–130. DOI: 10.1016/S0304-8853(01)00082-5.

[18] D. G. Rancourt and M.-Z. Dang. *Relation between anomalous magnetovolume behavior and magnetic frustration in Invar alloys*. Physical Review B 54, 17 (1996), pp. 12225–12231. DOI: 10.1103/PhysRevB.54.12225.

[19] P. Gorria *et al. Stress-induced large Curie temperature enhancement in $Fe_{64}Ni_{36}$ Invar alloy*. Physical Review B 80, no. 064421 (2009). DOI: 10.1103/PhysRevB.80.064421.

ACKNOWLEDGEMENTS

Although this thesis presents as the culmination of my PhD journey, with just my name on the cover, multiple names remain to be addressed that made this journey worthwhile, both technically and personally. A big thanks and much gratitude are owed to my supervisory team, Dr Marcel Hermans, Dr Vera Popovich and Dr Constantinos Goulas, for their continued support throughout my PhD journey and for providing an environment conducive to fostering an independent and critical outlook. A sense of critical thinking started to instil in me after my update meeting with Marcel when I was doing my master's thesis under his supervision. His doors have always remained open, be it for technical discussions or brief chats where I pretended to be proficient in Dutch. Thanks for giving me the space to develop as a person and as a researcher, and for your help in translating the summary into Dutch. In times when I was in need of new contacts or equipment to conduct research work, Vera, you constantly guided me to appropriate sources as soon as I had finished mentioning my needs. Your timely responses and deep insights during my PhD have been greatly appreciated and enriching. Finally, Constantinos, you created a friendly yet challenging environment that I enjoyed. Your perspectives on the content I would present in my update meetings and our general discussions outside, like the time we sat at a café in San Diego after my first international conference, have left a mark on me. I believe that anyone in their PhD journey would be lucky to have a supervisory member like yourself. Sincere thanks are also due to the Grade2XL members, especially Marko Bosman, whose enthusiasm and support were much appreciated.

Prior to my PhD journey, I was lucky to have an experienced mentor during my master's thesis at Delft, Dr Gautam Agarwal, who also introduced me to this PhD topic. Early on, I admired your motivation and proactiveness when it came to scientific work, and I am glad that you were there to guide me at the beginning of my research journey, thank you. I also offer my sincere thanks to Dr Martin Luckabauer for his help with the dilatometry experiments; I have truly enjoyed our interactions.

It has also been a pleasure to work with experienced people in the Materials Department. I thank Kees Kwakernaak for the training sessions and for sharing the tricks up his sleeve for successful electron microscopy. Our discussions near the coffee machines at random times were enjoyable. I thank Richard Huizenga for the detailed discussions on X-ray diffraction and our attempts at finding ordered structures. I also enjoyed our discussions on improving sleep quality by limiting caffeine, something I have yet to practise. I am grateful to Ruud Hendrikx for performing X-ray fluorescence at short notice, and to Nico Geerlofs for his active help with dilatometry. I also thank the mechanical group, Elise Reinton and Ton Riemslag, for familiarising me with mechanical testing and showing me the best way to give cold showers to Charpy specimens with liquid nitrogen. I am thankful to Hans Brouwer for turning soft metallic wires into dust and for his help with calorific measurements, and to Remko Seijffers for his active involvement and helpful tips

in performing welding experiments. I also appreciated his regular check-ins when I was trying to deposit 3D-printed walls. Several of the experimental days, since my master's thesis, were spent in the good company of Jurriaan van Slingerland. Thanks to him, many experiments could be performed without delays. I have fond memories of our discussions on culture and about 'zwaar' things, something that will stay with me for a long time.

Sharing a workspace with José, Aravind, Amin, Emiliano and Can over the past years kept a light atmosphere around, even when there were unexpected turns. Aravind and Amin, I appreciated your insights on different topics. Can, you have always been welcoming and that I deeply appreciate. The recent additions, Chrysa and Ashwin, made the last phase of my PhD easier with their presence, and I wish them both success in their future. José, I remember that at the beginning of the project you reached out to me to go for lunch. We sat outside the Aula, enjoyed our sandwiches and talked about our plans. I am glad it worked out well for both of us. I have looked forward to your generous offerings of Glorias from time to time and our everyday conversations. I wish you and Lotte the best for the busy but exciting days ahead. I also had the pleasure of meeting some wonderful colleagues, including Vitória, Philipp, Virginia, Jia Ning, Xiaohui, Zhaorui, Eszter, Gaojieli, Jaji, Joep, Jithin, Mohammed, Gautham and Daniel, in the Materials Department. Special thanks go to the friends from my master's who also continued their journeys in Delft, Devi, Sagar, Tim and Luis, as having you all around meant that candid conversations were always possible. I thank Devi, Sagar, Sid, Vishrut, Arsel, Shivam, Rupak and Vishant for their pleasant and comforting company over the past years in the Netherlands. During that time, I was also lucky to have met Nimmi, Ahmed, Irene and Shubi, whose company made for some of the nicest evenings. Meeting Arthur at X was another highlight; our regular conversations during the little breaks between sets were always enjoyable.

Around the beginning of my PhD, I moved into shared housing in Delft. Fairly soon, it was clear to me that my daily existence away from home would be anything but boring. I can always speak my mind here, and that is something I value. Esh and Luc, our conversations at 'Kailash' were relaxing. Sanya, you were always kind to offer me some freshly baked cakes. Katie, the little incident at Delftse Hout is unforgettable. Prateek, you orchestrated some of the amazing biryani nights. Farouk, one day we will complete the six-month challenge. Jaja, thanks for covering the floor in my room 'Jesus'. Joanna, you are a natural when it comes to mimicking accents. Alexis, thanks for the effort you put in during the search for a lost person. Eleni, thank you for sharing your knowledge of the Greek origins of English words. Leti, the weight of your shoes and the daily drops will always remain a mystery to me. Fer, the 'personal touch' you add to the meals you cook is truly unique.

I also thank my friends from my bachelor's, Nipun, Prithvi, Sahil, Inder, Himanshu, and Mayank, for making sure to call me from time to time and for being immensely understanding. The GAP group from my childhood, Gursimran and Prabhjeet, and Vishvapreet, there is much to catch up on, but I know that when we meet again it will be like the times spent on the basketball courts of YPS.

My mother, father and brother have given me their utmost support, care, encouragement and, above all, a constant affirmation that whatever it is, they are there for me to rely on. They have gone above and beyond for me in ways that I could not possibly go, and for that I am eternally grateful. My brother, Raghav, you will always be the reason

I could explore a different path without a second thought. Thank you for your kindness towards me. Also, to my dear tail-wagging friend back home, Noddy, I will make sure to feed you only your favourites on my next visit.

In the fullness of time, 2014 was a fortunate year, for it was when I met you, Sharon. Since then, you have been my constant, and had it not been for you, there is a good chance that none of this would have happened, if you remember the eventful evening near the Veridian elevator. You lifted me then, and now, from time to time. You saw my struggles and made them ours, all with a smile and without an ask, a rare, humbling grace. For adding meaning and making the fleeting moments of time that we call the past, present and future special, I thank you from my heart.

Arjun Sood
Delft, 2025.

Curriculum Vitæ

Arjun SOOD

Born on 2 January 1994 in Hoshiarpur, India

Education

09. 2020–06. 2025	PhD in Materials Science and Engineering Delft University of Technology, Delft, the Netherlands
09. 2017–06. 2020	Master of Science in Materials Science and Engineering Delft University of Technology, Delft, the Netherlands
06. 2012–06. 2016	Bachelor of Technology in Industrial and Production Engineering Manipal Institute of Technology, Manipal, India

List of Publications

4. **A. Sood**, M. Bosman, R. Huizenga, C. Goulas, V. Popovich, and M. J. M. Hermans. *Enhanced cracking resistance and deposition of alloy 36 via accelerated cooling and TiC addition during wire arc additive manufacturing*. Virtual and Physical Prototyping 20.1, no. e2469827 (2025). DOI: 10.1080/17452759.2025.2469827

3. **A. Sood**, J. Schimmel, M. Bosman, C. Goulas, V. Popovich, and M. J. M. Hermans. *Fabrication of low thermal expansion Fe–Ni alloys by in-situ alloying using twin-wire arc additive manufacturing*. Materials & Design 240, no. 112837 (2024). DOI: 10.1016/j.matdes.2024.112837

2. A. Ebrahimi, M. Sattari, A. Babu, **A. Sood**, G. W. R. B. E. Römer, and M. J. M. Hermans. *Revealing the effects of laser beam shaping on melt pool behaviour in conduction-mode laser melting*. Journal of Materials Research and Technology 27 (2023), pp. 3955–3967. DOI: 10.1016/j.jmrt.2023.11.046

1. **A. Sood**, J. Schimmel, V. M. Ferreira, M. Bosman, C. Goulas, V. Popovich, and M. J. Hermans. *Directed energy deposition of Invar 36 alloy using cold wire pulsed gas tungsten arc welding: Effect of heat input on the microstructure and functional behaviour*. Journal of Materials Research and Technology 25 (2023), pp. 6183–6197. DOI: doi.org/10.1016/j.jmrt.2023.06.280